Title

Evidence for molecular activated recombination of He single ions from particle balance measurements in helium and hydrogen mixture plasmas in PISCES A

Permalink

Author

Cai, Laizhong

Publication Date

2008

Peer reviewed|Thesis/dissertation

UNIVERSITY OF CALIFORNIA, SAN DIEGO

Evidence for Molecular Activated Recombination of He single ions from Particle Balance Measurements in Helium and Hydrogen Mixture Plasmas in PISCES A

A dissertation submitted in partial satisfaction of the
requirements for the degree Doctor of Philosophy
in
Engineering Science (Applied Mechanics)

by

Laizhong Cai

Committee in charge:

Professor George Tynan, Chair
Professor Steve Buckley
Professor Robert Cattolica
Professor Asoka Mendis
Professor Kevin Quest

2008

The dissertation of Laizhong Cai is approved, and it is acceptable in quality and form for publication on microfilm and electronically:

Chair

University of California, San Diego

2008

Epigraph :

Everywhere the human soul stands
between a hemisphere of light
and another of darkness;
on the confines of the two everlasting
hostile empires —Necessity and Free Will.

—- Thomas Carlyle (1795-1881)

TABLE OF CONTENTS

LIST OF TABLES

LIST OF FIGURES

ACKNOWLEDGEMENTS

–Laizhong Cai

First of all, I am greatly indebted to my advisor, Prof. George Tynan, for his guidance and encouragement during my research and study at UCSD. His enthusiasm and insights in plasma physics have been of great value for me. Without his support, it is impossible to finish my Ph.D. work. Especially, he helped me to get over the hard time three years ago. I would like to express my deep and sincere gratitude to him again.

I am also delighted to interact with Dr. Eric Hollmann and Dr. Daisuke Nishijima. They are always accessible and willing to talk with me when I have questions during my research. Their knowledge in plasma physics helps me a lot.

Additionally, I would like to give thanks to all people in the PISCES group, including Karl Umstadter, Russ Doerner, Leo Chousal, Ray Hernandez and Tyler Lynch. My project would not have been finished without the support from my colleagues. I want to give special thanks to Leo Chousal, a nice person who helped me a lot to deal with the PISCES-A facility and offered numerous valuable suggestions about the mechanical design.

I also want to express my gratitude to my Ph.D. committee members, Dr. Robert Cattolica, Dr. Steve Buckley, Dr. Asoka Mendis and Dr. Kevin Quest. Thank them for their valuable comments.

And I would like to give my special thanks to Min Xu and Zheng Yan. We had a lot of fun together. Min also gave me his hand on all of the labor work. Without his hand, my experiment will be an Impossible Mission.

I really want to express my thanks to all those who gave me the possibility to complete this dissertation.

Finally, my deepest gratitude goes to my family for their love and support throughout all these years. This dissertation is simply impossible without them.

Chapter 3, in part, has been submitted for publication of the materials as it may appear in Physics of Plasmas, 2008, Laizhong Cai, George Tynan, Eirc Hollmann. The dissertation author was the primary investigator and author of this paper.

Chapter 4, in part, has been submitted for publication of the materials as it may appear in Physics of Plasmas, 2008, Laizhong Cai, George Tynan, Eirc Hollmann. The dissertation author was the primary investigator and author of this paper.

Chapter 5, in part, has been submitted for publication of the materials as it may appear in Physics of Plasmas, 2008, Laizhong Cai, George Tynan, Eirc Hollmann. The dissertation author was the primary investigator and author of this paper.

Chapter 6, in part, has been submitted for publication of the materials as it may appear in Physics of Plasmas, 2008, Laizhong Cai, George Tynan, Eirc Hollmann. The dissertation author was the primary investigator and author of this paper.

This work is supported by the DoE Grant No. DE-FG02-07ER54912

VITA

1998	B.S., Tsinghua University, Beijing, China
2001	M.S., Tsinghua University, Beijing, China
2001–2008	Graduate Student Researcher, Center of Energy Research, University of California, San Diego, California, USA
2006	Teaching Assistant, Department of Mechanical and Aerospace Engineering, University of California, San Diego, California, USA
2008	Ph.D., University of California, San Diego, California, USA

PUBLICATIONS

Laizhong Cai, Gerorge Tynan, Eric Hollmann, Evidence for molecular-assisted recombination from particle balance measurements in helium-hydrogen mixture plasmas in PISCES-A, Physics of Plasmas, submitted, 2008

Jiachun Wang, Laizhong Cai, NHR Dynamic Analysis of Control Rod and Fuel Assembly of Test Model, Nuclear Power Engineering Vol.22 No.5 P.396-400, 2001

Jiachun Wang, Jiyang Fu, Laizhong Cai, Analyzing and Comparing the Dynamic Response of Test Heater Reactor Main Workshop, Nuclear Power Engineering Vol.22 No.4 P.308-312, 2001

Jiachun Wang, Laizhong Cai, Simulation of Seismic Waves with Wavelets, the 16th SMiRT International Conf., Washington DC, Paper #1202, 2001

Jiachun Wang, Laizhong Cai, Dynamic Analysis of the Control Rod and Fuel Assemblies with Seismic Loads, the 16th SmiRT International Conf., Washington DC, Paper #1855, 2001

Jiachun Wang, Laizhong Cai, The Problems on the Simulation of Seismic Waves, the 11th Structural Mechanics Conference Supplement, 2000

FIELDS OF STUDY

Major Field: Engineering Science (Applied Mechanics)

Studies in Plasma Physics
Professor George Tynan

Studies in Control Engineering
Professor Robert Skelton

Studies in Applied Mathematics
Professor Stefan Llewellyn Smith

ABSTRACT OF THE DISSERTATION

Evidence for Molecular Activated Recombination of He single ions from Particle Balance Measurements in Helium and Hydrogen Mixture Plasmas in PISCES A

by

Laizhong Cai

Doctor of Philosophy in Engineering Science (Applied Mechanics)

University of California, San Diego, 2008

Professor George Tynan, Chair

Detached plasma has been observed on different fusion devices, such as DIII-D, JET. Traditionally, Electron-Ion Recombination (EIR) is considered the dominant volume recombination process to cause detachment in detaching divertors. However, evidence for a new process, Molecular-Activated Recombination (MAR), was found both in PISCES-A and NAGDIS-II, which could be an important path to make a detaching plasma, and was also suggested by theoretical investigation and simulations.

In this dissertation, we describes measurements that quantitatively show the existence and rate of MAR in a low temperature recombining plasma. The experiment is performed on the PISCES-A divertor simulator in University of California, San Diego. In partially detached pure helium plasma, EIR can be demonstrated directly by high excited state emissions. A small amount of H_2 gas is then injected into the target region of this plasma, resulting in the collapse of EIR emission with sufficient H_2 gas density. The plasma is maintained in the partially detached state, therefore indicating that in the presence of H_2 gas another loss process is operative. Since MAR produces H neutrals in a low excited or ground states in contrast to EIR associated with highly excited states, the existence of MAR is also implied by the anomalous large ratio of $\frac{H_\alpha}{H_\gamma}$. Concurrent with this collapse, an increase in the $\frac{H_\alpha}{H_\gamma}$ ratio in the cool ($< 1eV$) outer halo plasma is observed. The results are quite different from the behavior of a standard EIR of H_2 in the cold region, and are consistent with the presence of MAR in the halo region. Using an integral form of the particle conservation equation, we show that this loss process is associated with a volumetric ion loss mechanism associated with the presence of H_2, in other words, it is due to a MAR process. The magnitude of the total volumetric particle MAR sink is derived with the measured parallel flux, ionization source, anomalous radial flux to the wall and EIR sink. The EIR sink rate is obtained in a magnetized He plasma column by absolutely calibrated high n (principle quantum number) He-I line emission associated with EIR. The difference between the total and EIR volumetric sink term is then attributed to the MAR process. The results indicate that the MAR is the dominant recombination mechanism when the H_2 concentration exceeds a few percent. In all cases, radial transport loss is the dominant ion loss term, which is consistent with previous experimental results in pure H_2 plasmas. With the measured radial profiles of MAR, it is seen that the MAR expands from the larger radii toward the center of the plasma column during the detachment. The role and evolution of MAR in detaching plasma reveals how MAR takes over from EIR during detachment in a mixed plasma.

Keywords: Volume recombination, Molecular-Activated Recombination, Electron-

Ion Recombination, Detachment, PISCES-A, Recombining plasma

1

Introduction

1.1 Background

1.1.1 Fusion Energy

Energy is absolutely essential in almost every aspect of our lives. With the development of economy and technology over the whole world, the demand of energy increases rapidly. Currently the main energy resources are fossil fuels, including the coal, oil and natural gas. However, the tremendous consumption of fossil fuels has caused serious issues. Firstly, the so called the greenhouse effect is getting more and more significant; secondly, fossil fuels, as a non-renewable energy, took millions of years to build up and are being depleted. Both the substantial consumption and the lack of the energy made a steep increase of the energy price over the past several years. Therefore, there is an urgent need of finding new energy sources. Although there are a few alternative energys, such as wind energy, biomass energy, geothermal energy, water stored behind dams, solar energy and fission energy, but they do have some disadvantages. For example, the fission energy produces radioactive waste which is a serious safety problem; some others are limited to special territory and natural environments. An attractive potential new energy resource is fusion energy, which has no air pollution and no risk of a nuclear accident. There is an abundant fuel supply for fusion since the material for fusion can readily be extracted from ordinary water which is available to all nations and essentially inexhaustible supply.

Fusion, the process that powers the stars, combines hydrogen atoms into helium, producing energy as a byproduct. The fusion energy is generated when hydrogen is superheated to create a charged gas called plasma and then the particles are fused together. The typical reactions are shown in Equation 1.1, 1.2 and 1.3.

Fusion Energy Reactions:

$$ {}_1^2D + {}_1^2D \rightarrow {}_2^3He(0.82MeV) + {}_0^1n(0.45MeV) \tag{1.1} $$

$$ {}_1^2D + {}_1^2D \rightarrow {}_1^3T(1.01MeV) + {}_1^1p(3.03MeV) \tag{1.2} $$

$$ {}_1^2D + {}_1^3T \rightarrow {}_2^4He(3.52MeV) + {}_0^1n(14.06MeV) \tag{1.3} $$

where D is a Deuterium particle and T is a Tritium particle.

To produce net power, fusion reactions must take place at a high temperature, around 100 million degree Celsius, and be confined for a sufficient time with a sufficient ion density to sustain the reactions. The corresponding condition has to satisfy the Lawson's Criterion [33] given by Equation 1.4 and 1.5, which is used to quantify the performance of a fusion plasma. Although a few various confinement systems have been studied, the most popular confinement scheme for fusion is the tokamak which was invented in the 1950s by Soviet physicists Igor Yevgenyevich Tamm and Andrei Sakharov. The characteristics of a tokamak is its toroidally shaped magnetic field. Consequently, the charged particles at a high temperature are confined by the magnetic field and prevented from striking the vessel walls. The reactor is being constructed to demonstrate fusion energy gain.

Lawson Criterion for Fusion Reactions:

$$n\tau \geq 10^{16} s/cm^3 \qquad for \qquad deuterium-deuterium \qquad fusion \tag{1.4}$$

$$n\tau \geq 10^{14} s/cm^3 \qquad for \qquad deuterium-tritium \qquad fusion \tag{1.5}$$

where n is the plasma density, and τ is the confinement time.

1.1.2 Divertor

A Tokamak type fusion reactor is characterized by very high heat loads to plasma facing surfaces of components surrounding the plasma. Therefore, one of the most important things for a fusion reactor is how to remove the very high heat load from the plasma core without damaging the plasma facing components. It is expected that fusion reactors will use the so-called divertor concept, in which the outer magnetic field lines are diverted far from the plasma by means of specially designed auxiliary magnetic field coils which allow the field lines to then reach the vessel wall where the heat is deposited on specially designed divertor plates. With this configuration, it is possible to produce much purer plasmas, i. e., less contaminated by impurity atoms, and to afford much better energy confinement. In the demo reactor, ITER, a similar divertor design is applied and has a maximum heat load of around $30MW/m^2$ at the divertor target as shown in Fig.1.1. This heat load is so large that it can damage or destroy the target. A potentially attractive solution to this heat exhaust problem is the so-called gas-target divertor, where particles from the edge of the plasma are diverted into a region of high neutral gas pressure 1.2. This innovative way to 'extinguish' Scrape-Off-Layer (SOL) plasma by terminating it in a gas box maintained at high pressure was proposed by Tenney and Lewin [69] in 1974. Certainly, when a neutral gas is pumped into a divertor chamber, the interaction between plasma and gas causes a redistribution of energy and momentum, and can lead to the so-called plasma detachment state. The gas-target divertor has obvious advantages to remove the heat load without damaging plasma facing components. This has been observed in several different devices, such as PISCES-A [4], NAGDIS-II [16], DIII-D [55], JET [42], ASDEX-U [14], Alcator C-Mod [34].

1.1.3 Detachment

The main feature of a detached plasma is a large drop of the electron pressure along the magnetic field line and a loss of both particle flux and plasma heat flux to the divertor target plate. Although the same characteristics are present in every device, there are also some differences in how this process is to occur in different devices. In particular, several different dissipation processes have been invoked to explain detachment, including

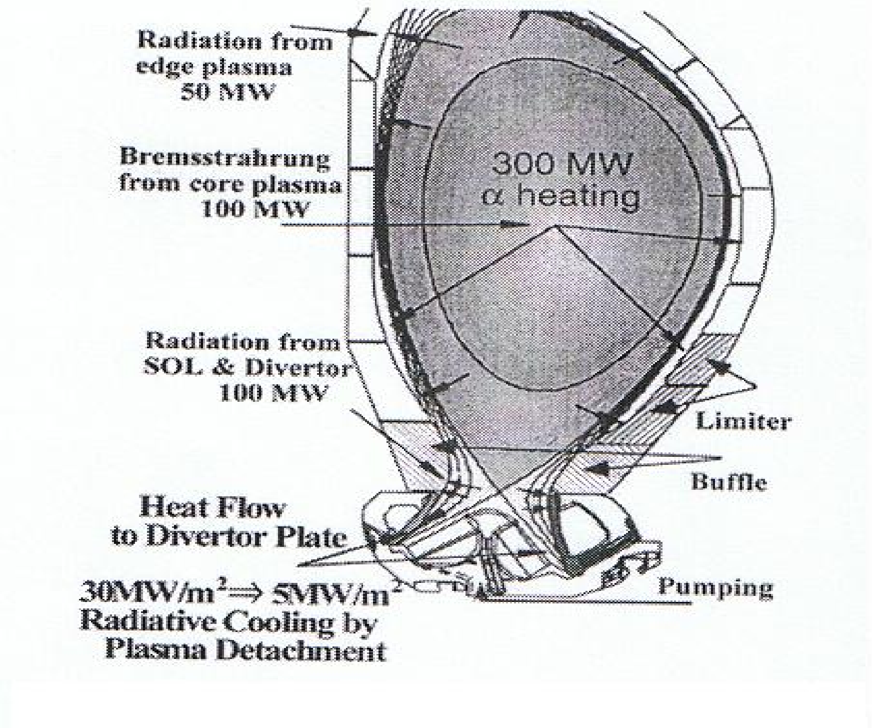

Figure 1.1: The poloidal cross section of tokamak and divertors as well as the power balance in ITER-Final Design Report. (From Ref.[67] by S. Takamura)

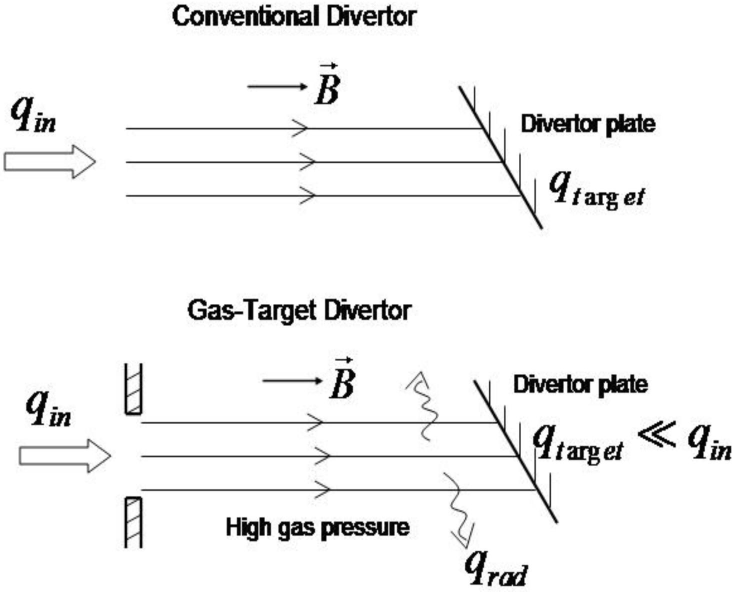

Figure 1.2: A schematic of the gaseous divertor

volume recombination, ion-neutral collisions and non-diffusive cross-field transport. For a specified device, one or more of these processes can occur and lead to detachment.

Generally, the ion-neutral collisions may be important to cool the plasma temperature to $\leq 1eV$ where the volume recombination occurs [53]. The parallel plasma momentum is effectively dissipated by ion-neutral collisions in the presence of a sufficiently high neutral density, and then subsequently dissipated in wall collisions by the neutrals. Since ion-neutral collisions reduce parallel flow speed, volume recombination might then have time to act as a significant sink. It was claimed that a steep plasma pressure drop observed in the detached divertor plasma regime can be attributed to plasma-neutral interactions in the divertor chamber [65]. Although neutral atoms enter plasma at the edge with low energy, they can penetrate deep into the plasma by gaining energy through charge exchange collisions with the much hotter ions. Even small amounts of the resulting fast neutrals in the plasma interior can lead to large non-diffusive energy transport via charge exchange.

It has recently been pointed out that such a mechanism may be ineffective at low plasma densities where the plasma-neutral interaction is weak, and for such a case, an alternative mechanism involving transport of plasma across the magnetic field by turbulent $E \times B$ drifts has been proposed [17]. For instance, non-diffusive cross-field plasma transport, which could be associated with so-called plasma blobs [29, 58], has been observed on PISCES-A [1] and NAGDIS [52], where the total cross-field flux is comparable to the axial flux. In these experiments, the transport to the side wall does not appear to be strongly affected by increasing neutral pressure, suggesting that ion-neutral collisional scattering is not the dominant cause of the radial transport [15, 17]. In the linear divertor experiment device NAGDIS-II, plasma detachment has been observed in hot $(Te \geq 5eV)$, highly ionizing plasmas surrounded by a cold $(Te \sim 0.1eV)$ halo region of recombining plasma. Since the plasma recombination is negligible at $Te \geq 5eV$, these experiments therefore provide indirect evidence that the detachment is primarily caused by cross-field radial transport and by a gradual drop in the ionization source as the temperature of the core region drops below 5eV [16].

As discussed above, volumetric recombination, as distinguished from recombination that occurs on material surfaces, is considered to be an important mechanism leading to divertor plasma detachment in low temperature plasmas [27, 35, 39, 71], and has been reported in almost every experiment focused on studying detachment. Volume recombination of ions into neutrals can occur through radiative recombination and three-body recombination, which are collectively referred to as Electron-Ion Recombination (EIR). For He plasma, the corresponding reactions are shown in Eq.1.6 and 1.7. Two dimensional measurements of divertor plasma density and temperature suggest that the volumetric recombination is effective to reduce the particle flux to the target plates [42].The radiative recombination is usually negligible when the electron temperature is not high $(\leq 5eV)$ [71, 10, 70]. Therefore, in a low temperature plasma, the electron-ion recombination could be the dominant process of volume recombination.

$$He^{+} \quad + e^{-} \rightarrow He + h\nu \qquad\qquad radiative \quad recombination \tag{1.6}$$

$$He^{+} + e^{-} + e^{-} \rightarrow He^{*} + e^{-}; \quad He^{*} \rightarrow He + hv \qquad three - body \quad recombination \tag{1.7}$$

1.1.4 Molecular-Activated Recombination (MAR)

Molecular-Activated Recombination (MAR) is another recombination process that can lead to detachment, and has been reported in PISCES-A, ULS and NAGDIS-II [15, 5, 50]. MAR is associated with vibrationally excited molecules such as $H_2(\nu)$, which mediate the recombination process via the reactions

$$H_2(\nu) + He^+ \rightarrow H + HeH^+ \qquad following\ by \qquad HeH^+ + e \rightarrow H^* + He \tag{1.8}$$

$$and \quad H_2(\nu) + e \rightarrow H + H^- \qquad following\ by \qquad He^+ + H^- \rightarrow H^* + He. \tag{1.9}$$

In order to clearly see the MAR physical process during detachment, hydrogen gas is introduced into helium plasmas during these experiments. The corresponding reactions are described as Eq.1.8 and Eq.1.9. The first is called dissociative recombination; the second is called charge exchange recombination.

According to the previous results from the experiment in NAGDIS-II [50, 51, 7], MAR, associated with vibrationally excited molecules, could strongly affect the divertor detachment process.

1.2 Previous Studies of MAR

Many investigations the molecular-activated recombination have been carried out recently. I summarize some important results based on experiments and simulations.

1.2.1 Previous Experimental Work

Detachment has been observed in several different devices, such as PISCES-A [4], NAGDIS-II [16], DIII-D [55], JET [42], ASDEX-U [14]and Alcator C-Mod [34]. Although the same overall characteristics are present in every device, there are some significant differences between different experiments. The large range in traditional volume recombination levels of detached plasmas relative to the total ion sink $(10-75\%)$ is striking. For example, on JET [41, 42], the volume recombination was found to be an essential and necessary element in divertor detachment. However, the recombination rate was found to be too small to account for the drop in particle sink rate on ASDEX-U [74]. For JT-60U [31] and Alcator C-Mod [36], recombination appeared to play a secondary role in detachment and was evidently not a critical element in the detachment process.

These results suggest that traditional volume recombination is not always the determinant factor for detachment although it appears always to be present. Moreover, the EIR also turns itself off rather quickly when the plasma density drops since three-body recombination is such a strong function of density. Thus once the detachment process begins, this mechanism would then quickly become ineffective.

Motivated in part by these considerations, the effect of MAR in a detached plasma has been researched. The onset of MAR has been observed in the linear device, NAGDIS-II, by injecting small amount of Hydrogen gas into the Helium discharge, and has been reported to be comparable to the EIR rate [50, 51]. Theoretically, the probability of an electron capture in three-body collisions increases rapidly with increasing principal quan-

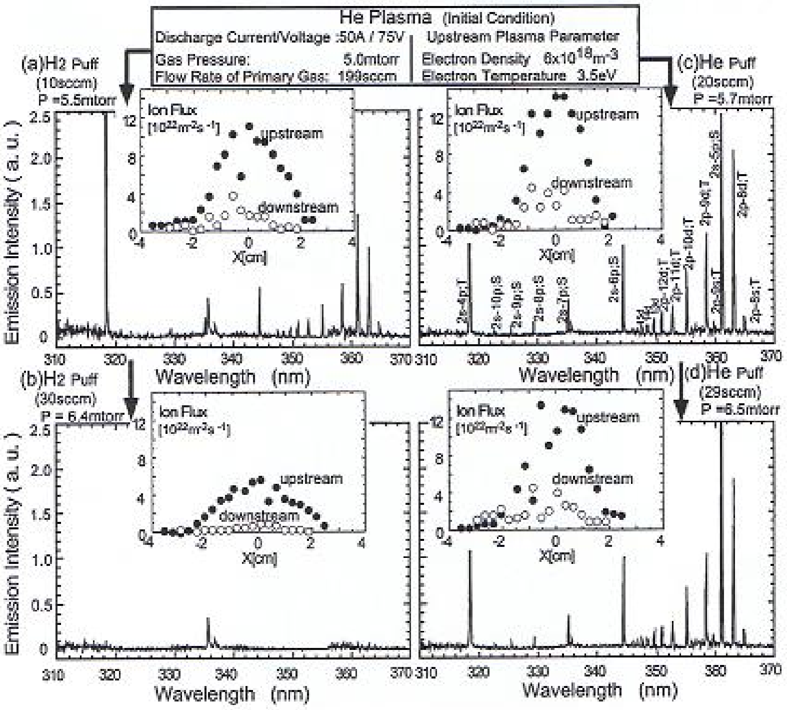

Figure 1.3: Previous experiments on NAGDIS-II: EIR is depressed by injecting H_2 gas, and as a result, MAR is inferred by the reduction of ion flux between the upstream and downstream during the detachment when EIR is quenched. (From Ref.[50])

tum number and decreased binding energy, and so electrons are primarily captured into the upper levels. Therefore, the intensities of high n (principle quantum number) emission lines denote directly the three-body recombination. The continuum comes from the radiative recombination. Fig.1.3 below shows the continuum and line emission spectra, i.e., EIR, from these helium plasma with and without hydrogen injection. The insets present the radial profiles of ion particle flux at upstream and downstream axial locations. Comparing the Fig.1.3(a) and Fig.1.3(c), it is obvious that the three-body recombination and radiative recombination are quenched due to H_2 puffing, since the intensities of the associated emission processes are reduced. Further, according to the Fig.1.3(b), no EIR recombination takes place when the hydrogen density is above a critical value. But the ion flux still has a large drop in the inset of Fig.1.3(b), which means that another physical process occurs to make the ion loss. It is therefore hypothesized that the molecular-activation recombination results in the plasma flux drop, and occurs at a rate comparable to the electron-ion recombination. However, a detailed particle balance was not performed in this experiment and thus no quantitatively statements regarding the MAR role were possible.

MAR has also been observed on Alcator C-Mod tokamak[71]; and was estimated to be 0.7 times of the rate due to the three-body recombination, which was much smaller than the simulation result in Ref.[27, 28, 56]. The measurements were taken at $T_e \sim 1eV$ and $n_e \sim 1.5 \times 10^{21} m^- 3$. No conclusive explanation for the discrepancy was given.

The conditions of MAR or EIR dominant in the plasma were investigated in the ULS divertor simulator by P. K. Browning et al. [5]. It was shown that the MAR dominated in the detached plasma when the plasma density was very low. However, the EIR was dominant in the plasma with higher electron densities and lower electron temperatures.

The different channels of MAR were observed in Ref.[72, 6]. MAR has not been reported in other fusion devices such as the DIII-D tokamak. [22].

1.2.2 Previous Theoretical Work

The effect of plasma temperature on MAR in a detached plasma was investigated by L. Miyamoto[43]. He concluded that the MAR had no significant contribution to the plasma detachment when the electron temperature is in the range of $0.5 \sim 3eV$. The ratio of $\frac{n_{H_2}}{n_e}$ (~ 0.01 in this paper) and re-ionization were considered in the calculated results. The $\frac{n_{H_2}}{n_e}$ ratio was found to be crucial for the contribution of MAR on plasma recombining at $T_e < 1eV$.

The simulation of MAR in a Hydrogen plasma was also carried out [56, 57, 27, 28]. In the collisional-radiative atomic-molecular model, different processes such as dissociation, recombination and ionization, as well the effect of excitation of vibration and electronic states, were taken into account. The calculated MAR rate was much larger than the EIR rate at $T_e < 2eV$. For a plasma of $n_e = 10^{14} cm^{-3}$ and $T_e = 1eV$, the MAR rate could be 50 times larger than the rate of EIR; the ratio of MAR rate to EIR rate also increased when the plasma density decreased. When the ratio of $\frac{n_{H_2}}{n_e} = 0.1$, MAR was calculated to be 30 times larger than EIR at $T_e = 1eV$, $n_e = 10^{15} cm^{-3}$ and dominated the recombining process [27, 28, 56]. It also showed that the density, electron temperature and the $\frac{n_{H_2}}{n_e}$ ratio are important to the MAR rate coefficient.

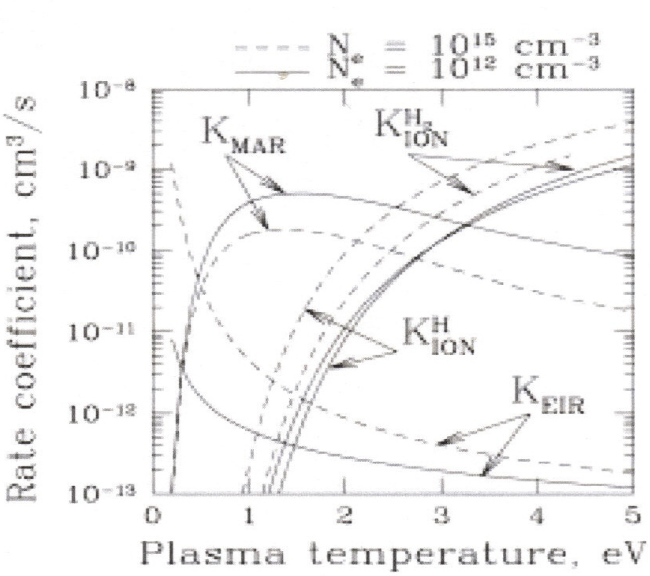

Figure 1.4: Collisional radiative rate coefficients of MAR (K_{MAR}) and EIR (K_{EIR}) as well as the ionization rates of atoms (K^{H}_{ion}) and molecules $(K^{H_2}_{ion})$. The rates are plotted against plasma temperature for two values of electron density: 10^{12} and $10^{15}cm^{-3}$ (From Ref.[57])

Since the conventional volume recombination is ineffective unless the parallel plasma flow is slowed down to allow for sufficient interaction time [64, 73, 40], the effect of plasma flow on MAR was also researched by K. Miyamoto [44]. He concluded that the plasma flow had an effect on the efficiency of the hydrogen molecules available for MAR. He calculated that the flow speed changed the ratio of $\frac{n_{H_2}}{n_e}$ and thus influenced the MAR rate in the plasma flow. It was shown the contributions of volume recombination including the MAR to the ion flux loss was larger when the flow speed was decreased. He also claimed that the MAR rate depended on the H_2 gas temperature. The rate of MAR at

$T_{H_2} = 0.1eV$ was $1.7 \sim 3.8$ times larger than those at $T_{H_2} = 1eV$.

1.2.3 Estimation of EIR and Ionization

In Ref.[9, 12], a collisional-radiative model was developed that included the effects of ionization, excitation, three-body recombination and radiative recombination. Using this model, the populations of different excited states or ground state can be calculated. It was found that the ionization and recombination rates are proportional to the number of photons from the transitions; the ratio of ionization or recombination events per photon, S/XB, was found to be weakly dependent on the electron temperature and electron density, and was unique for each transition. The results of simulation for helium plasma at different electron temperatures and densities are presented in Fig.1.5. Therefore, the emission line intensity is an effective measure to estimate the ionization and recombination rates and is used in this work. The similar measure was used in the experiments in Alcator C-Mod [70, 71].

1.2.4 Previous Experiments on PISCES-A

In PISCES-A, both attachment and detachment of the Ar plasma have been observed [17, 4]. Fig.1.6 shows the attached Ar plasma. By injecting sufficient Ar neutral gas into the target chamber, a cool detached plasma occurs as shown in Fig.1.7. Comparing Fig.1.7 to Fig.1.6, the plasma was obviously detached from the target plate on the right side of Fig.1.7. A noticeable dark zone exists near the target plate on the right side in Fig.1.7. In Helium plasmas, the fully detached plasma state shown in Fig.1.7 can not

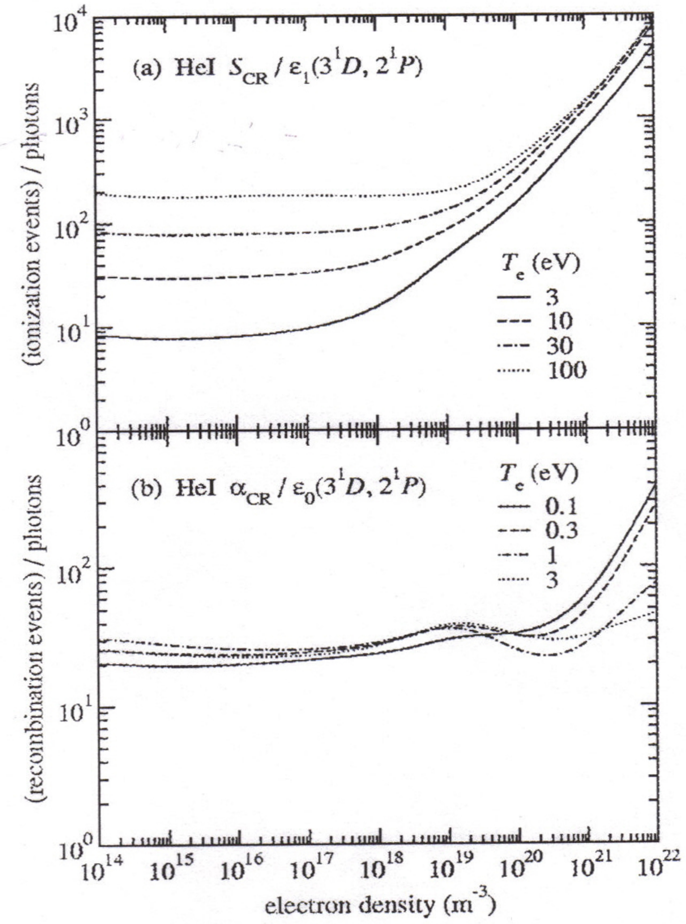

Figure 1.5: The ionizations and recombinations per photon dependent on the electron density and temperature for neutral Helium. (From Ref.[12])

be achieved. When helium neutral gas was injected into the target region, the He plasma was only partially detached, which we define here as a state in which the plasma does not detach from the target plate but there is still a plasma pressure drop along the magnetic field. In both cases, a cold halo region surrounding the hot core region was formed due to the cross-field transport [17].

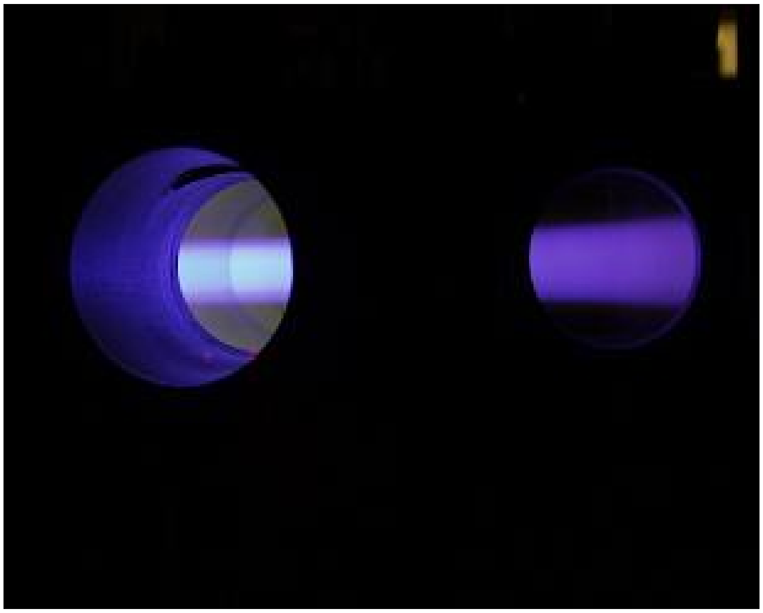

Figure 1.6: Attachment of Argon plasma in PISCES-A

In these He discharges, small amounts of H_2 were then injected; and the ratio of $\frac{H_\alpha}{H_\gamma}$ was measured in PISCES-A [15]. The measured ratio of H_α intensity to the H_γ intensity presented a big jump from $\frac{H_\alpha}{H_\gamma} \approx 15$ to $\frac{H_\alpha}{H_\gamma} \approx 50$ as shown in Fig.1.8. In that earlier work, it was then argued that the $\frac{H_\alpha}{H_\gamma}$ ratio provided a signature of the MAR process. However, no quantitative estimates of the reaction rates of MAR and EIR were made.

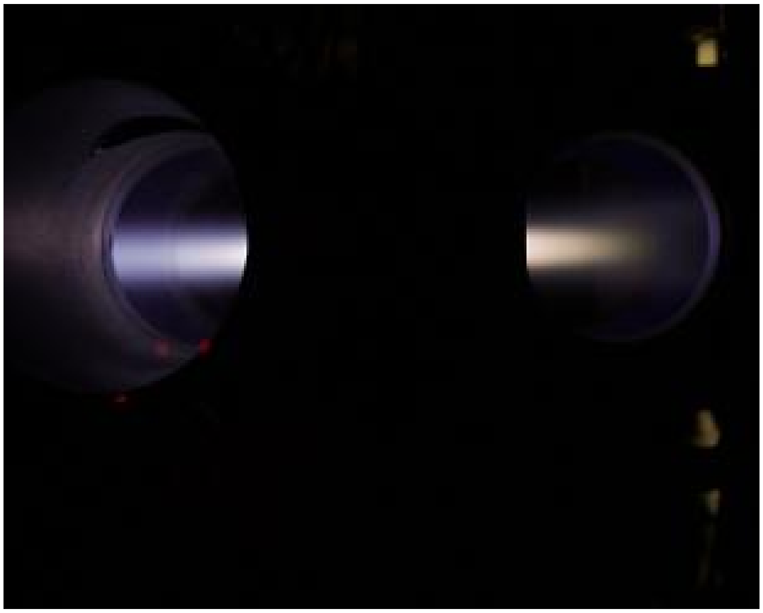

Figure 1.7: Fully detachment of Argon plasma in PISCES-A. The target plate is on the right side of the picture. A clear detachment from the target plate is seen.

1.3 Motivation and Goal

The brief summary above shows that there are a number of questions surrounding the role of MAR during detachment. The clearest open question is: Under what conditions does MAR dominate EIR as the leading volumetric ion term? The goal of this research was to carry out a controlled experiment that would allow a clear answer to this fundamental question. In order to address this question, we performed a set of new experiments to attempt to more conclusively establish the presence of MAR in detaching divertors using the PISCES-A device located at University of California, San Diego. Hydrogen gas is injected into a partially detached helium plasma. Then, by using the particle conservation equation integrated over a special control volume, the MAR and EIR rates

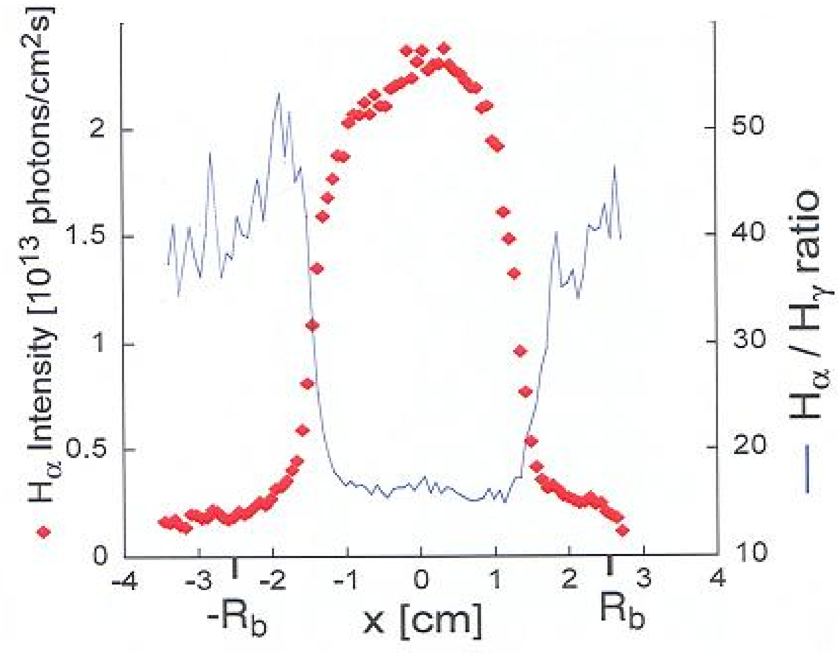

Figure 1.8: The line-integrated Balmer emission and the corresponding $\frac{H_\alpha}{H_\gamma}$ ratio. (From E. Hollmann)

can be estimated quantitatively, and the role of MAR in a low temperature recombining plasma is revealed. In addition, spectroscopy measurements then provide a measurement of photon efficiency from H_2-induced MAR processes, allowing the development of detachment to be followed as the H_2 concentration is increased.

1.4 Organization of the Dissertation

This dissertation is organized as follows. Chapter II will describe the experimental facility, PISCES-A, which is used to implement the research. The operating components and basic diagnostic systems are also displayed. Chapter III simply describes the experimental conditions and operations for the particle balance. The different diagnostics used in this work are presented in chapter IV. The axial flux and radial flux to the chamber wall are measured by Langmuir probes and wall probes, respectively. The EIR is estimated through the intensity of emission from excited Helium neutrals with an absolutely calibrated spectroscopy. In Chapter V, the demonstration and measurements of EIR and MAR, as well as ionization are described. The EIR is estimated quantitatively by Helium neutral emissions, and the MAR is indicated qualitatively with Hydrogen neutral emissions. In Chapter VI, the particle balance analysis is carried out using the measurements of chapters IV and V. The effective MAR rate is derived and a plot of MAR vs. the percentage of H_2 gas in the He-H mixture is given; and the detail of the evolution of MAR is given from profiles of MAR-associated emissions in the recombining region. The final chapter gives conclusions about the experiment and claims that MAR is more efficient than EIR for making detachment.

2

The Experimental Device: PISCES-A

2.1 Overview of PISCES-A

PISCES-A (Plasma-Surface Interaction Experimental Station A) is a linear divertor simulator which can produce a steady state plasma with tokamak edge characteristics. It is mainly applied to investigate the plasma turbulence and atomic processes to test the validity of theory and models for future fusion devices such as ITER. The PISCES-A facility is shown as Fig.2.1 and its typical parameters are listed in Table 2.1.

2.1.1 Vacuum Chamber

The device is 1.5m long along the magnetic field and has a cylindrical vacuum chamber. The stainless steel chamber is divided into two regions by a neck-like flange in a 10cm diameter as shown in Fig.2.2. The region close to the cathode is called source region; the other is the target region which is in a 20cm diameter and 71cm long. The

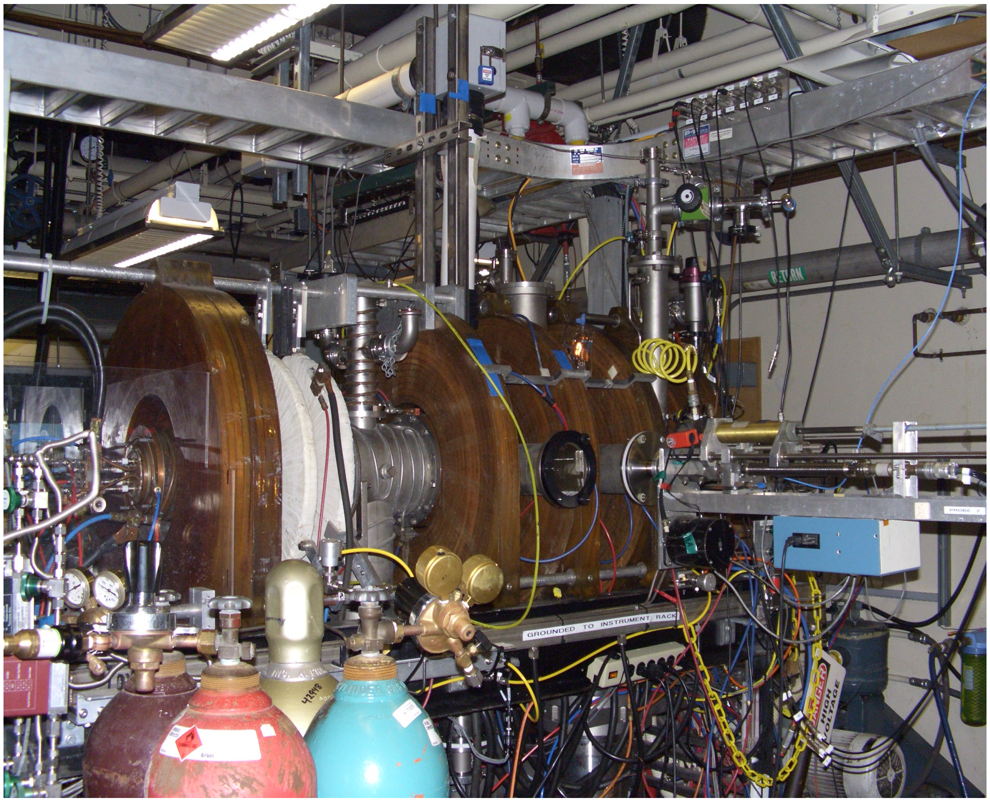

Figure 2.1: The PISCES-A device

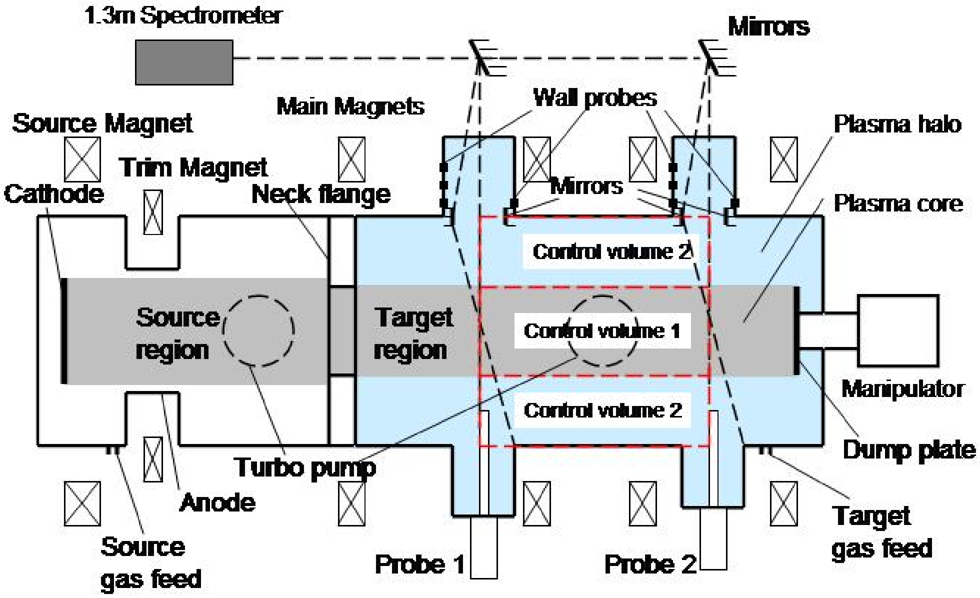

Figure 2.2: The Schematic of PISCES-A. The device is total 1.5m long, and the diameter of the vacuum chamber is 20 cm. The pumping system is not shown for the sake of clarity. However, the upstream volume defined by the cathode and anode, and the downstream volume defined by the region to the right of the anode are independently pumped, allowing independent control of the gas composition and pressure in these two regions.

Table 2.1: Parameters of the PISCES-A device

Parameters	Value
chamber length	$150cm$
chamber radius	$10cm$
plasma radius	$2.5 \sim 3.5cm$
main magnetic field	$0.07 \sim 0.14Tesla$
electron density	$5 \times 10^{10} \sim 10^{13}cm^3$
electron temperature	$\leq 20eV$
discharge voltage	$40 \sim 120V$
discharge current	$20 \sim 60A$

neck-like flange in a 10cm diameter is crucial to isolate the target region from the source region in order to vary the gas pressure independently in these two region. The vacuum chamber is water-cooled by copper tubes soldered to the outside of the walls in order to avoid uncontrolled outgoing of the walls due to heating; and all components are electrically grounded except the floating target plate and the floating baffle tube.

2.1.2 Magnetic Field

The plasma column is confined by the axial magnetic field provided by three independent sets of magnet coils. They are source magnet coils, trim magnet coils and main magnet coils as shown in Fig. 2.2. The magnets outside of the source region, so-called source magnet coils, can vary the magnetic field in a range of $0.03 \sim 0.10 Tesla$, while the magnetic field in the target region can be adjusted from 0.07 to $0.14 Tesla$ by the main magnets. The magnetic field within the target chamber is uniform and is in the axial direction of chamber. The additional trim magnet coils between the source and main magnets are applied to stabilize the plasma discharge to achieve desirable steady state plasma. In this thesis, the experiments are performed at the main magnetic field $B = 0.0936 Tesla (936 Gauss)$.

2.1.3 Cathode and Anode

The plasma is generated by a hot ($\sim 1800^{\circ}C$) Lanthanum-hexaboride (LaB6) disc-shaped cathode. The cathode is 7.6cm in diameter and concentric with a coaxial conducting copper anode, which is 21cm long and 13cm away from the cathode. Primary electrons are produced by the radiantly heated cathode and accelerated by a biased voltage which is applied between the cylindrical anode and the discal cathode. A reflex arc discharge can be created by the primary electrons which ionize the background neutral gas. The plasma transports to the floating target plate along the magnetic field and is sustained in a steady state in PISCES-A, producing conditions similar to those found in the divertor region of tokamak devices.

2.1.4 Pumps and Mass Flow Controllers

There are two turbo-molecular pumps under the chamber, which are operated at a pumping speed of $1500 l/sec$ to achieve a vacuum pressure in the $10^{-7} Torr$ scale. They are used to control the gas pressure in the source region and target region, respectively. These two turbo pumps can be enabled or disabled independently by two gate valves. When the turbo pump under the target region is disabled, it is easy to implement the gas-target divertor operation and achieve a state of partial or complete detachment. Two gas flow controllers are also employed to control the working gas feeding into the two chamber regions. With the combination of turbo pumps and gas flow controllers, the gas pressure in the target region can scan from a few mTorr to 20 mTorr without disturbing the gas pressure in the source region, which is referred to as a gas-target divertor. In addition, the mechanical pump and roots pump keep running during all the experiment operations to remove the bulk gas.

2.2 Diagnostic System

2.2.1 Basic Diagnostics

The PISCES-A is equipped with basic diagnostic systems, including Langmiur probes, discharge voltage and current indicators, pressure gauges such as baratrons, ion gauges. The baratrons are used to monitor the real-time pressures in the source region and the target region. The baratron for the target region is very important since the target gas pressure is a basic parameter to evaluate the gas-target divertor condition. An ion gauge continually monitors the vacuum pressure. Generally, the base vacuum pressure should be in the $10^{-7} Torr$ scale before starting to discharge. However, the ion gauge must be turned off during the experiments due to the fact that the pressure is higher than

1mTorr as well as due to the magnetic field. In addition to these measurements, there is a continuous measurement and display of the real-time discharge voltage and discharge current. A temperature indicator is also on this panel to display the temperature of the target plate which is measured by a thermocouple.

2.2.2 Langmuir Probes

There are two probes to measure the electron density and temperatures. They are pneumatically driven and can scan radially from the edge to the center of of the chamber. The Langmuir probes are located at the two view ports as shown in Fig. 2.2, which are 103cm and 126cm away from the cathode, respectively. The probe tip is in a cylindrical shape with the diameter $d = 1.5mm$ and length $l = 1mm$. The probe close to the source is called the upstream probe, while the other is the downstream probe. Each probe has one probe tip and can scan radially to get the radial profiles of the probe current by applying a biased voltage. According to the measured I-V characteristic curve with a sweeping voltage, the electron density and electron temperature can be estimated easily. The corresponding position of the probe tip during scanning radially is monitored by a positioning sensor.

2.2.3 Wall Probes

A set of wall probes are used to estimate the cross-field transport to the chamber wall. There is one set of wall probes in each side port as shown in Fig.2.2. The wall probe is a $75.3mm^2$ copper plate isolated by a 0.5mm thick Teflon sheet. A set of wall probes

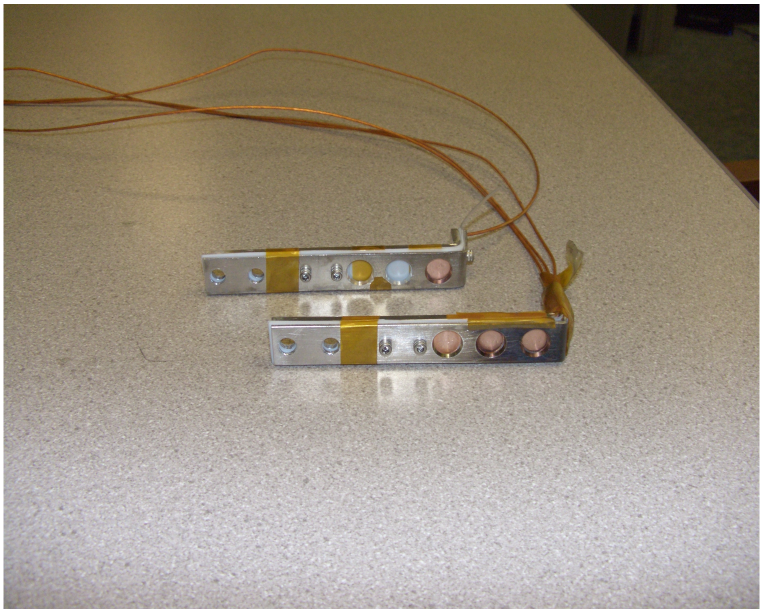

Figure 2.3: A set of wall probes for one side port.

are shown in Fig. 2.3. By applying a sufficient negative voltage to the copper plate, the ions in the side port are collected. Each set of wall probes includes three wall probes on the side port wall and one on the facing wall as shown in Fig.2.4, which are located in the vertical plane of the center of the plasma. Fig. 2.4 show how the wall probes are mounted on the wall of the side port. With the ion saturated currents measured by the wall probes, the ions coming into the side port from the edge region of the chamber can be derived.

2.2.4 Spectroscopy

The spectrometer used in this work is a Czerny-Turner type, McPherson model 209 with a 1.33m focal length. It can be used to measure the emissions of wavelength in the range of 1850 $\sim$ 13000 Å, including visible spectrum. The emission light from the plasma through a view port is focused onto the entrance slit of the spectrometer by a lens

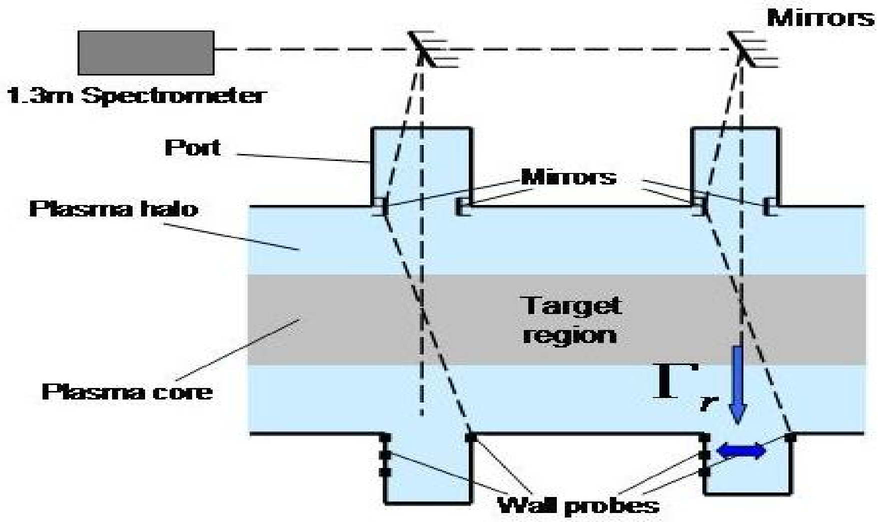

Figure 2.4: The schematic drawing of installation of wall probes and mirrors mounted on the wall of the side port.

and mirror mounted on the optical rail. A CCD camera is connected to the spectrometer to capture 2-D images of the broadband visible spectrum.

A series of emission lines from highly excited Helium neutral transitions are measured to estimate the ionizations and the recombinations. H_α and H_γ are also measured by the spectrometer. These measurements are made by employing a 1200 groove/mm grating, which is manipulated with a stepper motor to select the desired wavelength. The absolute intensity of the emission is obtained by calibration with a Calibration Source Optics Head (model: 456-12-1). The low electron temperature at large radii of the chamber is estimated by the absolute intensities of emissions. The details on how to estimate the ionization and recombination rates and low electron temperature using spectroscopic measurements are presented in Chapter 4 and 5.

Fig. 2.5 shows the photograph of the mirrors. Two mirrors are mounted on each side port to measure the axial flow speed as shown in Fig. 2.4. We can manually turn the mirror on the optical rail to collect the light reflected by the mirrors mounted on the side wall. One view, made orthogonal to the magnetic field, provides an unshifted line emission spectrum. A second view, made at an angle of 20 $\sim$ 30 degree with respect to the magnetic field, is used to measure the Doppler shifted line emission. The axial flow speed is estimated by the Doppler shift. The installation of wall probes and mirrors is presented in Fig. 2.6.

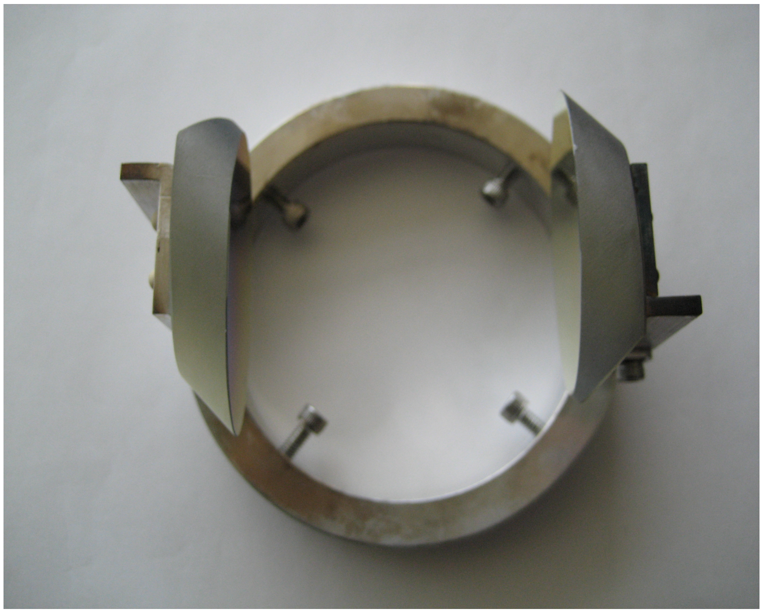

Figure 2.5: Mirrors for the axial flow speed which are mounted on the wall of the side port.

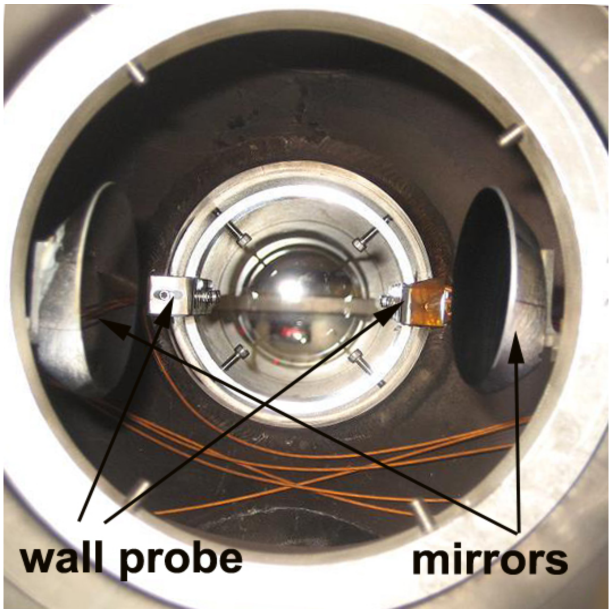

Figure 2.6: The installation of wall probes and mirrors mounted on the wall of the side port.

2.2.5 PISCES-A Operations

As shown in Table 2.1, PISCES-A produces basically an attached plasma and has a great flexibility in operation parameters. Typically, the electron density is in the range of $5 \times 10^{10} \sim 10^{13} cm^3$; and the electron temperature is less than 20eV. For these plasmas, there is a core plasma region in a $5 \sim 7cm$ diameter along the magnetic field, while a cold halo region surrounding the core plasma also exists due to the turbulent cross-field transport of particles and heat.

PISCES-A can be operated with different working gases such as Hydrogen, Helium and Argon. For the Hydrogen and Argon gas, it is easy to get fully detached by separately adjusting the source gas pressure and target gas pressure. The neutral gas pressure in the target region can scan from 1mTorr to 40mTorr with the combination of gate valves and gas feed controllers. However, for Helium gas, the plasma is only partially detached with a discharge voltage of $60 \sim 100V$ and a discharge current of $20 \sim 40A$. Helium is the main working gas in this experiment. A detailed description about the experiments will be presented in Chapter 3.

Overall, PISCES-A provides the opportunity for experimentation in a relatively simply linear magnetic geometry to simulate the plasma behaviors in a toroidal tokamak, and provides an excellent platform to study the role of MAR in causing detachment in divertor plasma conditions.

3

Experimental Operations

3.1 Basic PISCES-A Experiments

The plasma is generated by the biased voltage between a Lanthanum-hexaboride (LaB6) disc-shaped cathode and a concentric copper anode. The primary electrons are accelerated by the cathode-anode discharge voltage and collide with neutral gas, resulting in the creation of a plasma in the device. The resulting steady state plasma can freely move along the magnetic field into the downstream region. There are two molecular turbo pumps to separately control the gas flows to pump from the source region and target region, respectively. With the combination of the two gas feeding controllers and the two turbo pumps, the gas pressures in the source region and the target region can be adjusted independently, which produces conditions similar to those found in the divertor region of tokamak devices. The gas pressure in the target chamber can vary from a few mTorr up to 20 mTorr for Helium plasma in these experiments, while the source gas pressure is held at a fixed pressure.

In order to understand the role of MAR in detaching plasma, a pure helium plasma is created first; then MAR is produced by injecting a small amount of Hydrogen gas into the downstream target chamber. Fig.3.1 shows an attached pure He plasma with target gas pressure at 3mTorr, where an obvious halo region surrounding the core region is seen. Injecting Helium neutral gas into the target region, the partially detached plasma is presented in Fig. 3.2, where the violet halo is produced by the emission ($340 \sim 450nm$) of highly excited He neutral transitions as the EIR "monitor". For this example, the source gas pressure is at $\sim 6mTorr$, while the target gas pressure is at 7.3mTorr. MAR can then be studied by injecting a small amount H_2 gas into the target chamber. Fig.3.3 shows the plasma with the total target gas pressure of 8.0mTorr (7.3 mTorr He and 0.7 mTorr H_2). With a small amount of H_2 gas puffing, the halo emission becomes dominated by longer wavelength ($\sim 650nm$) light associated with MAR. When the H_2 concentration exceeds a critical value ($\sim 12\%$), no EIR appears at all, as described in Chapter 6. By combining these results with a particle balance analysis over a suitable control volume, the role of MAR can be quantitatively demonstrated in experiments.

3.2 Experiment Outline for the Particle Balance

Fig. 3.4 presents the different contributions to the particle balance in the plasma in the target chamber of PISCES-A, where all of the measurements were performed. There is a hot ($\sim 10eV$) core region with a $2.5 \sim 3.5cm$ diameter. This core is surrounded by

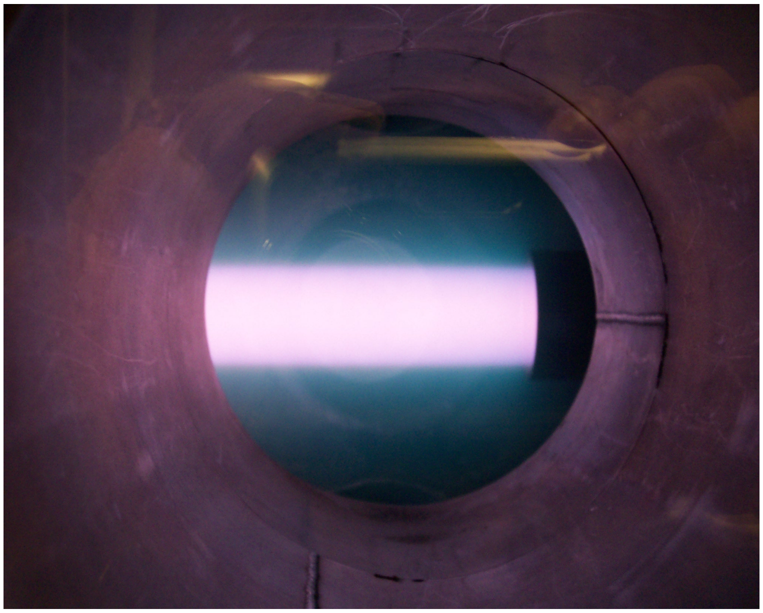

Figure 3.1: A fully attached helium plasma in PISCES-A. The target gas pressure is 3mTorr, and is composed of pure He. The target plate is on the far left side of the photo.

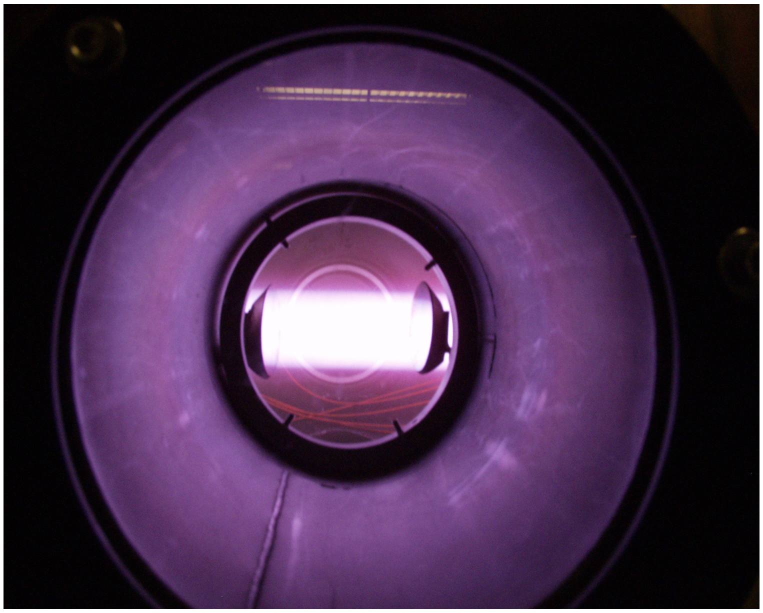

Figure 3.2: The partially detached Helium plasma in PISCES-A. The target gas pressure is 7.3mTorr, composed of pure He.

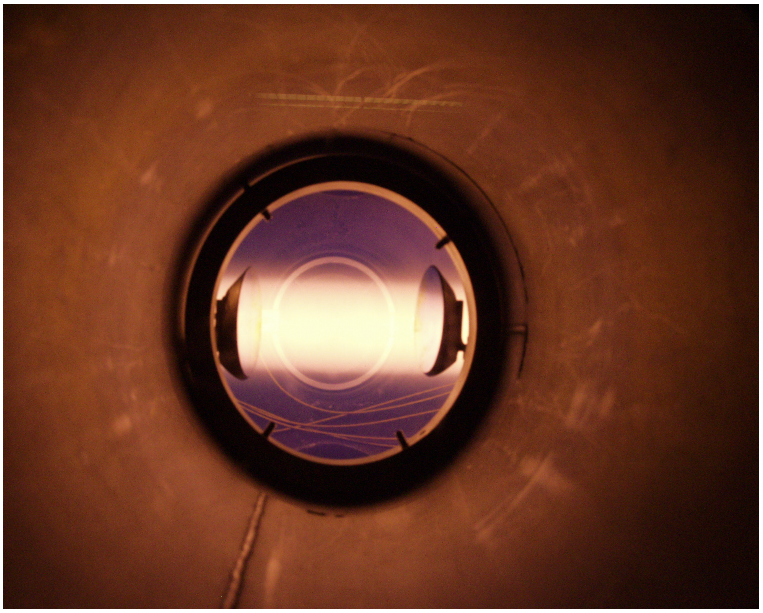

Figure 3.3: The detaching Helium plasma with injecting H_2 gas. The target gas pressure is 8mTorr, consisting of 7.3mTorr He and 0.7mTorr H_2.

a cold ($\leq 1eV$) halo region that is fueled by the cross-field transport of plasma from the core region. Ionization only takes place in the core region since the electron temperature in the halo region is too low to ionize the neutral He atoms. In the halo region, which is at low electron temperature, both EIR and MAR are present. In the core region they are negligible since the temperature is above 5eV. In the absence of H_2 injection, 3-body recombination should be dominant in the cold halo region since the radiative recombination is negligible in the PISCES-A plasma conditions [70, 71, 10]. As argued in a later section, the intensities of high n emission lines of Helium neutrals denote directly the three-body recombination in the cold halo region.

Now consider the two control volumes of the plasma presented in Fig. 3.5. The parallel flux $\Gamma_{\|}$, cross-field flux Γ_r, ionization source S_{ion}, EIR sink S_{EIR} and MAR S_{MAR}

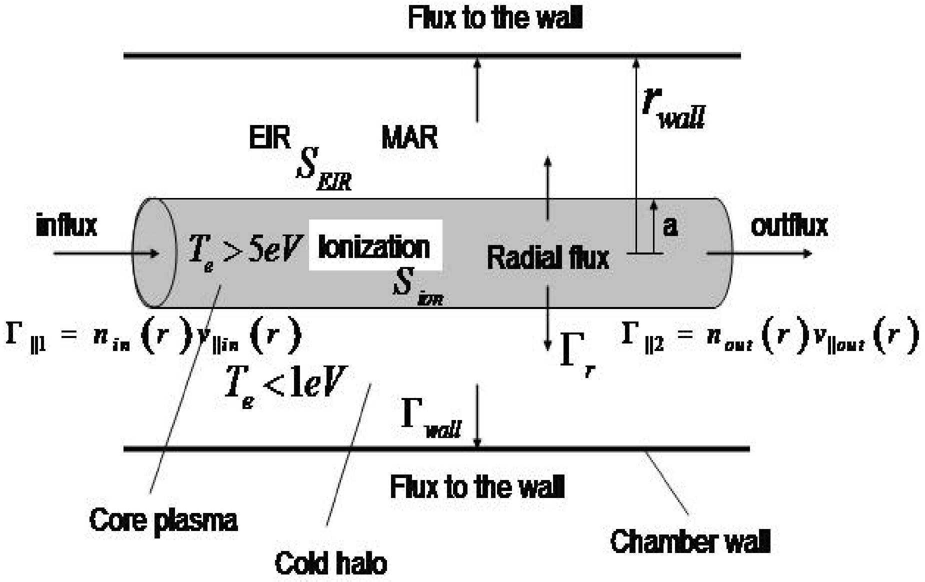

Figure 3.4: Schematic of the particle balance in the PISCES-A plasma column.

sink contribute to the particle balance in the two control volumes. The particle conservation equation shown in Eq. 3.1 can be evaluated for S_{MAR} when $\Gamma_{\|1}$, $\Gamma_{\|2}$, Γ_r, S_{ion} and S_{EIR} are known from measurement.

$$\int(\Gamma_{\|1}-\Gamma_{\|2})dA_z-\int\Gamma_r dA_r+\int(S_{ion}-S_{EIR}-S_{MAR})dV=0 \tag{3.1}$$

where S_{EIR} and S_{MAR} are the EIR and MAR recombination sink, respectively; $\Gamma_{\|1}$ and $\Gamma_{\|2}$ are parallel particle fluxes at axial location 1 (the upstream port) and 2 (the downstream port).

Certainly, no MAR occurs at all for pure Helium plasma, the 0% H_2 case, and then the particle conservation equation is rewritten as Eq. 3.2.

$$\int(\Gamma_{\|1}-\Gamma_{\|2})dA_z-\int\Gamma_r dA_r+\int(S_{ion}-S_{EIR})dV=0 \tag{3.2}$$

The particle balance analysis is more straightforward if we breakup the experimental region into two distinct control volumes as shown in Fig.3.5. In the core region (control volume 1, which is the filled cylinder shown in Fig. 3.5), defined by the region where T_e is large enough ($\geq 3-4eV$) that S_{EIR} and S_{MAR} can be neglected [56, 57], the particle balance for this region is given as

$$\int(\Gamma_{\|1}-\Gamma_{\|2})dA_z+\int S_{ion}dV_1=\int\Gamma_r dA_r \tag{3.3}$$

In the halo region (control volume2, which is the blank ring shown in Fig. 3.5), defined by the region where S_{ion} is small enough to be neglected $(T_e < 1eV)$, we have

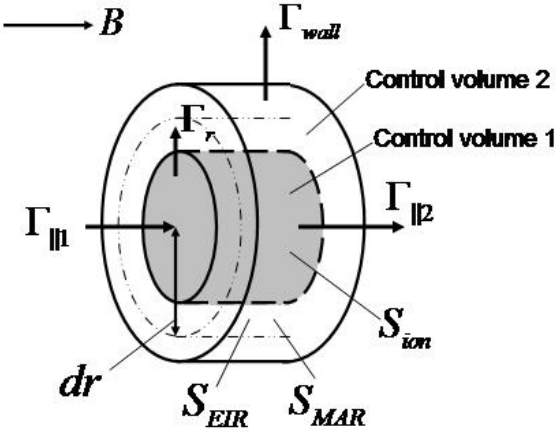

Figure 3.5: The particle balance in a control volume. The filled cylinder, control volume 1, is the region of core plasma; and the outer boundary of the control volume 2 is the chamber wall. The cross section on the left is at the upstream port; the one on the right side is at the downstream port.

$$\int \Gamma_r dA_r = \int \Gamma_{wall} dA_{wall} + \int (S_{EIR} + S_{MAR}) dV_2 \tag{3.4}$$

where Γ_r is the radial flux on the boundary of the control volume 1, and Γ_{wall} is the radial flux to the chamber wall. V_1 and V_2 are the whole volumes of control volume 1 and 2, respectively; A_{wall} is the wall area of the control volume 2, that is, πDl (D is the diameter of the chamber, l is the length of the control volume 2); $dA_z = 2\pi r dr$ ($0 \leq r \leq a$ and a is the radius of the control volume 1); and $A_r = 2\pi al$. These expressions neglect parallel fluxes and ionization in control volume 2. The axial flow speed drops by two orders of magnitude small for $r > 3.5cm$ while the electron density in the halo decreases to $< 10\%$ of the density in the core region as described in chapter 4. As a result, the axial flow in the halo region is three orders of magnitude smaller than that in the core region and can be neglected in the halo region particle balance. Due to the low electron temperature in the halo region, EIR and MAR happen mainly in this region and there is no significant ionization.

The particle balance is performed in two consecutive steps. First, according to the axial fluxes and ionization source in the core region (control volume 1), the number of the particles coming out of the core is calculated by Eq.3.3. After that, the MAR can be derived by Eq.3.4 with knowledge of the cross-field particle flux to the chamber wall and the EIR in the halo region (control volume 2) since the parallel flux into the halo region is negligibly small. By adjusting the percentage of H_2 gas pressure with the gas feeding controllers, the particle balance can be studied across a range of conditions, from the case without MAR to the case of no significant EIR at all, which happens when the precentage of $\frac{P_{H_2}}{P_{total}}$ reaches a critical value, $\sim 12\%$ in this experiment.

Since all the other parameters are well diagnosed, the MAR can be quantitatively estimated by Eq.3.1, 3.2, 3.3 and 3.4 for various concentrations of H_2. Clearly, the relative errors must be carefully treated in order to successfully determine the rate of MAR. We can also use the hydrogen neutral emission line ratio $\frac{H_\alpha}{H_\gamma}$ to qualitatively demonstrate the presence of MAR. The spectral emission profiles of this ratio are Abel inverted to obtain the radial profiles of MAR for various H_2 concentrations. The results show the development and evolution of MAR during detachment, and demonstrate that it becomes the most important volumetric He^+ loss mechanism once the H_2 partial pressure exceeds a few percent.

3.3 Plasma Conditions for Measurements

During the experiment, the Helium gas pressure in the source region was held constant at a value of 6.3mTorr, while the target gas pressure changes from 7.3mTorr for the pure helium case to a maximum total pressure of 8.3mTorr for a mixture of 88% He and 12% H_2 gas when 20.4sccm of H_2 gas is injected into the downstream chamber. In this way, the percentage of H_2 gas in the mixture can be varied from $0 \sim 12\%$ while maintaining nearly constant source conditions. Measurements are taken at the percentage 0%, 1.2%, 2.9%, 5.9%, 8.8% and 12% H_2 gas partial pressure. The magnetic field is kept constant at 936 Gauss. The parameters of the experiments are listed in the table 3.1 below.

The discharge voltage and current have changed slightly after flowing H_2 gas. The case 1 is pure Helium plasma without MAR. Results show that after flowing H_2 gas, the EIR is depressed and evidence for MAR is observed. In case 6, which has 12% H_2 gas, the EIR is quenched according to the emissions from highly excited Heliume neutral transitions.

Table 3.1: Parameters of Different Experimental Cases

Case Number	Source Gas Pressure (mTorr)	Target Gas Pressure (mTorr)	Main Magnetic Field (Gauss)	MFC for He gas (sccm)	MFC for H_2 gas (sccm)	Discharge Voltage (V)	Discharge Current (A)	H_2 in Total Pressure
1	6.3	7.3	936	65.2	0	78	34	0%
2	6.3	7.4	936	65.2	2	83	31	1.2%
3	6.3	7.5	936	65.2	5	85	30	2.9%
4	6.2	7.8	936	65.2	10	85	29	5.9%
5	6.3	8.0	936	65.2	15	90	27	8.8%
6	6.3	8.3	936	65.2	20.4	95	26	12%

3.4 Required Measurements

In order to perform the particle balance with the particle conservation equations (Eq.3.1, 3.2, 3.3 and 3.4), the electron temperature, electron density, axial flow speed, cross-field flux to the chamber wall, emissions from highly excited Helium neutrals and Hydrogen neutral emissions must be made. Two Langmuir probes, which can scan radially at two axial positions, are used to measure the radial electron density and temperature profiles. Helium ion emission Doppler shifts are used to measure the axial ion flow speed, which is combined with density measurements to estimate the axial particle flux. A set of wall probes are mounted on the wall of each side port to obtain the radial flux to the wall as shown in Fig. 2.2. The ionization source and EIR sink are measured by an absolutely calibrated 1.3m Czerny-Turner spectrometer measuring He line emissions at 667.8nm and 353.1nm. The low electron temperature at large radii of the vacuum chamber is also estimated by the Helium neutral emission, which is important to calculate the EIR in this region.

According to particle conservation equations above, the MAR is then calculated. The details of the measurements will be presented in Chapter 4 and 5.

ACKNOWLEDGEMENT

Chapter 3, in part, has been submitted for publication of the materials as it may appear in Physics of Plasmas, 2008, Laizhong Cai, George Tynan, Eirc Hollmann. The dissertation author was the primary investigator and author of this paper.

4

Measurements

After the Helium discharge is created, a controlled amount of Hydrogen gas is introduced to the target chamber while the source Helium gas pressure is maintained at 6.3mTorr. With the combination of two gas flow controllers and independent gate valves connected to two turbo pumps, the target gas pressure changes from 7.3mTorr of pure Helium to 8.3mTorr of the mixture of He and H_2 gas when injecting H_2 gas into the chamber. Therefore, the percentage of H_2 gas in the neutral gas mixture varies from 0% to 12%. As a result, the measurements are taken at the percentage of 0%, 1.2%, 2.9%, 5.9%, 8.8% and 12% H_2 gas, which are called Case $1 \sim 6$, respectively. The constant main magnetic field is 936 Gauss.

4.1 Langmuir Probe Measurements of Plasma Temperature and Density

4.1.1 Diagnostics

Two horizontal probes are located at 103cm and 126cm away from the cathode, respectively, as shown in Fig.2.2. The probe close to the source is called the upstream probe, while the other is the downstream probe. These two horizontal Langmuir probes, which are pneumatically driven, are used to measure the electron density and electron temperature of the plasma to estimate the axial particle flux. Each probe has one tungsten probe tip with a 1.5mm diameter and a length of 1mm and can scan radially to obtain the radial profiles of electron density and temperature by applying a sweeping voltage ($-150 \sim\ 0V$). The probe current through a 100 Ω shunt resistor is collected to obtain the I-V characteristics by which the plasma parameters can be derived. The corresponding position of the probe in the chamber is monitored by a sensor, so the electron temperature and density at a specific position are obtained. The frequency of the sweeping voltage biased on the probe tip is 50Hz. As a result, the spatial resolution of the electron density and temperature is $1 \sim 2mm$. The measurements are collected by a 8-channel data acquisition system. For each channel, the sampling frequency is set at 50kHz.

4.1.2 Basic Probe Theory

Many investigations on a Langmuir probe, the most popular plasma diagnostics, have been carried out since the dawn of plasma physics research. The basic characteristic is revealed by the I-V curve of a Langmuir probe as Fig. 4.1.

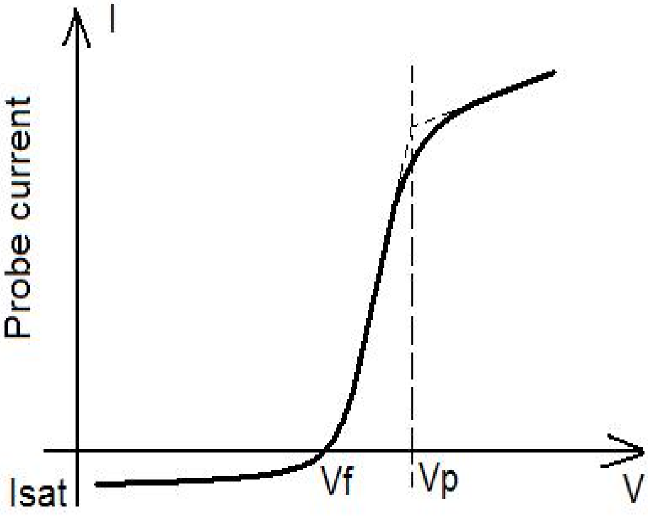

Figure 4.1: The typical I-V characteristic of Langmuir probe data.

For a thermal plasma of comparable electron and ion temperatures, the mean electron speed is much larger than the mean ion speed. Therefore, when the probe tip is inserted into the plasma, the total probe current is dominated by the electron flux to the probe tip. If the probe is a floating probe, that is, electrically insulated from other parts of the plasma device, then it would charge up rapidly until the electrons are repelled and consequently the net electrical current reaches zero. At this time, the potential of the probe is the floating potential V_f, which is below the plasma potential, V_p. The floating potential and plasma potential are shown in Fig. 4.1. Applying a sufficiently negative biased voltage to the probe, all electrons are repelled from the probe and only ion saturation current I_{sat} is drawn. If the biased voltage is positive, the ion current is decreased due the repulsion of the ions and the electron current is drawn to achieve the electron-saturation current, which is much larger than I_{sat}.

For the experiments, the ion gyroradius is about $3 \sim 6mm$ with main magnetic field $B = 936Gauss$, while the diameter of the probe is 1.5mm. Therefore, the probe is considered a "unmagnetized" probe. The corresponding I-V characteristic is derived by I.H. Hutchinson as Eq. (4.1) [20].

$$I = 10^{18} n_e e A_p T_e^{1/2} m_i^{-1/2} \left[\frac{1}{2} (\frac{2m_i}{\pi m_e})^{1/2} \exp \frac{e(V - V_p)}{T_e} - \frac{A_s}{A_p} \exp(-\frac{1}{2}) \right] \tag{4.1}$$

where I and V are the probe current and sweeping voltage; A_p is the area of the probe tip; A_s is the area of the sheath surface around the probe tip; the n_e, T_e and V_p are the electron density, electron temperature and plasma potential, respectively; m_i and m_e are the masses of the ion and electron.

When the biased voltage scans from $-150 \sim 0V$, then a typical Langmuir probe I-V curve is obtained. By fitting the I-V curve according to Eq. (4.1), the electron temperature and density are estimated. When the probe is placed in the plasma, a sheath around the probe forms; inside of this sheath $n_i \neq n_e$ and large electric fields can occur, while outside of this sheath $n_i \approx n_e$ and only much weak electric fields can exist. The sheath thickness x_s is a few λ_D ($\sim 3.29\lambda_D$) while $\lambda_D \sim 0.01mm$ is the Debye length for the helium plasmas studied here in PISCES-A. For a cylindrical probe, the area of the sheath satisfies $A_s = A_p(1 + \frac{x_s}{a})$[20], where a is the probe radius, $\sim 0.75mm$. For our conditions, the sheath area A_s is about $1.04A_p$ and thus the sheath area effect is so small that it may be neglected here. As a result, the probe tip area is a good approximation to the sheath area surrounding the probe tip, that is, $\frac{A_s}{A_p} \sim 1$. Applying this approximation, the I-V characteristic in Eq.(4.1) is fitted to estimate the electron density and temperature.

4.1.3 Plasma Density and Temperature

The raw probe data are fitted by the Eq.(4.1) with the parameters n_e, T_e and V_p, allowing all three parameters to be obtained by one fitting. Fig. 4.2 shows the I-V curve fitting of data from the upstream probe for a pure helium plasma. The deviation of the data from the model (Eq.(4.1)) can be used to find the errors of electron density and electron temperature. Fig.4.3 presents the results of electron temperature and density at the upstream port for 0% H_2 case by fitting the raw data. The errors of n_e and T_e are in the range of $10 \sim 20\%$.

The deviation of the measured current from the model current is given as

$$\sigma = \sqrt{\frac{\sum_{i=1}^{N}(I_i - I_i^*)^2}{N_{total} - N_{parameter}}} \tag{4.2}$$

where σ is the error of fitting the measured data with the model Eq.(4.1).

The relative error in the inferred density and electron temperature due to random or stochastic deviation in the measured data, $I_i(V)$, are given as

$$\varepsilon_{n_e} = \sqrt{\frac{\sum_{i=1}^{N}(I_i - I_i^*)^2}{\sum_{i=1}^{N}\left(\frac{\partial I_i^*}{\partial n_e} \cdot n_e^{fit}\right)^2}} \tag{4.3}$$

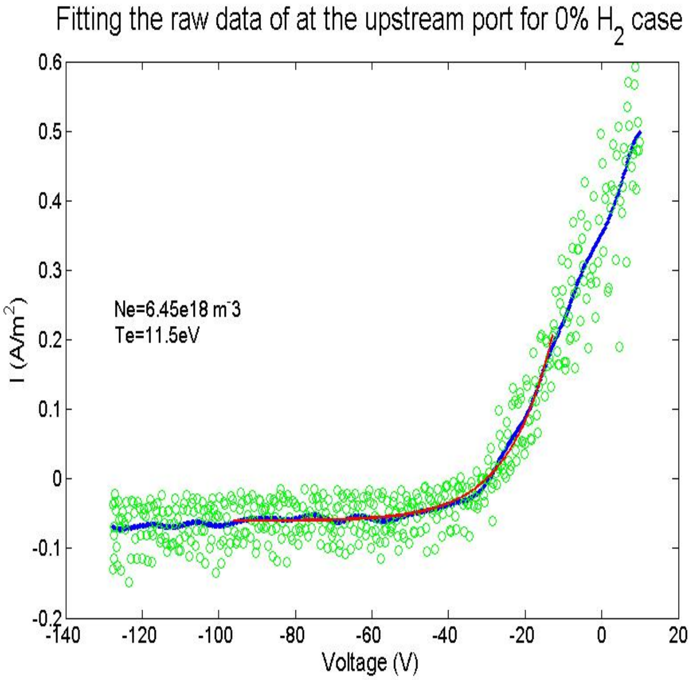

Figure 4.2: Using I-V curve to fit the probe raw data of the upstream probe data in the floating potential region for the 0% H_2 case.

and

$$\varepsilon_{T_e} = \sqrt{\frac{\sum_{i=1}^{N}(I_i - I_i^*)^2}{\sum_{i=1}^{N}\left(\frac{\partial I_i^*}{\partial T_e}\cdot T_e^{fit}\right)^2}} \tag{4.4}$$

where I_i is the measured raw data point; I_i^* is the value of this model at the same probe voltage, which is considered as the real value of the current; N_{total} is the number of data points; $N_{parameter}$ is the number of parameters to be fitted; and n_e^{fit} and T_e^{fit} are the fitted density and electron temperature.

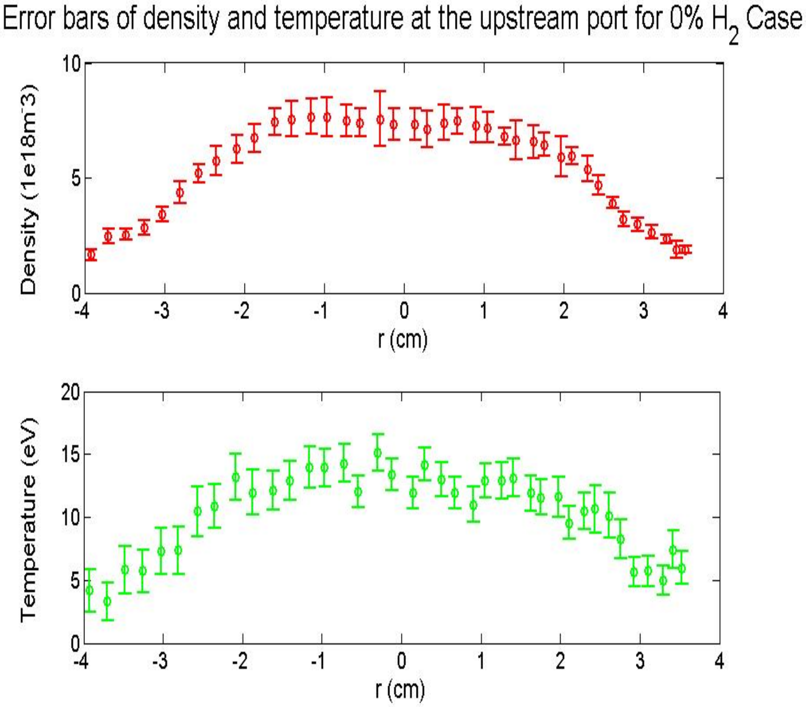

Figure 4.3: Error bars of the electron density and temperature at the upstream port for 0% H_2 case

By averaging the results obtained from a series (20 $\sim$ 25) of repeated measurements, the random error can be reduced in the particle balance. Fig. 4.4- Fig.4.7 show the radial profiles of electron temperature and density obtained in this way for all cases. The red lines are the densities and temperatures of the plasma close to the upstream port. The green are the results of the downstream probe. The blue lines are the mean of the results obtained from a series of repeated measurements. As a result, the error bar is reduced to $\sim 4\%$. The systematic error of probe measurements for electron density and electron temperature always exists. A systematic error in the range of 10%-20% does not invalidate the conclusion in this thesis.

In pure He discharges, the source gas pressure is 6.3mTorr and the target gas pressure is 7.3 mTorr. The profiles of density and temperature are shown as Fig.4.4. For pure helium plasma, the density is about $7 \times 10^{18} m^{-3}$ and the temperature is 12.5eV in the center of plasma column at the upstream port. For the downstream location, the density is lower, but no significant difference is seen in T_e. When H_2 gas is introduced into the target region (Fig. 4.5- Fig.4.7), the total target gas pressure varies from 7.3 mTorr up to 8.3mTorr while the source gas pressure stays at 6.3mTorr. The density develops a significant axial gradient, which becomes significantly larger as H_2 is added. The electron temperature does not exhibit a significant axial gradient, but does decrease slightly as H_2 is added to the discharge. This axial gradient is the beginning of the detachment process which, in our experiments, is not allowed to fully develop since the physics of interest can be studied without complete detachment.

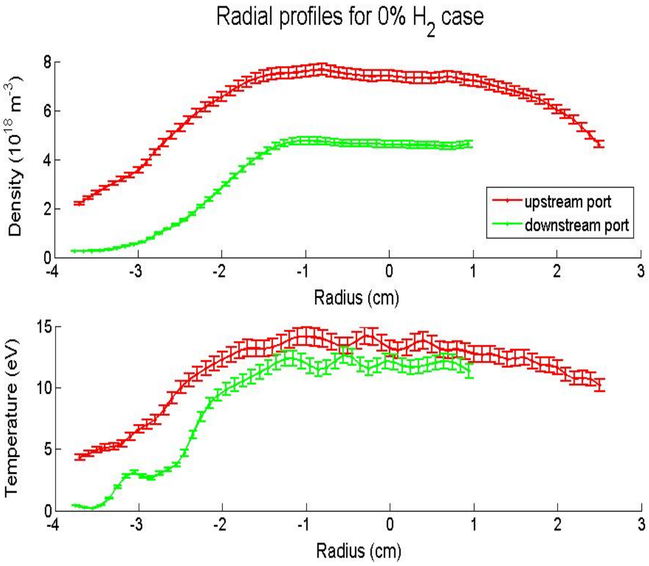

Figure 4.4: The radial profiles of electron temperature and density for different cases. The red lines are the densities and temperatures of the plasma close to the upstream port. The green are the results of the downstream probe. The blue lines are the averaged results of a series of repeated measurements. 0% H_2 case.

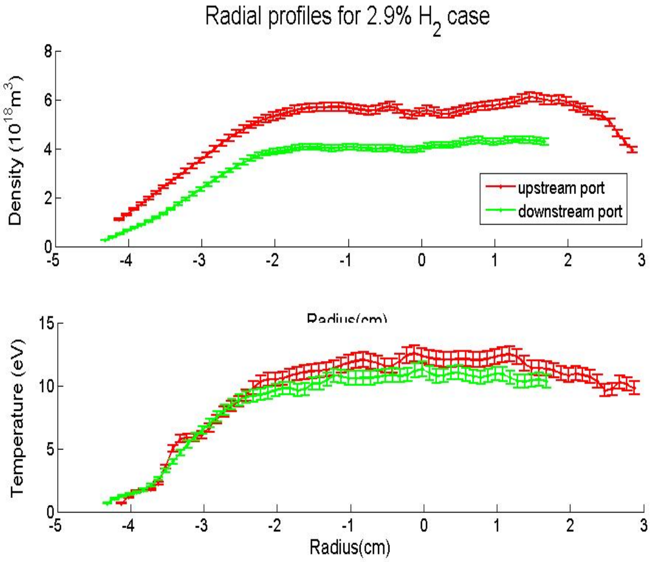

Figure 4.5: 2.9% H_2 case

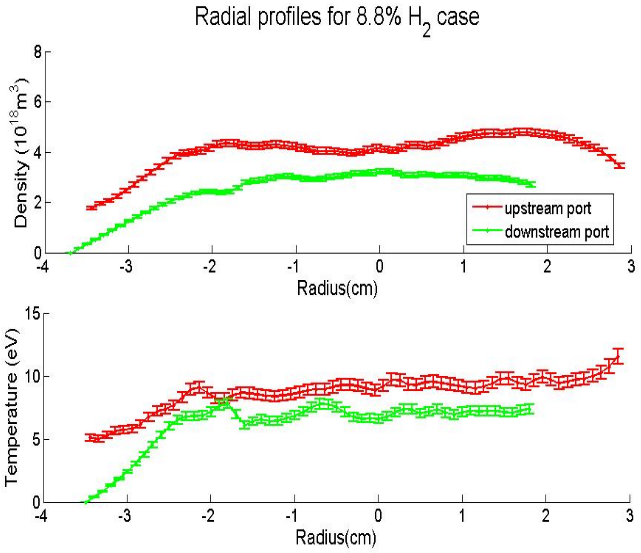

Figure 4.6: 8.8% H_2 case

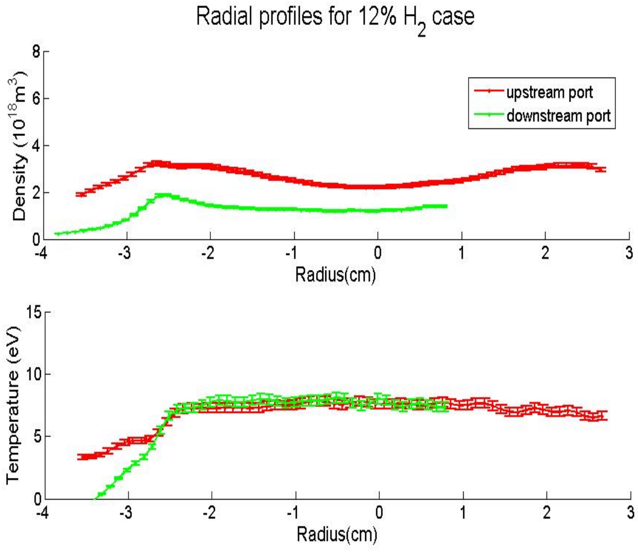

Figure 4.7: 12% H_2 case

4.2 Cross-field Particle Flux to the Chamber Wall

4.2.1 Diagnostics

The cross-field flux to the chamber wall is estimated by two sets of wall probe arrays [17]. As shown in Fig.2.4, there are three wall probes on the side port wall and one on the facing wall, which are located in the vertical plane of the center of the plasma. Therefore, the flux is measured by the wall probes at four axial positions for the two side ports as shown in Fig.2.2. They are 99cm, 107cm, 121cm and 130cm away from the cathode.

Each wall probe is a $75.3mm^2$ copper plate isolated from the wall by a 0.5mm thick Teflon sheet. For the set of three wall probes, they are respectively 6.5mm, 21.5mm and 36.5mm deep into the side port from the chamber wall as in Fig.2.3 and Fig.2.2. Applying a -150V biased voltage to the wall probe, the ion saturated current is collected through a 100 Ω resister. All the ions arriving on the wall of the side port are transported radially across the magnetic field from the halo region by turbulent fluctuations [1].

4.2.2 Basic Theory to Interpret Wall Probe Data

Fig.4.8 shows the radial profile of I_{sat} obtained with the scanning Langmuir probe. The inset plot indicates clearly that the I_{sat} decreases exponentially in the region far away from the center, although the decay rates are different for $r \geq 8.5cm$ and $r \leq 8.5cm$. Therefore, we can assume that the ion saturation current collected by the wall probes satisfies an exponential decay versus the radial position as Eq.(4.5).

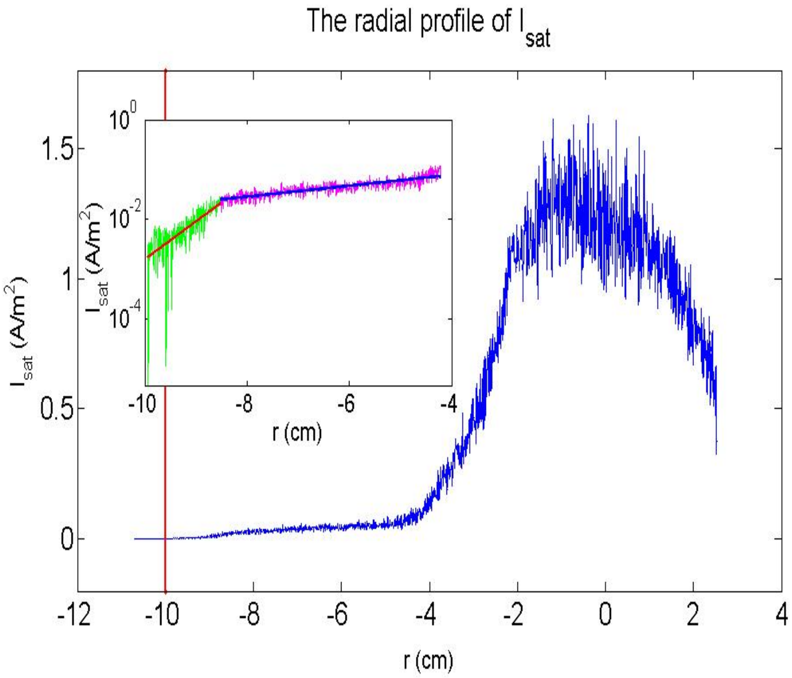

Figure 4.8: The radial profile of I_{sat} with the scanning probe at the upstream port. The inset plot is a log plot of the data close to the chamber wall.

$$I(y) = I_0 exp(-\frac{y}{\lambda_r}) \tag{4.5}$$

where $y = r - r_{wall}$ is the distance into the side port from the chamber wall, that is, $y = 0$ on the chamber wall locates at radius r_{wall}; and λ_r is the decay length.

Since there is no significant volumetric source and sink in the port region, the radial flux only depends on the depth into the side port, and thus the total rate of particles entering the side port can be estimated from particle balance as Eq.(4.6).

$$\int_0^\infty \frac{I_0}{A_w} exp(-\frac{y}{\lambda_r}) dy = \Gamma_r \frac{W_p}{2} \tag{4.6}$$

where W_p is the width of the port and A_w is the area of the wall probe.

Using Eq.(4.5) in this integral, the local radial flux can be rewritten as given in Eq.(4.7). Here Γ_r denotes the cross-field transport at the axial position $z = Z_p - \frac{W_p}{4}$, where z_p is the axial position of the centerline of the side port. Assuming the decay length is same as the opposing wall in the side port, the radial flux at axial position $z = Z_p + \frac{W_p}{4}$ is estimated from the available wall probe on the facing wall of the side port.

$$\Gamma_r = \frac{2\lambda_r I_0}{W_p A_w} \tag{4.7}$$

This procedure then allows Γ_r to be determined at four axial locations from the measured decay length λ_r, the ion saturation curent I_0 at radius r_{wall}, and the port and chamber geometry.

4.2.3 Cross-field Transport to the Chamber Wall

The wall probes are 6.5mm, 21.5mm and 36.5mm deep into the side port from the chamber wall, respectively. The deepest probe tip can not get an effective current because it is so far away from the plasma column that few ion particles can reach there. Fig.4.9 displays the fitting curve of the raw data of wall probes at the upstream port for 0% H_2 case using Eq.(4.5). The radial flux to the wall here is about $3A/m^2$ and the decay length is 1cm. According to the obtained decay length and raw data, it can be derived that the voltage on the deepest probe tip with a 100 Ω resister is around 2mV, at least 50 times smaller than that of the tip close to the chamber wall.

The radial fluxes at the upstream port for all cases are presented in Fig.4.10. Similarly, the radial fluxes to the wall at the downstream port can be obtained. The decay length within the upstream port is about 1cm; while it is $2 \sim 2.5cm$ in the downstream port. Using these measurements with the model described above, we then infer the total cross-field radial transport flux at the different locations; the results are shown in Fig. 4.11.

Fig. 4.11 presents the radial flux to the wall along the axis of the chamber for different cases. The horizontal axis indicates the distance from the cathode. From Fig.4.11, we see that as the H_2 percentage is increased, the radial flux increases, reaches a peak at 5.9% H_2, and then decreases as the H_2 fraction increases further. We also observe that the cross-field flux decreases as the distance from the cathode is increased. This result is discussed in the Chapter 6.

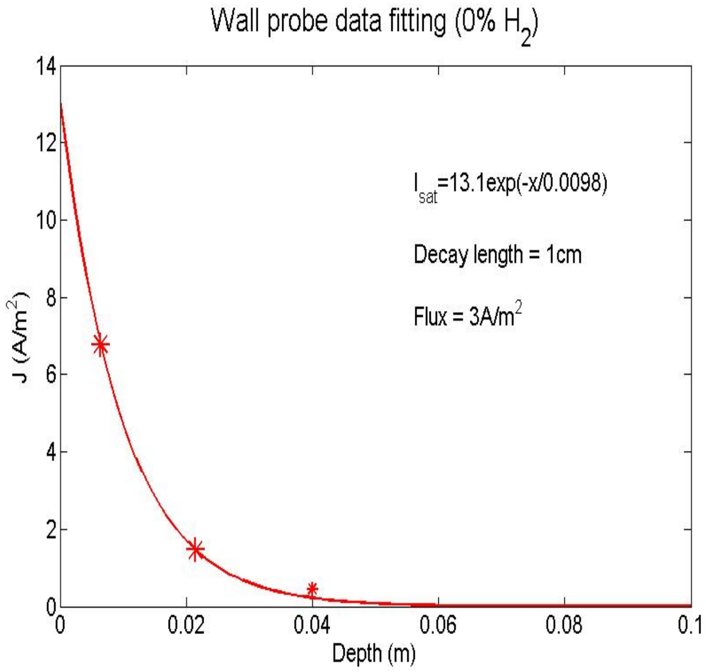

Figure 4.9: Fitting the upstream wall probe data to estimate the radial flux to the wall for the 0% H_2 case with Eq. 2. The horizontal axis is the depth into the side port from the chamber wall.

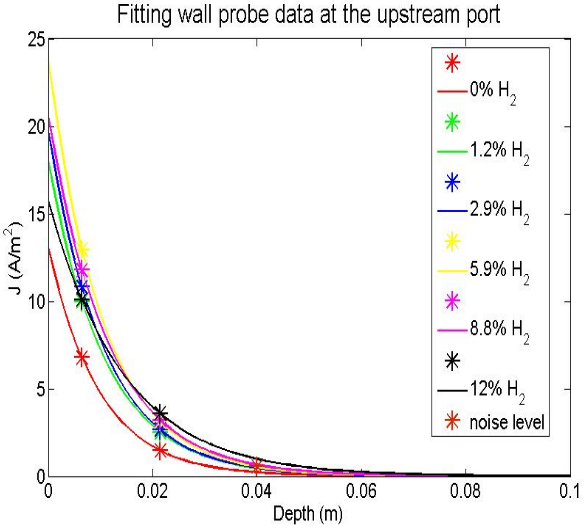

Figure 4.10: Fitting the wall probe data at the upstream port for all cases. The decay length λ_r is about 1cm. The stars are the wall probe data and the data from the third wall probe are in noise level.

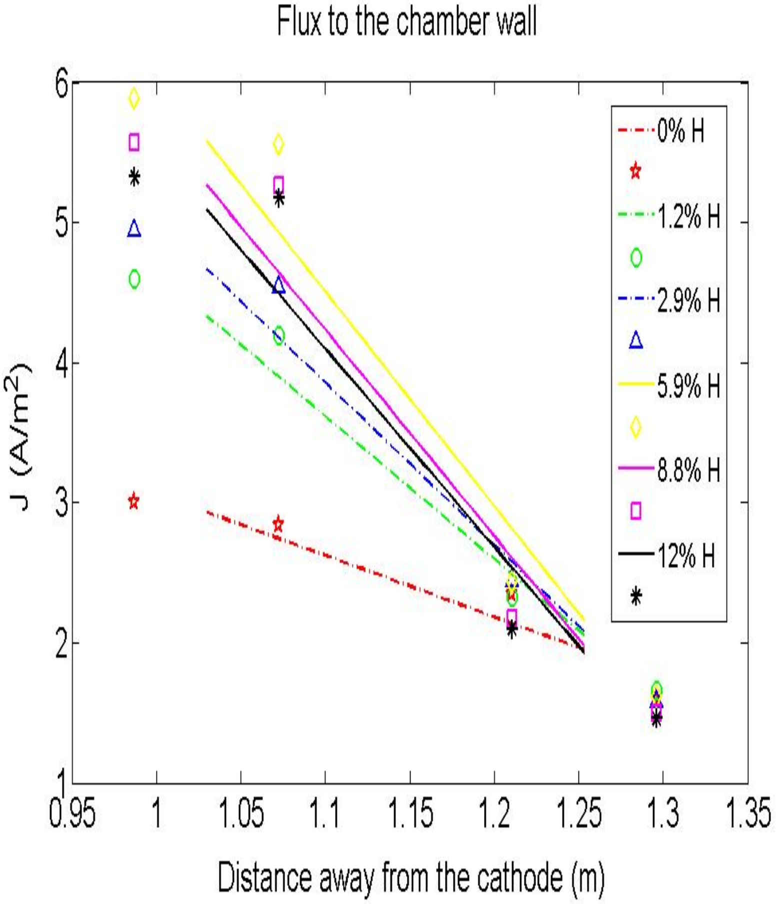

Figure 4.11: Radial fluxes to the wall along the chamber for all cases.

4.3 Axial Flow Speed of the Plasma

4.3.1 Diagnostics

Axial flow speed is required to estimate the axial flux used in the particle balance. Doppler shift on the spectral line (468.5nm) measured by a Czerny-Turner spectrometer is used to measure the bulk flow velocity. In order to observe the Doppler effect, two mirrors are mounted on the wall of each side port as shown in Fig.2.6 and Fig.4.12. The two mirrors at the upstream port are made at an angle of 28° with respect to the normal of the chamber wall as in Fig.4.12; while those at the downstream port are at 24°. The measurements are made with a 1.3m Czerny-Turner spectrometer employing a 1200 lines/mm grating operated in second order to give dispersion of 0.06 Angstrom/pixel.

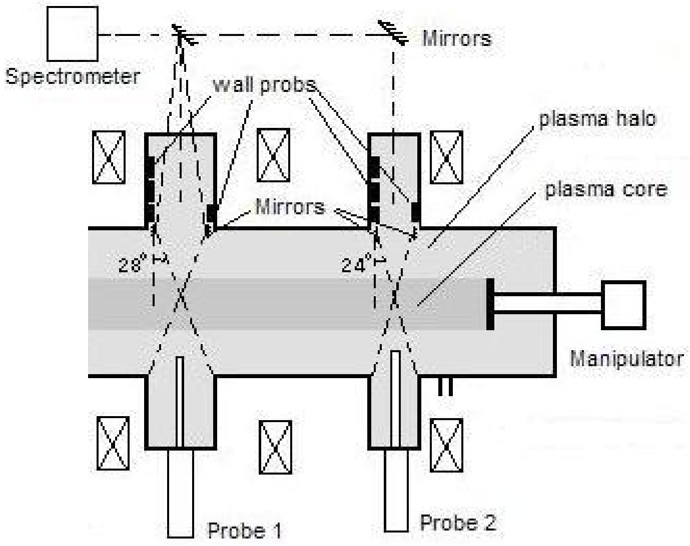

Figure 4.12: The mirrors mounted on the side wall to observe the plasma flow.

4.3.2 Basic Theory

If the velocity parallel to the line of sight is significant, the emission line will shift from the usual spectral position. Since the Stark effect and Zeeman effect are negligible for PISCES-A, it is feasible to estimate the axial flow speed by Doppler shift $\Delta\lambda$ by Eq.4.8. The axial flux is then easy to be calculated with $\Gamma_r = n_e v_a$.

$$\frac{\Delta\lambda}{\lambda_0} = \frac{v_a}{c} \tag{4.8}$$

where v_a is the bulk flow speed; c is the speed of light; and $\lambda_0 = 468.5nm$ is one of the wavelengths of He^+ emission lines.

It is difficult to measure the absolute wavelength with sufficient accuracy to calculate the line shift. As a result, in these experiments, one view is made orthogonal to the magnetic field to provide an unshifted line emission spectrum, while a second view is made at an angle of 28° at the upstream port or 24° at the downstream port with respect to the normal of the chamber wall as in Fig.4.12 to observe the Doppler shifted line emission. The difference between two views is the Doppler shift subject to the angle between the path of the light and the plasma flow. The axial flow speed is calculated by Eq.(4.8).

4.3.3 Axial Flow Speed

In order to get a better resolution of the line shift, the measurement of the Doppler shift is operated in second order of He^+ emission $\lambda = 4685$Å employing a 1200 lines/mm grating. The fine structure includes 13 lines given in Table 4.1. The Doppler shift can be estimated by fitting the Eq.(4.9) [24].

Table 4.1: Fine structures of He^{+} emissions

Wavelength(Å)	A_{ki}	g_k	Transition
4686.688182	9.38E+07	4	3p-4d
4686.718573	4.90E+07	4	3s-4p
4686.835773	9.79E+06	2	3p-4s
4686.879396	4.91E+07	2	3s-4p
4687.015269	2.06E+08	6	3d-4f
4687.015800	1.13E+08	6	3p-4d
4687.068513	5.56E+05	4	3d-4p
4687.069408	1.88E+07	4	3p-4d
4687.115538	2.21E+08	8	3d-4f
4687.1423432	1.47E+07	6	3d-4f
4687.195590	5.01E+06	4	3d-4p
4687.217023	1.96E+07	2	3p-4s
4687.229361	5.57E+06	2	3d-4p

$$I(\lambda) = I_0 \sum_{l=1}^{13} g_l A_l exp \left\{ - \left(\frac{\lambda - \lambda_0 - \lambda_l}{\lambda_{1/e}} \right)^2 \right\} \tag{4.9}$$

where λ_l, A_l and g_l are the wavelength, Einstein coefficient and the statistical weight of the upper level. Line label l is from 1 to 13. The fitting parameters are the

Doppler shift λ_0, the amplitude I_0 and the gaussian line broadening $\lambda_{1/e}$.

However, due to the resolution of the PISCES-A spectrometer, it is very hard to determine the absolute shifted wavelength of the fine structure. Therefore, the spectroscopic raw data are fitted with multi-gaussian components as Eq.(4.10). The difference of b_i obtained by fitting the raw data of two views is the Doppler shift in pixel subject to the angle between the views.

$$I = \sum_{i=1}^{k} a_i \exp\left[-\left(\frac{x-b_i}{c_i}\right)^2\right] \tag{4.10}$$

where I is the relative intensity of the emission; x is the pixel; a_i, b_i and c_i are the fitting parameters; i is the order of the gaussian fitting; and k is the number of gaussians used.

Fig.4.13 shows the dispersion relation of emission lines with different wavelengths, which can be fitted by Eq.(4.11). The Doppler shift is then calculated with the dispersion relation and the shifted pixel obtained above.

$$dispersion(nm/pixel) = 6.7\times10^{-3} + 3.77\times10^{-6}\lambda - 1.15\times10^{-8}\lambda^2 \tag{4.11}$$

Fig.4.14 shows the fitting with multi-Gaussian components (up to 6 Gaussian components) to the spectroscopic raw data at the upstream port for pure He plasma, the 0% H_2 case. The red circles are the data from the mirror very close to the source, which makes a view at an angle of 28° with respect to the normal of the chamber wall. The green circles provide an unshifted line emission spectrum from the light perpendicular to the magnetic field. The blue lines present qualitatively the spectral profile of

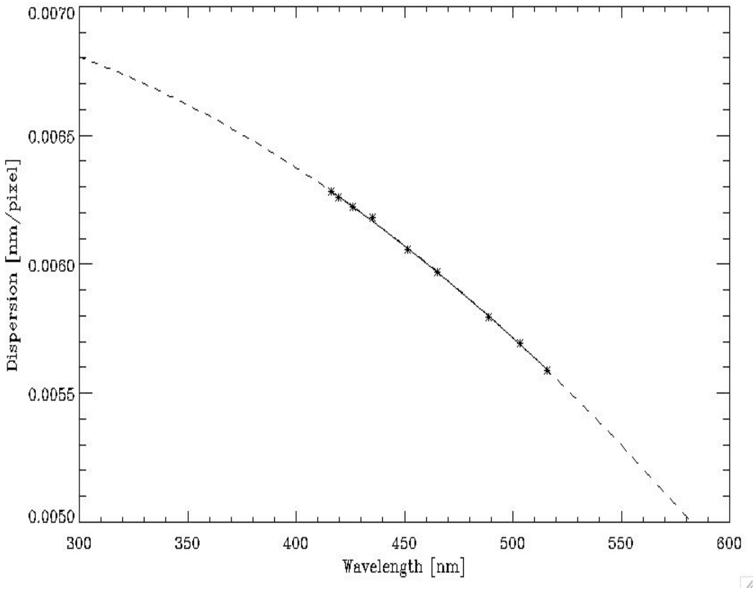

Figure 4.13: The dispersion relation for the second order of different emission lines in the PISCES-A spectrometer. (from D. Nishijima)

fine structures according the Table 4.1. The results shown in Fig. 4.14 show a typical set of such measurements, and indicate that a Doppler shift, $\Delta\lambda = 0.013\text{Å}/cos(62^\circ) = 0.028 \pm 0.002\text{Å}$ exists for the condition and location. The actual average flow velocity is about $1.79 \pm 0.1 km/sec$ away from the source region, which is larger than the measured Doppler shift since the spectrometer view is not parallel to the flow. The corresponding error can be estimated by Eq.(4.12) similar to Eq.(4.3) and (4.4).

The relative error of the Doppler shift measurement is given in

$$\varepsilon_{\Delta\lambda} = \sqrt{\frac{\sum_{j=1}^{N}(I_j - I_j^*)^2}{\sum_{j=1}^{N}\left(\sum_{i=1}^{k} a_i \exp\left[-\left(\frac{x-b_i}{c_i}\right)^2\right]\cdot\frac{2(x-b_i)}{c_i^2}\right)^2}} \tag{4.12}$$

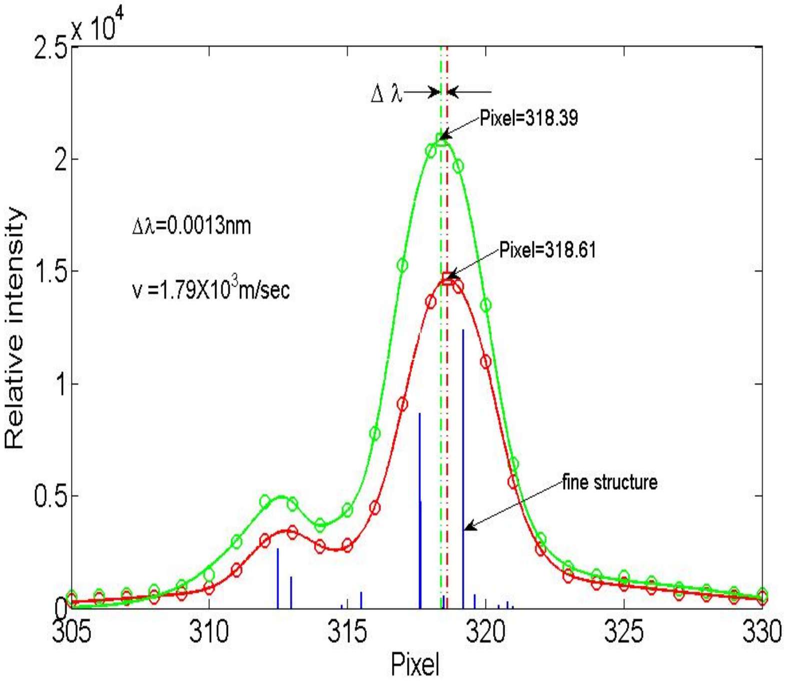

Figure 4.14: Fitting the spectroscopy data with multi-Gaussian components to obtain the Doppler shift. The red circles are the data from the mirror very close to the source for the 0% H_2 case. The green circles are the data from the light perpendicular to the magnetic field. The blue lines show qualitatively the spectral profile of fine structures.

where I_j is the measured relative intensity; I_j^* is the value of this model at this point, which is considered as the real value; x is the pixel; a_i, b_i and c_i are the fitting parameters; i is the order of the gaussian fitting; and j is the index of data points.

By analyzing these measurements at different vertical displacements to the plasma center, the profile of the flow speed can be found. Fig.4.15 and Fig.4.16 show the radial profiles of the axial flow speed for different cases, although the values at different heights of the chamber are still line-averaged as Fig. 4.17. Since the flow speed does not vary much radially for $r < 3cm$, the vertical displacement can be referred to as radius. The error bars are calculated from the relative error. From Fig.4.15, the flow speed does not change at the upstream port as H_2 is injected. For pure helium plasma, the speed at the downstream port is larger than that at the upstream port. When the H_2 gas is flowing into the chamber, the downstream flow speed decreases rapidly to the same level as the flow speed at the upstream port. The results are shown in Fig.4.16.

Overall, the flow speed of the core plasma is nearly flat in the radial direction, showing only a slight increase at the edge of the core plasma column, which has also been seen in previous experiments [61]. The axial flow speed at the upstream port does not vary too much when the H_2 is injected into the target chamber; while the flow speed at the downstream port is reduced quickly.

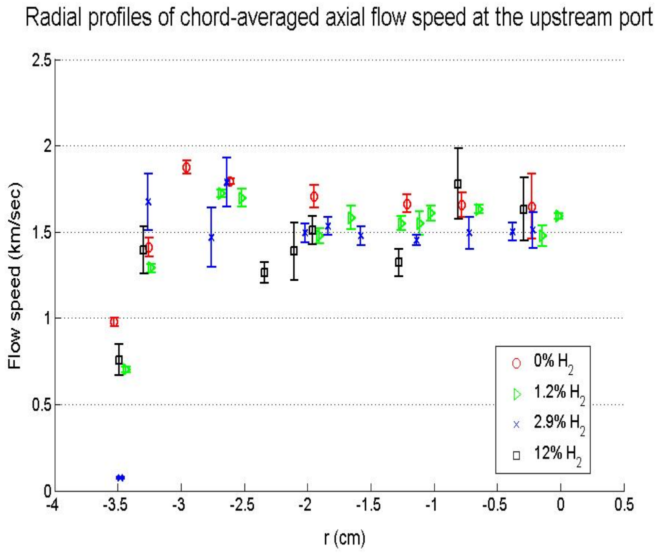

Figure 4.15: The line-averaged flow speed obtained by analyzing the spectroscopy data of different vertical pixels. Radial profiles of axial flow speed at the upstream port.

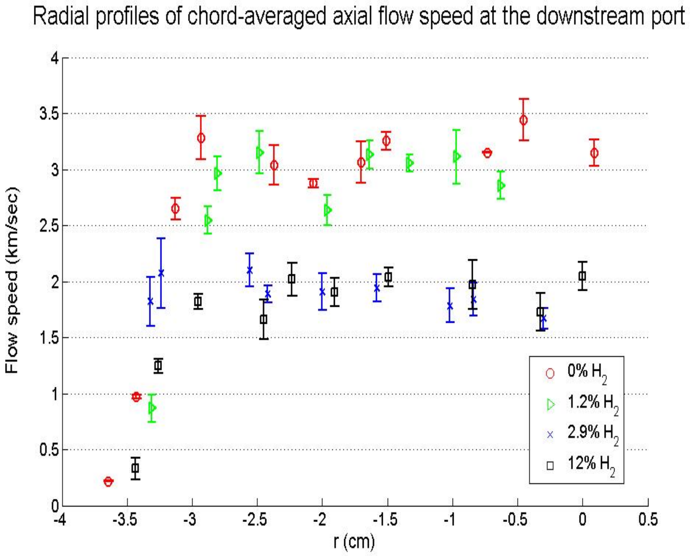

Figure 4.16: The line-averaged flow speed obtained by analyzing the spectroscopy data of different vertical pixels. Radial profiles of axial flow speed at the downstream port.

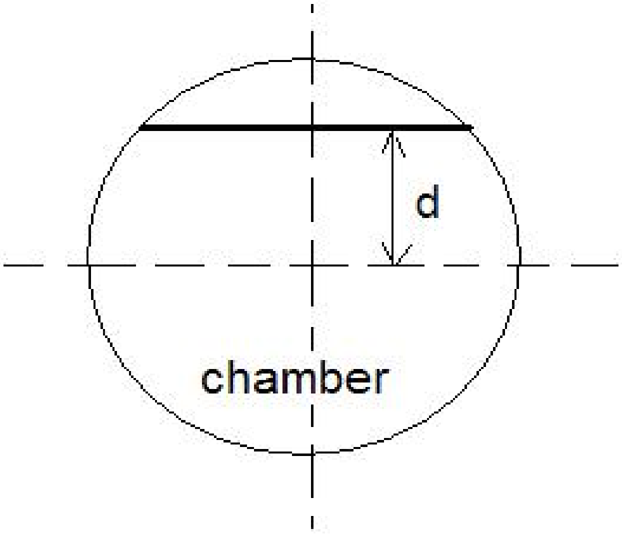

Figure 4.17: The path of the light measured by the spectroscopy. d is the vertical displacement.

4.4 Measurements of Low Temperature in the Halo Region

4.4.1 Diagnostics

In the halo region of the plasma, the electron temperature is too low ($< 1eV$) to be reliably measured by our Langmuir probes. Since the electron temperature T_e is required to estimate to the EIR sink in the cold halo region, the temperature at large radii is evaluated by the emissions from a series of state populations of He neutrals in highly excited states [16], which are estimated by the measurements of the emissions of He neutral transitions and the corresponding transition coefficients [2]. The light of plasma emission is viewed through the view ports in Fig. 4.12 and measured by the Czerny-Turner spectrometer nearby PISCES-A. The measured lines correspond to the transitions of excited helium neutrals for $n = 7$ to $n = 15$, which are listed in Table.4.2.

Table 4.2: Emission lines of He neutral transitions

Transition	Wavelength(nm)	A_{ki}	g_k	Upper state energy (eV)
15d-2p:T(triplet)	347.9	3.814×10^5	15	24.527
14d-2p:T(triplet)	348.8	4.736×10^5	15	24.518
13d-2p:T(triplet)	349.9	5.940×10^5	15	24.507
12d-2p:T(triplet)	351.3	7.570×10^5	15	24.493
11d-2p:T(triplet)	353.1	9.880×10^5	15	24.475
10d-2p:T(triplet)	355.4	1.310×10^6	15	24.451
9d-2p:T(triplet)	358.7	1.815×10^6	15	24.419
8d-2p:T(triplet)	363.4	2.610×10^6	15	24.375
7d-2p:T(triplet)	370.5	3.952×10^6	15	24.310
3d-2p:S(singlet)	667.8	6.380×10^7	5	23.074

4.4.2 Basic Theory

If the atoms in all possible states are in the Boltzmann distribution and the radiation energy density corresponding to all the possible corresponding transitions has the blackbody spectrum corresponding to the system temperature, the system is said to be in thermal equilibrium. However, it is very difficult to achieve such an equilibrium for laboratory plasmas. Therefore, a less complete form is defined, which is called local thermodynamic equilibrium (LTE). In LTE, the state populations satisfy the Boltzmann distribution as Eq.(4.13) while the radiation is not restricted to be in thermal equilibrium with the kinetic temperature.

$$\frac{N_n}{g_n} = \frac{N_i}{g_i} \frac{h^3 N_e}{2\pi m_e {T_e}^{3/2}} exp\left(\frac{\Delta E_n}{T_e}\right) \tag{4.13}$$

where N_n is the total level density, N_i is the ion density, g_n is the statistical weight of the level n, ΔE_n is the ionization energy of the level n, g_i is the statistical weight of the ion, and T_e is the electron temperature.

Unfortunately, the LTE condition is still too restrictive for the conditions of our experiments, and is rarely satisfied for low-lying levels in magnetic fusion plasmas. However, it may be satisfied between high principal quantum levels due to the small value of ΔE for these types of transitions, which can be considered to be in partial local thermodynamic equilibrium (pLTE). To measure T_e in the halo region, we thus first assume that the state populations of Helium neutrals in the halo region are in pLTE and satisfy Eq.(4.13) and find T_e using the measured line emission distribution. Using this result with the probe measurements of density, we then verify that the pLTE assumption is correct after the fact. As a result, the electron temperature can be estimated by measuring the line emission intensities ($\propto N_n$) for various high n transitions, which will vary with ΔE_n as in Eq.(4.14). The factor $\frac{1}{T_e}$ is then given by the slope of $ln\left(\frac{N_n}{g_n}\right)$ vs. ΔE_n.

$$ln\left(\frac{N_n}{g_n}\right) \sim \Delta E_n/T_e \tag{4.14}$$

which then gives

$$1/T_e \sim \frac{ln\left(\frac{N_n}{g_n}\right)}{\Delta E_n} \tag{4.15}$$

When performing a spectroscopic data analysis for state populations, the relative intensities of emission lines measured by the spectrometer need to be calibrated to account for the sensitivity with wavelength. The intensity calibration is implemented by a standard light source with known spectral emission. In this experiment, the Calibration Source Optics Head (model: 456-12-1) is used and the absolute calibration data from the manufacturer is plotted in Fig.4.18. The standard radiance dependent on wavelength is obtained from the manual of the integrating sphere. The line intensities in unit $Watts/(sec \cdot cm^2 \cdot sr \cdot nm)$ can then be converted into $\frac{photons}{sec \cdot cm^2 \cdot sr \cdot \mathring{A}}$. Using the standard radiance (STD) with wavelength obtained from the manufactory of the integrating sphere, the corresponding absolute intensity can be calculated by Eq.(4.16).

$$Absolute\ Intensity\left(\frac{photons}{sec \cdot cm^2 \cdot sr \cdot \mathring{A}}\right) = \frac{STD \cdot Measured\ data\ (counts/sec)}{Calibration\ data\ (counts/sec)} \tag{4.16}$$

4.4.3 The Electron Temperature in the Halo Region

Fig.4.19 shows the highly excited helium neutral emissions from n=10 to n=14 transitions for the 0% H_2 case. Applying Abel inversion to the spectroscopy data, the radial resolution of the intensities of high n emission lines is obtained. Assuming that the electrons in sufficiently upper states are in partial local thermodynamic equilibrium

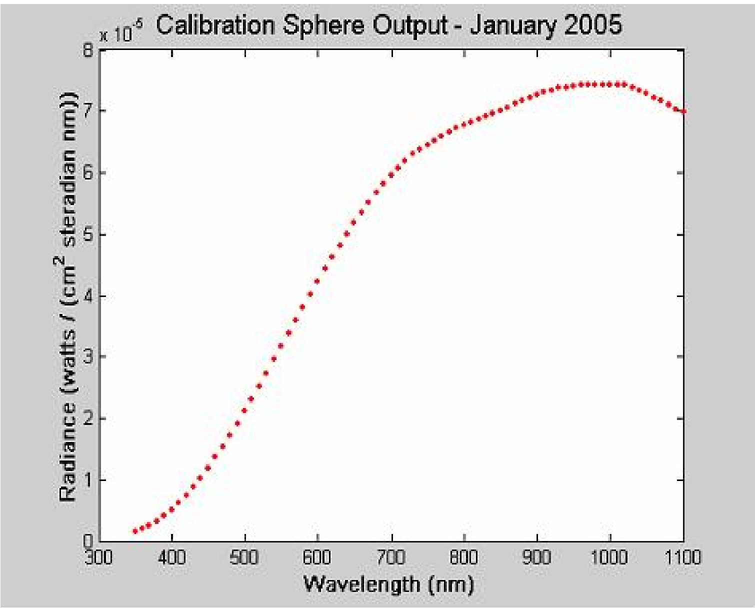

Figure 4.18: Absolute calibration data from the manufacturer. Radiance at different wavelengths.

(pLTE) with unbound electrons, the populations follow the Saha-Boltzmann distribution in Eq.(4.13) [54, 13]. The temperature at large radii is then derived by Eq.(4.15).

Fig.4.20 presents $ln\left(\frac{N_n}{g_n}\right)$ vs. ΔE_n for the pure He case, and shows that the electron temperature in the halo region is about 0.12eV by evaluating the helium neutral emissions from n=7 to n=13 transitions. The density in the halo region is $\sim 10^{17} m^{-3}$, about 30 times less than in the center, estimated from the probe ion saturation current and these spectroscopic measurements of the temperature in the halo region. The results of electron temperature and density in the halo region can be used to verify the assumption of pLTE above. Eq.(4.17) is the criterion of pLTE [13], which means those higher excited states above a critical quantum number n are in partial local thermodynamic equilibrium (pLTE) and the Eq.(4.13) is satisfied.

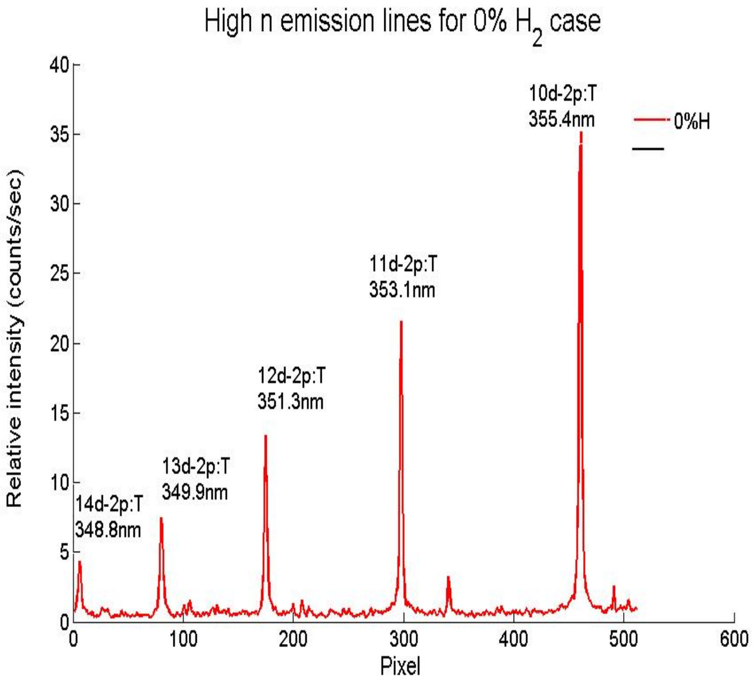

Figure 4.19: Measured emission lines from high excited He neutral transitions in the halo region for the 0% H_2 case.

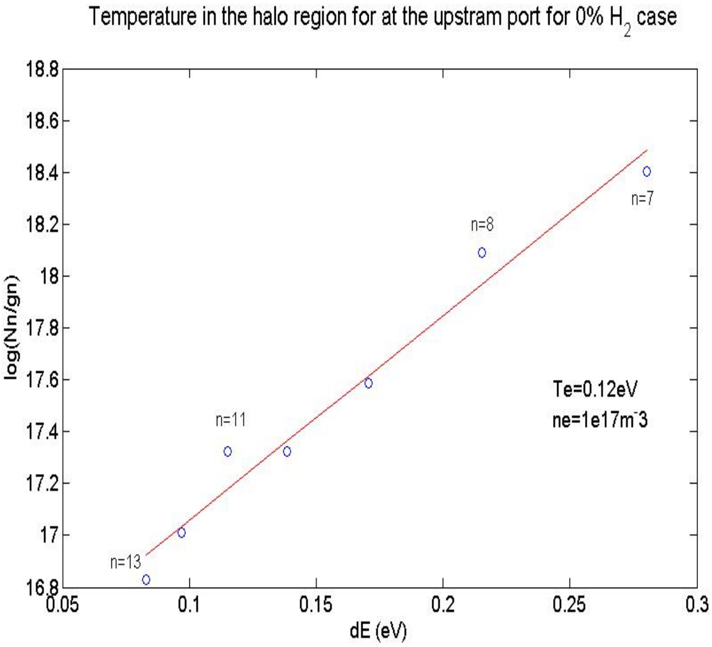

Figure 4.20: Estimation of the low electron temperature at Radius=6cm in the halo region with Eq.(4.15) for the 0% H_2 case.

To achieve pLTE in halo region, we require

$$n_e \geq \frac{10}{2\pi^{\frac{1}{2}}} \frac{z^7}{n^{\frac{17}{2}}} \left(\frac{\alpha}{a_0}\right) \left(\frac{kT_e}{E_H^z}\right)^{\frac{1}{2}} \tag{4.17}$$

where n, n_e and T_e are the principal quantum number, electron density and temperature, respectively. $z = 1$ is the ionization state; the fine structure constant $\alpha = \frac{e^2}{\hbar c} = \frac{1}{137}$; the Bohr radius $a_0 = 0.53\mathring{A}$ and the Rydberg energy $E_H^z = \frac{z^2 e^2}{2a_0} = 13.6eV$.

Solving for n, we find

$$n \geq 142.24 \left(\frac{T_e}{n_e^2}\right)^{\frac{1}{17}} \tag{4.18}$$

where T_e in eV and n_e in cm^{-3}; n is the principal quantum number.

Using $n_e = 10^{17} m^{-3}$ and $T_e = 0.12eV$ obtained above, we find that the critical principle quantum number is 6, that is, the assumption of pLTE on $n = 7 \sim 13$ is valid.

Overall, measurements across the halo region show that the electron temperature is very flat, and is insensitive to the core plasma conditions.

ACKNOWLEDGEMENT

Chapter 4, in part, has been submitted for publication of the materials as it may appear in Physics of Plasmas, 2008, Laizhong Cai, George Tynan, Eirc Hollmann. The dissertation author was the primary investigator and author of this paper.

5

Measurements of Recombination and Ionization

Due to the low electron temperature ($< 1eV$) in the halo region, the volumetric recombination mainly occurs in this region, while the ionization takes place mainly in the hot ($\sim 10eV$) core region. Measurements of both types of processes, required to implement particle balance analysis, are presented in this chapter..

5.1 Electron-Ion Recombination Sink

5.1.1 Diagnostics

In this experiment, the spectroscopic data of EIR are measured by the PISCES-A spectroscopy, a Czerny-Turner spectrometer (model 209). The measured spectral line is the emission from Helium neutral transition ($11^3d - 2^3p$) at 353.1nm which is observed through two view ports as shown in Fig.2.2. The instrument is equipped with a 2D detector, and has the slit imaged onto a vertical chord. In this way, spatially resolved spectra can be obtained across the plasma column.

5.1.2 Basic Theory

Volumetric recombination in laboratory plasmas includes radiative recombination, three-body recombination and dielectronic recombination. Recently, the molecular-activated recombination has been observed on different fusion devices. Dielectronic recombination is a process by which an atom captures an electron into an upper energy level while using the electron's excess energy to excite another electron already in the atom to an upper level. Since this process is usually observed only in a very hot plasma $(> 100eV)$, the dielectronic recombination is negligible under the plasma condition ($\sim 10eV$) in PISCES-A. The radiative recombination process and three-body recombination, which are collectively referred to as Electron-Ion Recombination (EIR), are presented in Eq.(5.1) and Eq.(5.2), respectively. In He/H plasmas, molecular-activated recombination, so-called MAR, usually occurs via Eq.(5.3) and Eq.(5.4).

$$He^+ + e \rightarrow He + hv \qquad radiative \quad recombination \tag{5.1}$$

$$He^+ + e + e \rightarrow He^* + e \qquad He^* \rightarrow He + hv \qquad three-body \quad recombination \tag{5.2}$$

$$H_2(\nu) + He^+ \rightarrow H + HeH^+ \qquad followed\ by \qquad HeH^+ + e \rightarrow H^* + He \tag{5.3}$$

$$H_2(\nu) + e \rightarrow H + H^- \qquad followed\ by \qquad He^+ + H^- \rightarrow H^* + He \tag{5.4}$$

The first, recombination of atoms into a molecule with simultaneous ionization (associative ionization) is more important than Hydrogen atom ionization. From an energy point of view, this process has an advantage over the other in that it requires the expenditure of less energy than the ionization potential by an amount equal to the dissociation energy [75]. For the plasma in PISCES-A, H_3^+ could also be important according to the previous experiments [18]. The roles of different channels of MAR during detachment are not included in this thesis.

Photon emission from a suitable line or set of lines allows one to 'monitor' the recombination according to Eq.(5.1), Eq.(5.2), Eq.(5.3) and Eq.(5.4). Fig.5.1 shows schematically the electron state density of neutrals formed by different processes. Generally, the populations of excited levels of atoms consist of both ionization and recombination components. The excited neutrals produced by electron impact or neutral atoms are usually in low n states [30] as shown in Fig.5.1. The MAR process also produces neutrals in low excited states (usually the principal number $n \leq 5$ [63]). However, three-body recombination creates neutrals with an electron in a high n state [75, 30] as shown in Fig.5.1. Theoretically, with an increase of the effective size of the electron orbital and a decrease of the binding energy, the probability that an electron will be captured by three-body collisions increases rapidly with principle quantum number, and the probability of spontaneous radiative transitions is reduced quickly [75]. This principal quantum number population distribution has been seen in JT-60U experiments [30]. There it is found that the populations of the $n < 4$ levels are dominated by the ionization component and the recombination component dominates those of $n > 6$ levels as shown in Fig.5.1. Considering the EIR for our experiments with low electron temperature at large radii, three-body recombination should be the dominant process since the radiative recombination is negligible due to the low temperature [71, 10, 70]. Therefore, the Helium neutrals formed from EIR are primarily generated in the high excited states. These high n electrons will then undergo radiative decay transitions to low n states. As a result, the intensities of high n emission lines of Helium neutrals are directly associated with the rate of three-body recombination, and then referred to as the EIR in the cold halo region. The absolute intensity of He neutral emission is obtained by calibration with an integrating sphere (Calibration Source Optics Head, model: 456-12-1) as described in Chapter 4. Since the number of recombinations per photon is weakly dependent on the electron temperature and density [70, 9, 12], the EIR rate can be estimated by the product of the number of recombinations per photon and the absolute intensity from spectroscopic data.

5.1.3 Estimation of EIR Sink

In order to estimate the EIR, the number of recombinations per photon is required, which is weakly dependent on the electron temperature and electron density [70, 9, 12]. Using an existing model [12], the number of recombinations per photon at $(7^3d - 2^3p)$ 370.5nm at different electron temperatures and electron densities can be calculated and

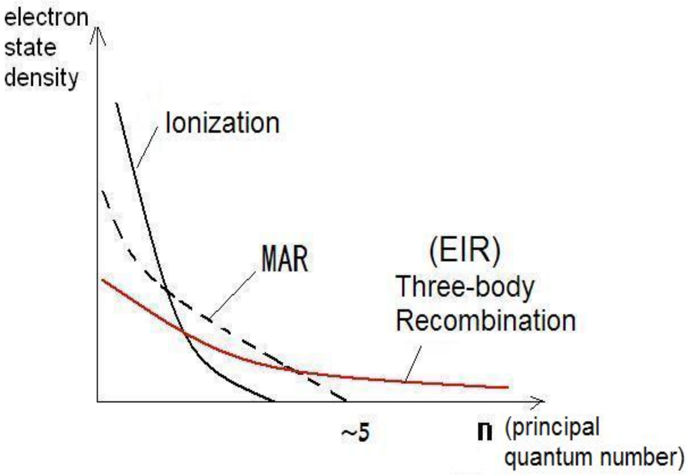

Figure 5.1: The electron energy state of neutrals formed during different processes

are shown in Fig. 5.2.

However, in the experiments, the emission at wavelength 353.1nm (11^3d-2^3p) is measured by the spectrometer to estimate the EIR since it is less possible to be influenced by excitations and MAR process than the emission at 370.5nm. Thus the number of recombinations per photon $N_{recomb/photon(353.1nm)}$ at (11^3d-2^3p) 353.1nm need to be derived from the calculated results in Fig.5.2. In order to accomplish this, the recombination rate α_λ is written as Eq.(5.5) and Eq.(5.6). The number of recombinations per photon at 353.1nm, $N_{recomb/photon(353.1nm)}$, can then be rewritten as Eq.(5.7).

$$\alpha_{370.5} = n_{(7^3d)}A_{(7^3d-2^3p)}N_{recomb/photon(370.5nm)} \tag{5.5}$$

$$\alpha_{353.1} = n_{(11^3d)}A_{(11^3d-2^3p)}N_{recomb/photon(353.1nm)} \tag{5.6}$$

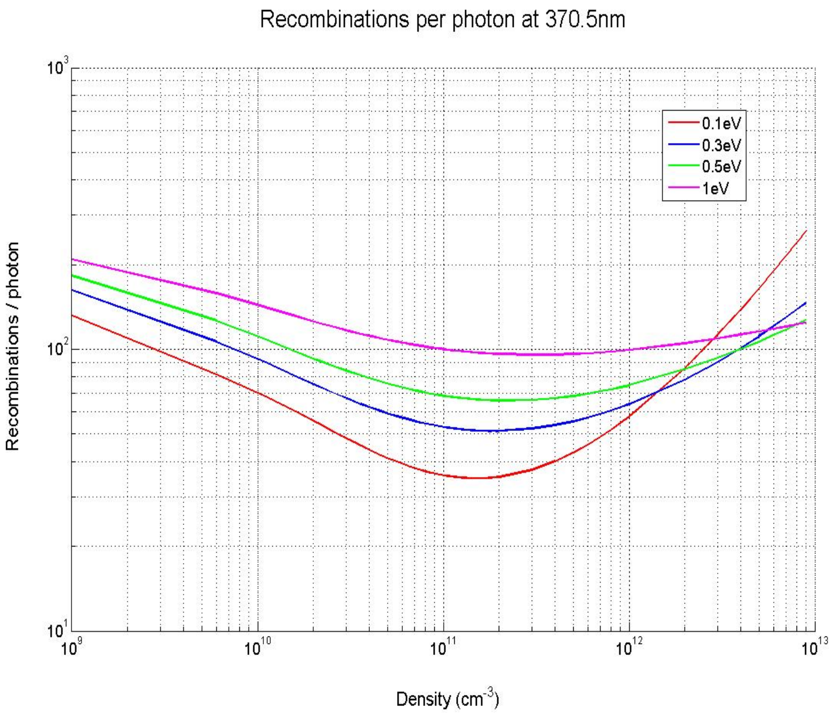

Figure 5.2: The number of ionizations and recombinations per photon dependent on the electron density and temperature for helium plasmas. Recombinations per photon from He neutral emission at $(7^3d - 2^3p)$ 370.5nm. The results are calculated by using a model in Ref.[12].

where n is the state population at its level, A is the Einstein coefficient of this transition, α_λ is the recombination rate for wavelength λ, and $N_{recomb/photon}$ is the number of recombination per photon of this transition. These then give

$$N_{recomb/photon(353.1nm)} = \frac{n_{(7^3d)} A_{(7^3d-2^3p)} N_{recomb/photon(370.5nm)}}{n_{(11^3d)} A_{(11^3d-2^3p)}} \tag{5.7}$$

where $N_{recomb/photon(370.5nm)}$ is calculated by the existing model [12] as shown in Fig.5.2.

According to the result in Chapter 4, the plasma in the halo region is in partial local thermodynamic equilibrium (PLTE). The state populations from the state level $n = 7$ to $n = 13$ then satisfy the Eq.(4.13), and thus Eq.(5.8).

$$\frac{n_{(7^3d)}}{n_{(11^3d)}} = \frac{g_{(7^3d)}}{g_{(11^3d)}} exp\left(\frac{\Delta E_{(7^3d)} - \Delta E_{(11^3d)}}{T_e}\right) \tag{5.8}$$

where ΔE is the ionization energy at its level, g is the statistical weight of the given level, and T_e is the electron temperature. All these coefficients are presented in Table 4.2.

Substituting Eq.(5.8) into Eq.(5.7), the number of recombinations per photon at 353.1nm, $N_{recomb/photon(353.1nm)}$, is obtained.

With the PISCES-A spectroscopy system, the high n emission from the $11^3d - 2^3p$ transition at 353.1nm is observed and measured. By calibrating the measured relative emission intensity with an integrating sphere as in Chapter 4, the absolute emission intensity in the halo region is obtained. Fig.5.3(a) presents the profiles of the absolute intensities of emissions at 353.1nm at the upstream port for the 0% 5.9%, 8.8% and 12% cases. Applying Abel inversion to the absolute chord-averaged intensity profiles, the radial profiles of the emissivity are obtained and shown in Fig.5.3(b). From this plot, it is seen that the EIR emissivity in the halo region is obvious. The error bars of emissivity in the core region are very big because of the accuumation effect during Abel inversion. In the core region, due to the relatively high electron temperature $(\sim 10eV)$, the EIR is negligible. As a result, the EIR is dominant in the halo region.

For the plasma condition at $n_e = 10^{17} m^{-3}$ and $T_e = 0.12eV$, the calculated $N_{recomb/photon(353.1nm)}$ is about 720. The EIR in the halo region can be estimated by the product of $N_{recomb/photon(353.1nm)}$ and the calibrated emissions at 353.1nm in Fig.5.3(a). With injecting H_2 gas, the emissivity changes from the red line to the black in Fig. 5.3. The results clearly show that the EIR is depressed rapidly as H_2 gas is added to the He plasma.

5.2 Ionization Source

5.2.1 Diagnostics

The ionization source is estimated by the spectral line of Helium neutral emission from the $3^1d - 2^1p$ transition at 667.8nm, which is measured by the spectrometer.

5.2.2 Theory

Since the electron temperature in the halo region is lower than 1eV, the ionization is negligible in the halo region. Therefore, it is safe to say that ionization occurs only in the core region, which can be identified by low n Helium neutral emission lines, such

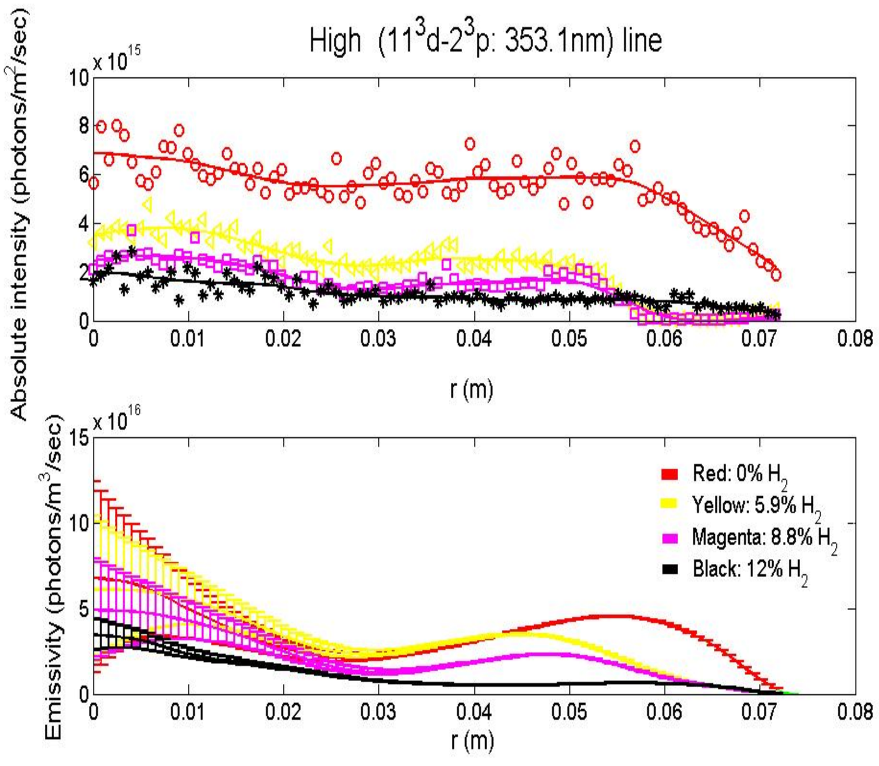

Figure 5.3: The radial profile of absolute intensity and emissivity of the high n $(11^d - 2^p)$ transition emission at the upstream port. The red lines are the 0% H_2 case; the yellow lines are for the 5.9% H_2 case; the magenta lines are for the 8.8% H_2 case; the black lines are the 12% H_2 case.

as the $3^1d - 2^1p$ transition emission line at $\lambda_0 = 667.8nm$. The measured spectroscopic data are calibrated by the calibration source, and the ionization is then estimated by the absolute intensity of emission at 667.8nm and the number of ionization per photon from the $3^1d - 2^1p$ transition, which is also weakly dependent on the electron temperature and electron density [9, 12].

5.2.3 Estimation of Ionization Source

Using the existing collisional-radiative model [12], the number of ionizations per photon at ($3^1d - 2^1p$) 667.8nm at different electron temperatures and electron densities can be calculated; the results are shown in Fig. 5.4. According to the electron temperature and density in the core region from the Langmuir probe data, the number of ionizations per photon at 667.8nm is in the range of $30 \sim 80$ in these experiments. Taking the radiation trapping into account [49], the calculated S/XB in Fig. 5.4 need to be modified by a factor 0.5 [49].

Fig.5.5(a) shows the profiles of absolute chord-averaged intensities of the 667.8nm emission line at the upstream port, which are obtained by calibrating the measured relative emission intensities as above. The lines in red, yellow, magenta and black are for the 0%, 5.9%, 8.8% and 12% H_2 case, respectively. Correspondingly, Fig.5.5(b) presents the radial profiles of the emissivity by applying Abel inversion to the absolute intensities of emissions for the different cases. The ionization rate is then estimated by the product of the number of ionizations per photon and the absolute intensity of emission at 667.8nm. The results of this analysis are shown in Fig.5.5. We conclude that the ionization in the

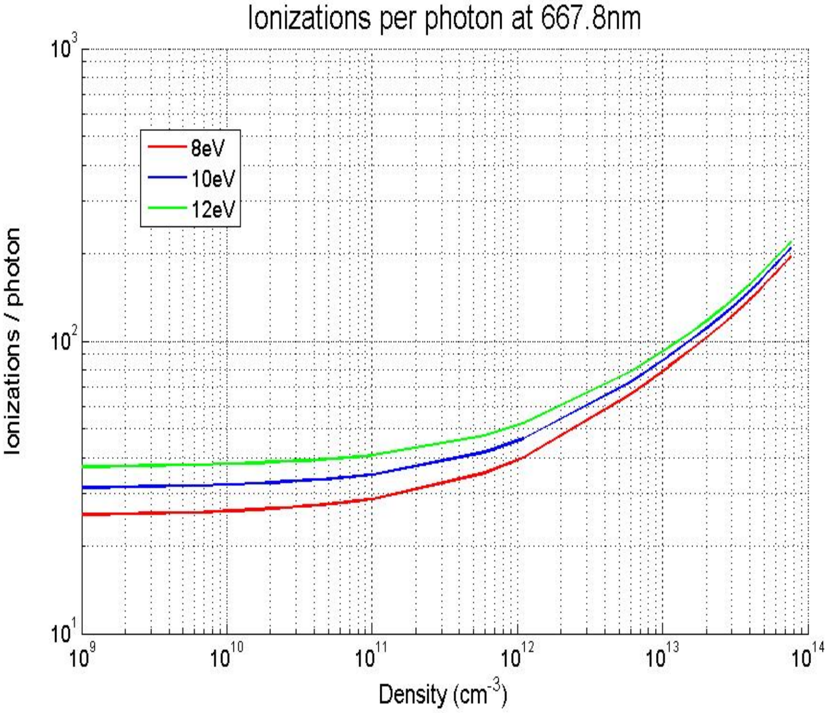

Figure 5.4: The number of ionizations per photon of He neutral emission at $(3^1d - 2^1p)$ 667.8nm dependent on the electron density and electron temperature.

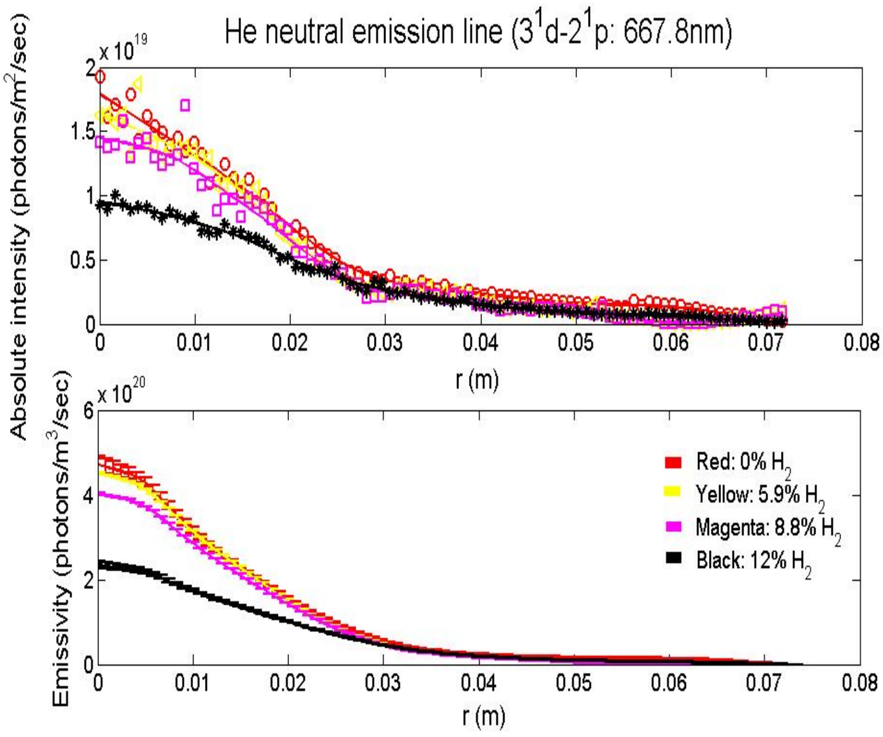

Figure 5.5: The radial profiles of the absolute intensity and emissivity of the $3^1d - 2^1p$ transition emission at the upstream port. The red lines are for the 0% H_2 case; the yellow lines are for the 5.9% H_2 case; the magenta lines are for the 8.8% H_2 case; the black lines are for the 12% H_2 case.

cold halo region is negligible small. When injecting H_2 gas into the target chamber, the ionization source in the central region is reduced due to the decrease of electron temperature and density according to the results in Chapter 4.

5.3 Qualitative Indications of MAR Using H Emission Line Ratios

5.3.1 Diagnostics

The H_α (3-2) emission line at 656.2nm and the H_γ (5-2) line at 434.0nm are measured by the spectrometer, and then the ratio of H_α to H_γ is computed to monitor MAR in the halo region.

5.3.2 Theory

The ratio of $\frac{H_\alpha}{H_\gamma}$, has been used to indicate the existence of EIR of Hydrogen plasma [41] as shown in Fig.5.6. As described above, EIR produces the neutrals mainly in high excited states. As a result, when EIR occurs, most of the neutrals formed by the recombination are in high excited states. Since the possibility of the electron in a high n state captured by the ion is larger than that of the electron in a lower state, the ratio of $\frac{H_\alpha}{H_\gamma}$ should decreases when EIR takes place, which is also presented in Fig.5.6 [Note these published results show the inverse ratio, $\frac{D_\gamma}{D_\alpha}$]. The sudden rise of the $\frac{D_\gamma}{D_\alpha}$ ratio indicates the onset of the electron-ion recombination.

As opposed to EIR, which generates He neutrals in highly excited states, MAR produces H neutrals in ground state or low excited states (usually $n \leq 5$ [63]). For the low

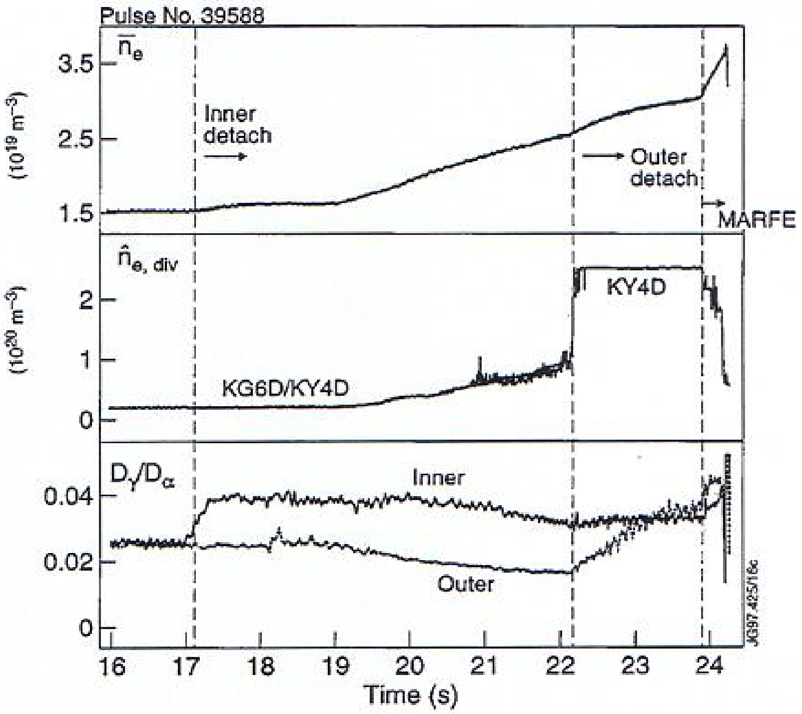

Figure 5.6: The data show the volume recombination in JET detached divertor plasmas. The sudden rise of the $\frac{D_\gamma}{D_\alpha}$ ratio indicates the onset of the electron-ion recombination. (From Ref.[41] by G.M. McCracken)

temperature $(T_e \sim 0.1 - 0.2eV)$ in the halo region, the H neutrals due to MAR are mainly created at states with $n = 2$ and $n = 3$ [63]. As a result, the ratio of $\frac{H_\alpha}{H_\gamma}$ increases when the MAR occurs, in contrast to the drop in $\frac{H_\alpha}{H_\gamma}$ that occurs with EIR. The occurrence of MAR in the halo region can then be qualitatively inferred by the ratio of $\frac{H_\alpha}{H_\gamma}$ since ionization and excitation, which also generate low excited state neutrals, are very weak in the cold halo region. This ratio can be obtained by measuring the intensities of H neutral emissions at 656.2nm and 434.0nm with the PISCES-A spectroscopy system.

5.3.3 Qualitatively Measurements of MAR with $\frac{H_\alpha}{H_\gamma}$ Ratio

Fig.5.7 shows the ratio of $\frac{H_\alpha}{H_\gamma}$ for the 2.9% H_2 case, which is plotted in blue. As discussed above, if the EIR process exists at large radii, the $\frac{H_\alpha}{H_\gamma}$ ratio should go down along the dashed red line in the transition zone from ionizing in the core to EIR in the halo. However, by injecting small amount of H_2 gas, a large $\frac{H_\alpha}{H_\gamma}$ ratio is seen for $r \geq 5cm$, as shown by the blue curve in Fig.5.7. The ratio increases rapidly at large radii instead of a drop from the center to the edge. The radial profiles of the $\frac{H_\alpha}{H_\gamma}$ ratio for all different cases will be presented in Chapter 6 to show the evolution of MAR with the increase of the H_2 content.

ACKNOWLEDGEMENT

Chapter 5, in part, has been submitted for publication of the materials as it may appear in Physics of Plasmas, 2008, Laizhong Cai, George Tynan, Eirc Hollmann. The dissertation author was the primary investigator and author of this paper.

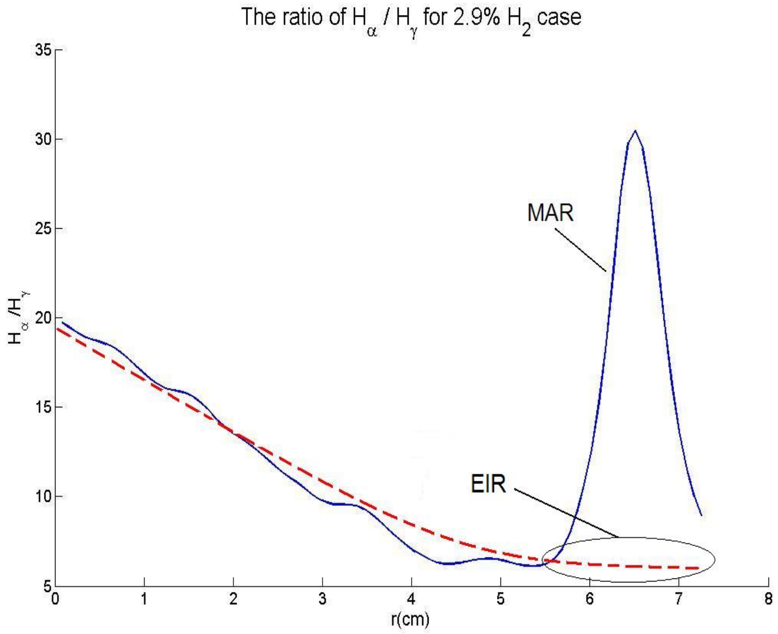

Figure 5.7: The radial profile of the ratio of $\frac{H\alpha}{H\gamma}$ for the 2.9% H_2 case. The blue curve is obtained from spectroscopic data; the red dashed line shows a possible trend of $\frac{H\alpha}{H\gamma}$ ratio from an ionization zone to a standard EIR zone.

6

Results and Discussion

By injecting H_2 gas into the helium plasma in the target chamber, the MAR process can be studied in detail. The gas pressure in the target region varies from 7.3mTorr (pure helium gas) to a maximum of 8.3mTorr (a mixture of 88% He and 12% H_2). By controlling the H_2 gas injecting flow rate, the fraction of pressure due to H_2 can vary from 0% to 12%. The cases investigated during experiments are with the fraction of 0%, 1.2%, 2.9%, 5.9%, 8.8% and 12%. In the core region of the plasma, electron density n_e is a few $10^{12} cm^{-3}$ and electron temperature T_e is about $10 eV$; in the halo region, n_e is $\sim 10^{11} cm^{-3}$ and T_e is $\sim 0.1 eV$. Due to such an electron temperature profile, ionization is significant in the core region, while recombination is dominant in the cold halo region.

6.1 EIR Depression

As described in Chapter 5, the high n emission lines due to transitions of excited helium neutrals are the "monitor" of electron-ion recombination, which correspond to

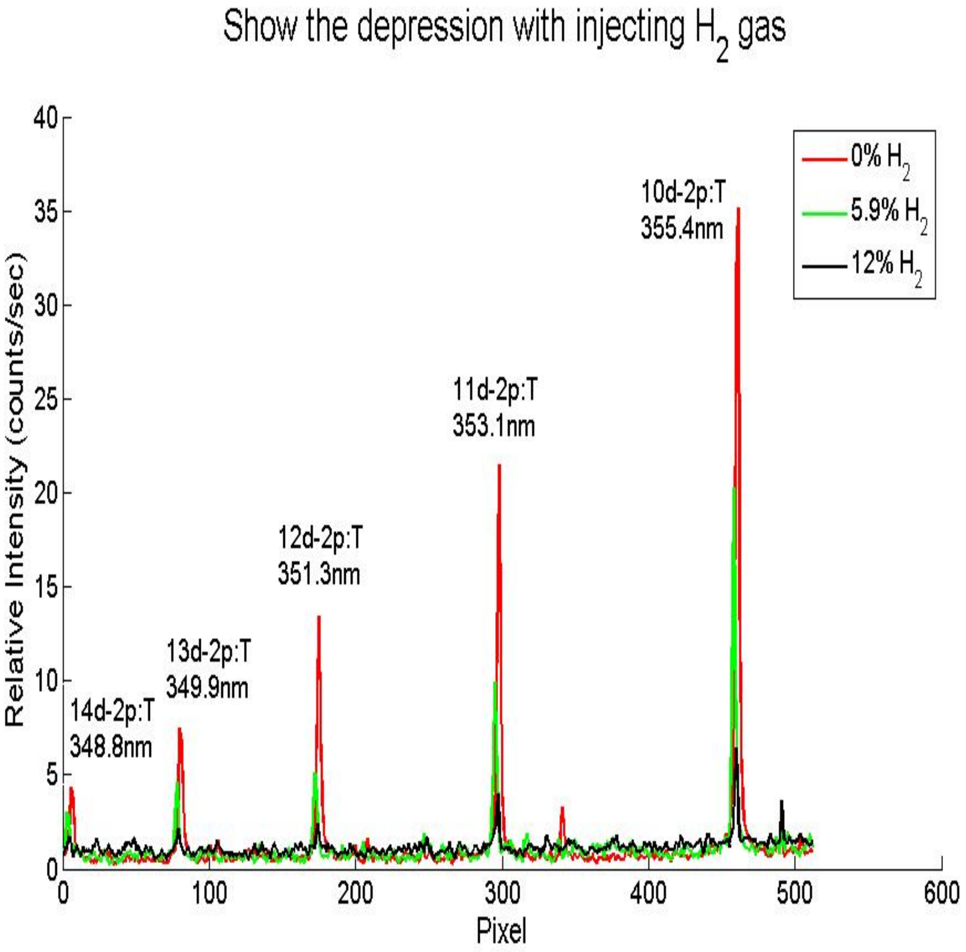

Figure 6.1: Show the depression of the high n emissions ($10^3d - 2^3p \sim 14^3d - 2^3p$) from He neutrals while injecting H_2 gas. The red line is for pure He plasma; the green line is for the 5.9% H_2 case; and the black shows the case of 12% H_2 gas.

three-body recombination, and then are referred to as EIR events. With the PISCES-A spectroscopy, the high n emission lines from $10^3d - 2^3p$ to $14^3d - 2^3p$ transitions are observed and shown in Fig.6.1. The red line is taken at the upstream port for the pure helium plasma, i.e., the 0% H_2 case; the green line is for the 5.9% H_2 case; and the black shows the case of 12% H_2 gas. It is obvious that the emission is depressed when H_2 gas is added. When the H_2 gas partial pressure is above a threshold value, about 12% H_2 in this experiment, no significant EIR appears at all. That is, EIR is totally quenched with a sufficient H_2 content. Similar results are obtained at the downstream location as well.

Without H_2 gas injection, the distinct high n emission in the halo region confirms that the EIR occurs there. After injecting small amount of H_2 gas, the EIR is depressed and even collapses. As a result, the measured ion loss discussed below must be due to another recombination process. Because the new process occurs with injecting of H_2, it seems likely to be due to H_2 mediated He recombination (i.e., MAR). By doing the particle balance analysis as Eq.(3.1) and Eq.(3.2), the rate of the MAR in the detaching plasma can be quantified.

6.2 Particle Balance Analysis

As presented in Chapter 4 and Chapter 5, measurements were taken at both the upstream port and the downstream port. The electron density, electron temperature, axial flow velocity, radial flux to the chamber wall, ionization source and EIR sink were obtained. As described in Chapter 3 and shown in Fig.3.5, the particle balance analysis of He^+ is performed in the core region (control volume 1) and halo region (control volume2), respectively.

With the combination of the radial profiles of electron density and parallel flow velocity (the Hydrogen ion flow has the similar flow velocity as helium ion flow since the momentum exchange time due to ion-ion collisions is $\sim 10^{-6} sec$, much smaller than the time scale of parallel flow $\sim 10^{-4} sec$), the axial ion flux at different axial positions can then be calculated by

$$\Gamma_{||}(r) = n_e(r) \cdot v_{||}(r) \tag{6.1}$$

where $n_e(r)$ is the radial profile of electron density; and $v_{||}(r)$ is the radial profile of axial flow velocity. The net change in axial flux is obtained by the difference between the axial fluxes at the upstream and downstream ports, which are derived by integrating Eq.(6.1) over the cross sections of the control volume 1 (core plasma), respectively. The radial fluxes to the wall are measured at several discrete axial locations as described in section 4.2. The total radial flux to the wall is obtained by integrating the profile of the radial flux shown in Fig.4.11 over the chamber wall shown as control volume 2 in Fig.2.2. Integrating the measured emissivity of EIR over the whole control volume 2, the total EIR sink is estimated. Similarly, the ionization rate is estimated by integrating over the core region, the control volume 1.

The results of this analysis are presented in Fig.6.2. The blue open circles show the net axial flux in the control volume 1; the blue stars are the total ionization source.

Doubly ionized helium He^{2+} is neglected in this analysis; this is justified by the measured intensity ratio HeI(6678)/HeII(4685)$\sim 0.8 \times 10^3 - 1.5 \times 10^3$. Together with the expected photon efficiencies $S/XB(6678) \sim 50-60$ and $S/XB(4685) \sim 5-8$ for the core plasma conditions of these experiments [66] and assuming comparable He^+ and He^{2+} loss rates, we arrive at a negligible He^{2+} fraction $\frac{n_{He^{2+}}}{n_{He^+}} < 2 \times 10^{-4}$.

The hydrogen ions are insignificant when the H_2 content is low. When the H_2 gas is injected into the target region, the ions are a mixture of He^+ and hydrogen ions. Hydrogen ions can, however, be present in significant quantities in these experiments. When the H_2 gas is injected into the target region, the ions are the mixture of He^+ and hydrogen ions. The ratios of $\frac{n_{He^+}}{n_e}$ on PISCES for different plasma conditions were obtained in [49]. According to the results of in Ref. [49], this ratio decreases from 100% to $\sim$ 50% when the H_2 content changes from 0% to 12%. As a result, the He^+ particle conservation equations (3.3) and (3.4) should be modified as shown in Eq. (6.2) and Eq. (6.3), since the probe data do not discriminate the type of ions. The He^+ fraction f in the particle conservation equations (6.2) and (6.3) is the ratio of $\frac{n_{He^+}}{n_e}$, which changes from 100% to $\sim$ 50% when the ratio of H_2 partial gas pressure increases from 0% to 12%.

In the core region (control volume 1), the particle conservation equation for He^+ ions is

$$f \cdot \int (\Gamma_{\|1} - \Gamma_{\|2}) dA_z + \int S_{ion} dV_1 = \int \Gamma_r dA_r \tag{6.2}$$

In the halo region (control volume2), the corresponding equation is

$$\int \Gamma_r dA_r = f \cdot \int \Gamma_{wall} dA_{wall} + \int (S_{EIR} + S_{MAR}) dV_2 \tag{6.3}$$

where f is the ratio of $\frac{n_{He^+}}{n_e}$, which is 100%, 92.7%, 80.6%, 66.8%, 56.4% and 48.5% for the different plasma conditions where measurements are taken from Ref.[49]; where S_{MAR} is the MAR recombination sink; $\Gamma_{\|1}$ and $\Gamma_{\|2}$ are parallel particle fluxes at axial location 1 (the upstream port) and 2 (the downstream port); Γ_r is the radial flux on the boundary of the control volume 1; Γ_{wall} is the radial flux to the wall; S_{ion} is the ionization source; S_{EIR} is the electron-ion recombination sink; V_1 and V_2 are the whole volumes of control volume 1 and 2, respectively; A_{wall} is the wall area of the control volume 2, that is, πDl (D is the diameter of the chamber, l is the length of the control volume 2); $dA_z = 2\pi r dr$ ($0 \leq r \leq a$ and a is the radius of the control volume 1); and $A_r = 2\pi al$.

With the combination of electron density and the axial flow velocity, the total axial flux increases when H_2 gas is added. According to the particle conservation equation in the core region as Eq.(6.2), the total number of He^+ ions coming out of the core region and entering the halo region is obtained by summing the net axial flux source and ionization source in the core region. The result is the red dotted curve in Fig.6.2(a) and (b). The green curve with square data points in Fig.6.2(b) shows the EIR sink in the cold halo region estimated by the spectroscopic data. The radial flux to the chamber wall is plotted in green open circles. With the assumption of small axial ion flow in the halo region, consistent with the results shown in Fig.4.15 and Fig.4.16, the volume averaged MAR rate can then be derived with radial flux to the chamber wall and the EIR sink in the halo region by Eq.(6.3). The calculated result of MAR is presented in magenta in Fig.6.2(b). By adjusting the percentage of H_2 gas pressure in the total target gas pressure, the MAR is quantified from the case of no MAR (0% H_2 case) to the case of no significant EIR at all (12% H_2 case) as shown in Fig.6.2.

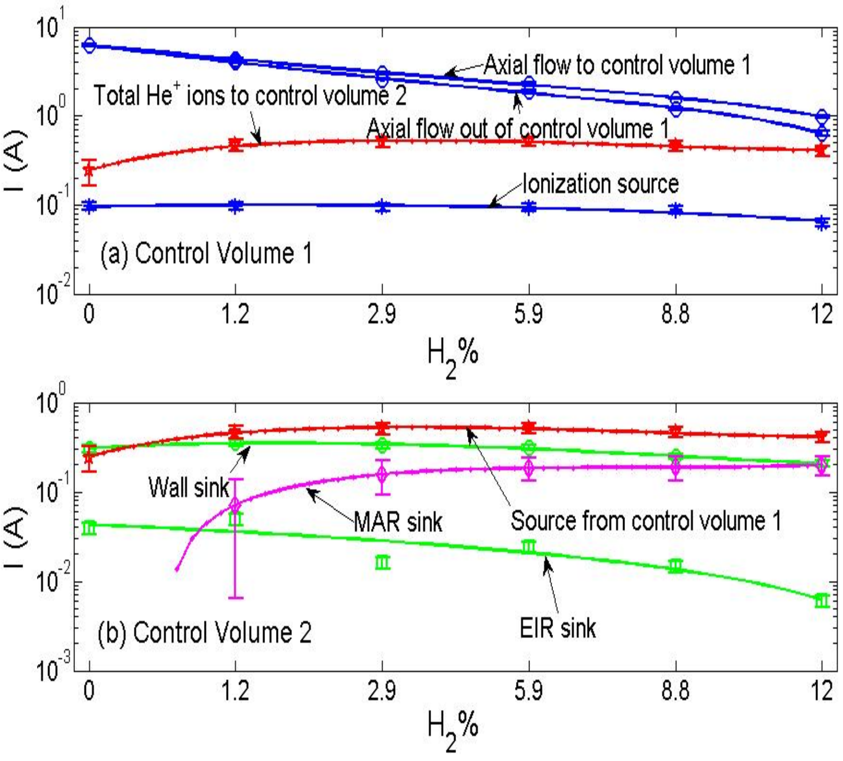

Figure 6.2: The particle balance of He^{+} ions. (a) the particle balance in control volume 1; (b) the particle balance in control volume 2. Axial flow source, ionization source, wall sink and EIR sink are obtained from the measured data; the total source is the sum of axial flow source and ionization source; the MAR is calculated by the particle balance analysis.

From Fig.6.2, the net accumulation of particles in control volume 1 increases when H_2 gas is added, which is caused by the decrease of axial flow velocity at the downstream port due to the injecting H_2 gas. The ionization source in the core region also decreases with H_2 injection since the electron density and temperature decrease in control volume 1 with H_2 injection. The total radial flux to the wall does not change very much for all cases, but the EIR is reduced by a factor of 10 times with 12% H_2 gas, which is also indicated by the intensities of the He neutral emission lines in Fig.6.1. By careful partical balance analysis, there is a missing ion loss term, which is inferred to as the MAR sink. The missing loss term is larger than the accumulated errors from the various source and sink terms, and thus represents a real, new volumetric ion loss mechanism. The inferred volume-integrated MAR loss term obtained by the particle conservation varies from around zero for pure helium plasma to $\sim 0.19A$ for the 12% H_2 gas case. When a small amount H_2 gas is injected into pure He plasma, EIR is depressed rapidly; simultaneously MAR begins to occur and increases with the H_2 gas partial pressure, that is, MAR and EIR coexist. After the partial pressure fraction of H_2 gas is above ~3%, MAR becomes the dominant volumetric recombination process.

Overall, the magnitude of MAR is one order larger than that of EIR in our experiments with 2%~12% H_2 gas. In the case of 12% H_2 gas, the MAR loss rate is almost 30 times bigger than EIR.

This analysis neglects molecular-assisted dissociation (MAD), which includes two channels: $HeH^+ + e \rightarrow He + H^+ + e$ and $HeH^+ + e \rightarrow H + He^+ + e$. The rate coefficients of MAD in a He/H plasma are not available. Using the measured results and the rate coefficient of MAD obtained from a pure hydrogen plasma [8], the total estimated MAD in the core region is $\sim 0.006A - 0.08A$ with H_2 injection. The effect of MAD modifies the value to MAR, but the basic conclusions drawn here are still valid.

6.3 Discussion of EIR Measurements

According to the semi-empirical formula of three-body recombination, which is shown as Eq.(6.4) [75], the EIR rate coefficient can be estimated by the measured electron temperature and electron density in the cold halo region.

$$\alpha_3 = 8.75 \times 10^{-27} T_e^{-4.5} \quad cm^6/sec \tag{6.4}$$

where T_e is electron temperature in eV; and α_3 is recombination rate coefficient.

The recombination sink in the halo region can then be written in Eq.(6.5).

$$S_{EIR} = \alpha_3 \cdot n_e^3 \cdot V \tag{6.5}$$

where S_{EIR} is the total EIR sink in the halo region; V is the volume of the halo region (control volume 2). So

$$V = \pi(10^2 - 3^2) \times 22 = 6.2 \times 10^3 cm^3 = 0.0062 m^3$$

Taking the results of $n_e \sim 5 \times 10^{17} m^{-3}$ and $T_e = 0.1eV$ obtained in Chapter 4 into the equations above, the recombination sink S_{EIR} in the halo region can be estimated roughly as following:

$$S_{EIR} = \alpha_3 \cdot n_e^3 \cdot V = \alpha_3 \cdot (2 \times 10^{17})^3 \cdot 0.062 = 0.03A$$

According the measured results in Fig.6.2, EIR sink in the halo region for the pure helium case is around 0.04A. The difference between the experimental result and value estimated by the formula of EIR [75] is around ~30%. Considering the error of measured temperature and density in the halo region and the inaccurateness of the formula, the difference is acceptable due to the sensitivity of the electron temperature and electron density in the semi-empirical formula.

6.4 Discussion of MAR Measurements

The rate coefficient of MAR K_{MAR} can be estimated by Eq.6.6.

$$S_{MAR} = K_{MAR} \cdot n_e \cdot n_{H_2} \cdot V \tag{6.6}$$

where S_{MAR} is the total MAR sink in the halo region; n_e is the electron density in the halo region; n_{H_2} is hydrogen gas density; K_{MAR} is the rate coefficient of MAR; and V is the volume of the halo region.

For the 12% H_2 case, the hydrogen gas pressure P_{H_2} is 1mTorr, so

$$n_{H_2} = \frac{P(Torr)}{1.2 \times 10^{-21} \cdot T} = \frac{0.001}{10^{-21} \times 0.1} = 8 \times 10^{18} m^{-3}.$$

where $T_{H_2} = 0.1eV$ is taken from Ref.[49].

Using the results of $S_{MAR} \sim 0.19A$ and $n_e \approx 5 \times 10^{17} m^{-3}$ in the halo region, we can estimate

$$K_{MAR} = \frac{S_{MAR}}{n_e \cdot n_{H_2} \cdot V} = \frac{0.19}{1.6 \times 10^{-19} \times 5 \times 10^{17} \times 8 \times 10^{18} \times 0.0062} = 4 \times 10^{-17} m^3/sec$$

This rate coefficient can be compared with previously published estimates for MAR [47] as shown in Fig. 6.3.

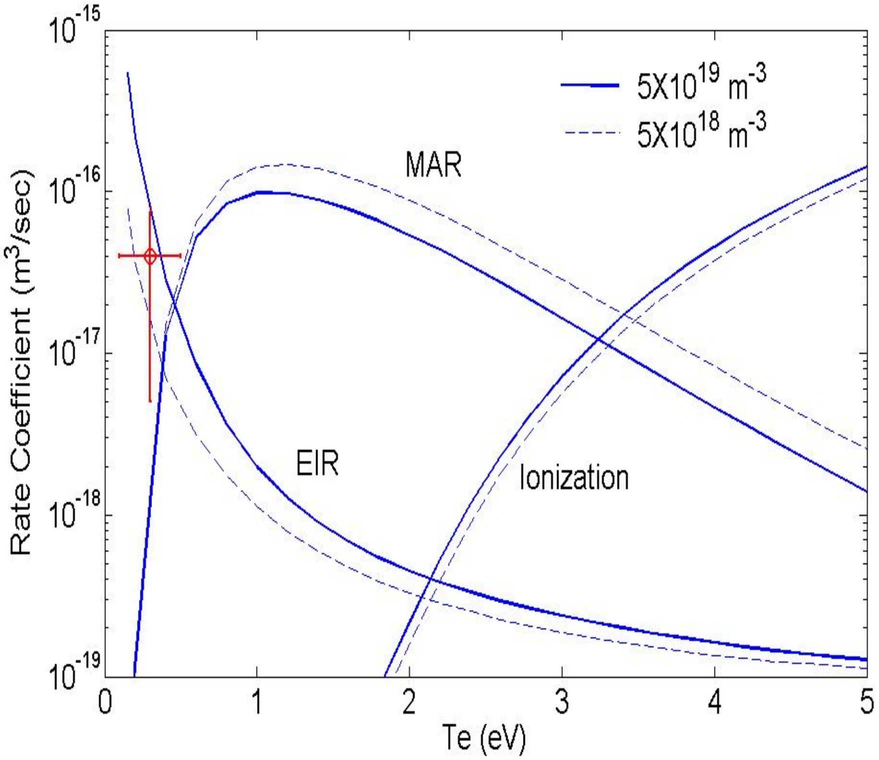

Figure 6.3: The simulation results of the rate coefficients of EIR (K_{EIR}) and MAR (K_{EIR}) as a function of electron density and temperature in He/H mixture plasma in Ref. [47]. The red data point is the MAR rate coefficient quantified by the measured MAR in this experiment, which is obtained at $n_e \sim 10^{17} m^{-3}$ and $T_e \sim 0.1 - 0.5 eV$.

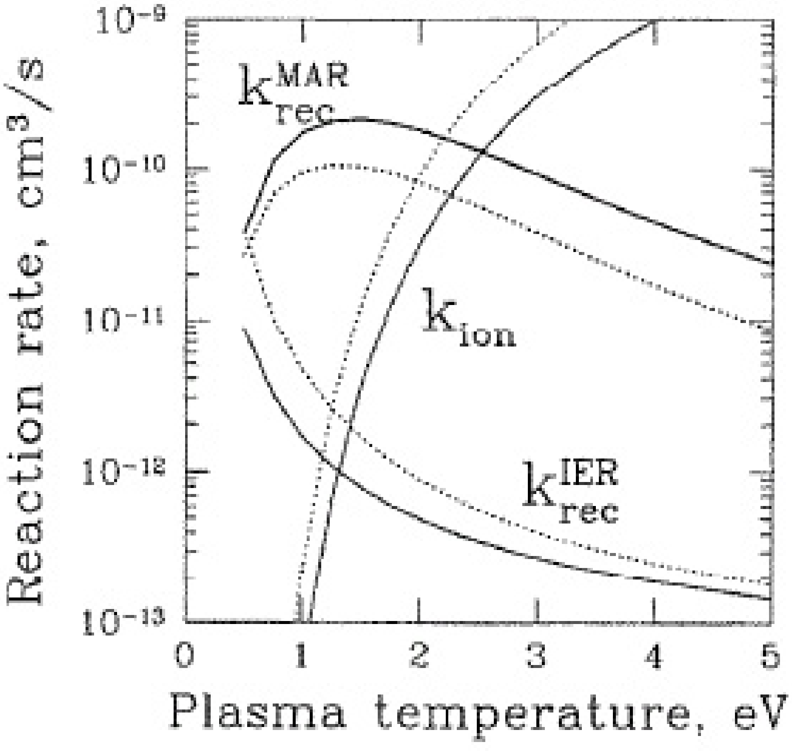

Figure 6.4: The electron temperature dependence of the rate coefficients of EIR (k_{rec}^{EIR}) and MAR (k_{rec}^{MAR}) for a pure H_2 discharge as a function of electron density. Effective rate coefficients are given for a plasma density of $n_e = 10^{14} cm^{-3}$ by the solid curves and for $n_e = 10^{15} cm^{-3}$ by the broken curves. (From Ref.[56])

The rate coefficient of MAR has been investigated by simulations [56, 47]. However, it is hard to find the simulation result for $T_e \sim 0.1eV$. Fig.6.4 shows the calculated rate coefficients of relevant processes in pure Hydrogen plasma for various values of electron density and electron temperature [56], which were obtained when $\frac{n_{H_2}}{n_e} = 0.1$. According to the investigations by K. Miyamoto, it is claimed that the ratio of $\frac{n_{H_2}}{n_e}$ is another significant factor to contribute to MAR, especially, for $T_e < 1eV$ [43].

These published results show that the electron temperature T_e, electron density n_e and the $\frac{n_{H_2}}{n_e}$ ratio are important parameters to influence the MAR rate. Additionally, the EIR rate decreases exponentially due to the n_e^3 term in Eq.(6.5) when the electron density n_e decreases, while MAR rate increases with the decrease of n_e as shown in Fig.6.4. As a result, it seems reasonable that the MAR rate is much larger than the EIR rate when the electron density is low, which is the condition in PISCES-A.

Another possible impact to be considered is H_3^+ ions in PISCES-A. Plasma recombination through the molecules HeH^+ and H^- as Eq.(5.3) and Eq.(5.4) have been considered as possibly contributing to detachment. Previous estimates found that H_3^+ recombination as in Eq.(6.7) could be very important in PISCES-A experiments [18], which is performed at $\frac{n_{H_2}}{n_e} = 0.2 \sim 5$.

$$H_3^+ + He \rightarrow HeH^+ + H_2 \qquad and\ then\ followed\ by \qquad HeH^+ + e \rightarrow He + H^* \quad (6.7)$$

As a result, due to the larger ratio of $\frac{n_{H_2}}{n_e} \sim 4-40$ in our experiments, it is reasonable to predict that the H_3^+ is important here too. However, we also note that this mechanism leads to the destruction of molecular H ions, but does not affect the He ion particle balance. As a result, it will not affect the conclusions of our study, which focused on the He ion particle balance.

The characteristic recombination time is the reciprocal of the recombination rate. Therefore, the life time of MAR in the 12% H_2 case is estimated as

$$\tau_{MAR} = \frac{n_e}{S_{MAR}/V} = \frac{2 \times 10^{17}}{\dfrac{0.19}{1.6 \times 10^{-19} \times 0.0062}} \approx 1 \times 10^{-3} s.$$

The characteristic time of the parallel flow is

$$\tau_{||} \sim \frac{L}{v_{||}} = \frac{0.5}{1.5 \times 10^3} \approx 3 \times 10^{-4} s$$

where L is the axial scale length of the plasma, and $v_{||}$ is the parallel flow velocity.

Comparing the characteristic time of the parallel flow with the life time of MAR, it indicates that MAR is an important loss term in these experiments.

6.5 Radial Profile of the $\frac{H_\alpha}{H_\gamma}$ ratio

As described in Chapter 5, the ratio of $\frac{H_\alpha}{H_\gamma}$ can be used to indicate MAR qualitatively since MAR produces neutrals in a low excited or ground states, especially, excited state $n = 2$ or $n = 3$ for a low electron temperature plasma $(0.1 \sim 0.2eV)$ [63] in PISCES-A. Applying Abel inversion to the measured chord-integrated intensities of hydrogen neutral emission lines at 656.2nm and 434.0nm, the radial profiles of H_α and H_γ are obtained from the spectroscopic data. The result is shown in Fig.6.5.

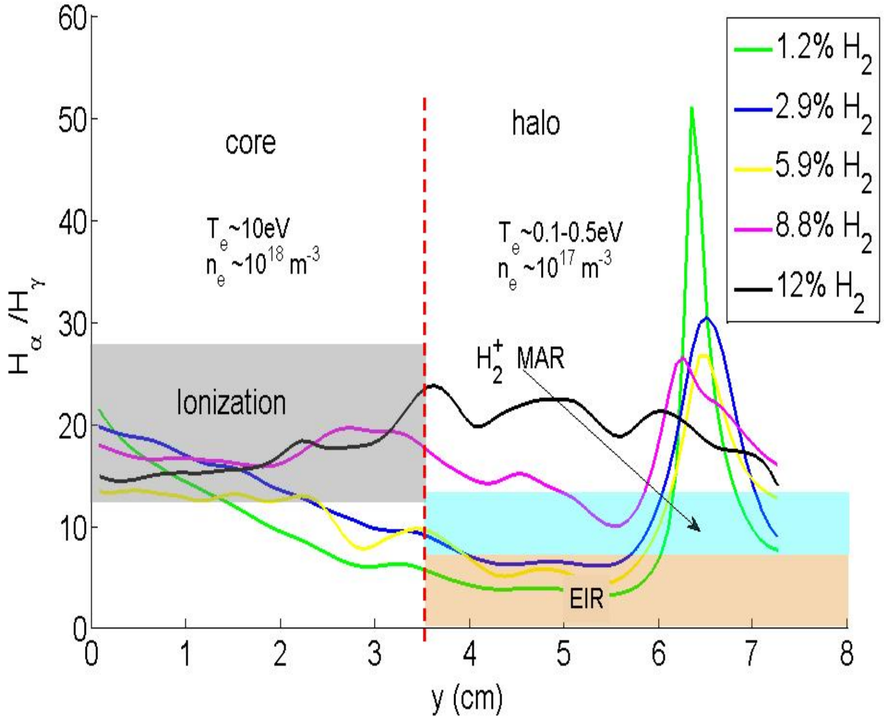

Figure 6.5: The vertical profiles of $\frac{H_\alpha}{H_\gamma}$ for different cases. The ranges of $\frac{H_\alpha}{H_\gamma}$ for different physical processes are filled in different colors. The estimated range of $\frac{H_\alpha}{H_\gamma}$ for ionization is from Ref. [41]; those of EIR and H_2^+ MAR are from Ref. [23]. $r = 0$ is the center of the core plasma; $r \geq 3.5cm$ is considered as the halo region.

The ratio of $\frac{H_\alpha}{H_\gamma}$, is expected to decrease radially as the plasma transitions from ionizing in the core to EIR recombination in the edge. However, with H_2 injection in PISCES-A, the ratio increases rapidly (up to $\frac{H_\alpha}{H_\gamma} \sim 50$) at large radii, as shown in Fig.6.5. However, $\frac{H_\alpha}{H_\gamma} \sim 1-5$ is expected for EIR and $\frac{H_\alpha}{H_\gamma} \sim 8-13$ is expected for traditional hydrogen MAR (H_2^+ recombination) [23]. These anomalous $\frac{H_\alpha}{H_\gamma}$ ratios are not understood at present, but could be due to H_3^+ recombination, since H_3^+ is known to be the dominant hydrogenic ion in these plasmas [18].

When injecting additional H_2 gas into the target region, the ratios at large radii is decreased; at the same time, the increase in $\frac{H_\alpha}{H_\gamma}$ expands from the edge toward the center as the H_2 partial pressure is increased. This result suggests that the MAR occurs in the region close to the chamber wall at the beginning. As additional H_2 gas is introduced into the chamber, the zone where MAR happens moves from the edge to the core plasma. The evolution of MAR implied by the radial profiles of the $\frac{H_\alpha}{H_\gamma}$ ratio is consistent with the effect of $\frac{n_{H_2}}{n_e}$ on MAR given in the discussion above. Another piece of evidence in support of this explanation is the behavior of the radial flux to the wall shown in Fig.4.11. From Fig.4.11, we see that as the H_2 content is increased, the radial flux increases and reaches a peak at 5.9% H_2. It then decreases as the H_2 fraction increases further. This could be caused by MAR. As shown in Fig.6.5, for the two cases of 8.8% and 12% H_2, MAR happens mainly around the core region. As a result, fewer ions can go further and reach the chamber wall due to the MAR ion loss and thus the radial fluxes to the chamber wall for those two cases should decrease with additional injected H_2 gas.

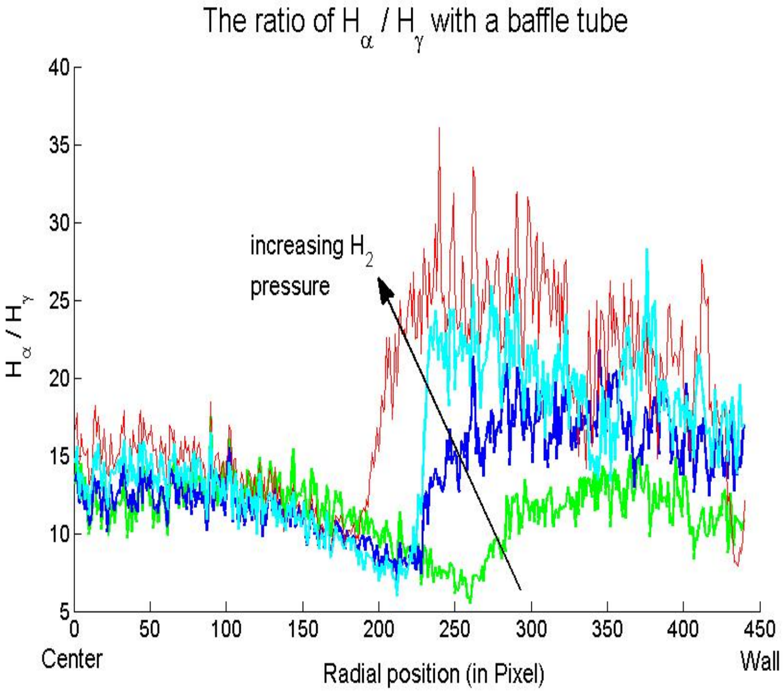

Figure 6.6: The ratio of $\frac{H_\alpha}{H_\gamma}$ for different experiments with a baffle tube on PISCES-A. The horizontal axis is proportional to radial location. The left side of the horizontal axis is the center of the core plasma. When injecting H_2 gas into the target region, the ratio varies in the order of green, blue, yellow and red with the increasing of H_2 gas partial pressure.

Fig.6.6 shows the ratio of $\frac{H_\alpha}{H_\gamma}$ for similar experiments with a baffle tube on PISCES-A, consistent with previous experiments [15]. The baffle tube in a 5cm diameter is 30 cm long and mounted on the neck-like flange between the source region and the target region. With the baffle tube, the cross-field confinement is better; and as a result, the electron density in the halo region should be lower than that without the baffle tube. That is why MAR could occur in the region close to the core plasma, which is different from the case of small H_2 density as shown in Fig.6.5. It is consistent with the explanation on expansion of MAR described above.

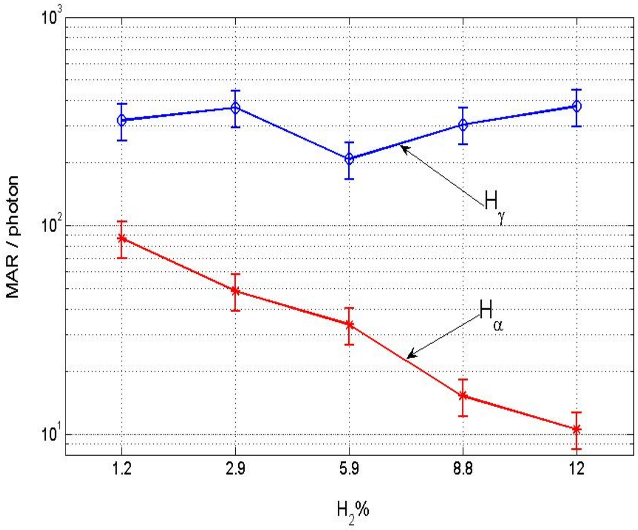

Figure 6.7: The total MAR per photon from H_α and H_γ transitions. The blue line is for the H_γ photon; the red line is for the H_α photon.

According to the number of H_γ photons and the total MAR sink in the halo region, the number of MAR per H_γ photon is estimated roughly to be $200 \sim 400$ as the blue line presented in Fig.6.7. It varies with the injection of H_2 gas, which could result from the change of plasma condition in the halo region due to the MAR and injection. Similarly, the number of MAR per H_α photon is calculated and shown in Fig.6.7. It is in the range of $10 \sim 90$.

6.6 Discussion of Radial Flux to the Chamber Wall

From Fig.6.2 above, the radial flux to the chamber wall does not vary much with the H_2 gas injection. However, it is very important for the ion loss in the halo region.

The characteristic time of radial transport can be estimated as Eq.(6.8).

$$\tau_\perp \sim \frac{n_e}{\frac{\Gamma/A}{R}} = \frac{2\times 10^{17}}{\frac{0.22}{1.6\times 10^{-19}\pi \times 0.2\times 0.22\times 0.07}} \approx 1\times 10^{-3}s \tag{6.8}$$

Comparing the characteristic time of radial transport with the lifetime of MAR computed above, we conclude that the radial loss is comparable to the MAR sink in the the case with 12% H_2 gas, while it is the dominant loss term in other cases. This result is consistent with previous experimental results in H_2 plasmas [17].

ACKNOWLEDGEMENT

Chapter 6, in part, has been submitted for publication of the materials as it may appear in Physics of Plasmas, 2008, Laizhong Cai, George Tynan, Eirc Hollmann. The dissertation author was the primary investigator and author of this paper.

7

Summary

7.1 Summary

These experiments were motivated by the desire to better understanding molecular-activated recombination (MAR), associated with vibrationally excited molecules, in a divertor region. In order to demonstrate the effect of MAR during detachment, hydrogen gas is injected into helium plasma discharge. The study was carried out on PISCES-A at University of California at San Diego, a linear device to simulate a gas-target divertor for magnetic fusion tokamaks. The plasma is generated by a discharge voltage between a disc-shaped cathode (LaB_6) and a concentric copper anode tube. And then the plasma transports to the floating target plate along the magnetic field ($\sim 960 Gauss$) and is sustained in a steady state in PISCES-A. By injecting neutral gas into the target chamber, the conditions similar to those found in the divertor region of tokamak devices are produced.

A partially detached Helium plasma is created when the neutral gas pressure in the target region is high enough. A hot core plasma column $(\sim 10eV)$ is surrounded by a cold $(< 0.1eV)$ halo plasma. During the experiments, the target gas pressure varied from 7.3mTorr of pure He neutral gas to 8.3mTorr of 88% He and 12% H_2 gas, while the source gas pressure was kept at 6.3mTorr. As a result, the ratio of partial H_2 gas pressure to the total neutral pressure in the target chamber was in the range fo $0 \sim 12\%$. Measurements were taken at the percentage 0%, 1.2%, 2.9%, 5.9%, 8.8% and 12% H_2 gas.

Two scanning Langmuir probes at two different axial positions were used to measure the radial profiles of electron density and temperature. Helium ion emission Doppler shifts at 468.6nm were used to measure the axial ion flow velocity, and these measurements were then combined to estimate the axial particle flux. A set of wall probes were mounted on the wall of each side port to obtain the radial flux to the chamber wall. The ionization source was estimated by absolute intensity of Helium neutral emission from $3^1d - 2^1p$ transitions by an absolutely calibrated 1.3m Czerny-Turner spectrometer. Similarly, the sink of electron-ion recombination, EIR, which was identified by the high n (principal quantum number) emissions, was obtained by the absolute intensity of Helium neutral emission from $11^3d - 2^3p$ transition since the number of recombination per photon is weakly dependent on the electron density and electron temperature. The low electron temperature at large radii of the vacuum chamber was also estimated by the series of emissions from excited Helium neutrals.

Using the results from measurements above, a particle balance analysis was performed in the core region and cold halo region, respectively. According to the particle conservation equation in the core column, the ions coming into the halo region from the core region was derived. With the assumption of no significant axial flow in the halo region, which is valid for these experiments, it is found that a missing ion sink exists in this region by the particle balance with measured radial flux to the wall and EIR sink, which is inferred to be a MAR process. With the injection of H_2 gas, MAR is presented quantitatively against the partial H_2 gas pressure ranging from 0% to 12%. When injecting H_2 gas into the target chamber, EIR is depressed by a factor of 10. The result of the measured EIR sink is consistent with the theoretical estimates evaluated with the measured electron density and temperature. MAR increases when more H_2 gas is added, and becomes larger (up to 30 times) than EIR sink in the halo region with 12% H_2 gas partial pressure. The MAR rate coefficient can be quantified according to the measured MAR sink, and is estimated to be $\sim 4 \times 10^{17} m^3/s$ close to theoretical predictions. The results show that radial transport is the dominant ion loss term in the He/H mixture plasma for all cases except the case with 12% H_2 gas, consistent with previous experiments in H_2 plasmas [17]. Additional evidence for molecular recombination is seen in anomalously large ratios of $\frac{H_\alpha}{H_\gamma}$ at the cold plasma edge. These results show that the MAR takes over from the EIR and expands from the edge of the chamber to the center when the H_2 content is increased.

7.2 Future Study

Although the role of MAR in a detaching plasma is well exhibited, further improvements are required to recognize how MAR behaves in a gas-target divertor region. For example, the detail of the different channels (Eq.(5.3), Eq.(5.4) and Eq.(6.7)) of MAR is still unclear. More investigations are needed to understand the different MAR mechanisms, especially, the H_3^+ channel in PISCES-A. In order to better estimate the ionization source in the core region, measurement of neutral density is also required. Another important parameter to be considered to estimate the MAR rate is the ratio of $\frac{n_{H_2}}{n_e}$. Therefore, further investigations of theoretical simulations of MAR dependent on the $\frac{n_{H_2}}{n_e}$ ratio are needed.

Appendix A:

Abel Inversion

Emission spectroscopy techniques are very common to be used in plasma diagnostics, which are based on the line integrated intensities of plasma emission along a chord. Usually, spatially resolved measurements are necessary to understand the plasma phenomenon.

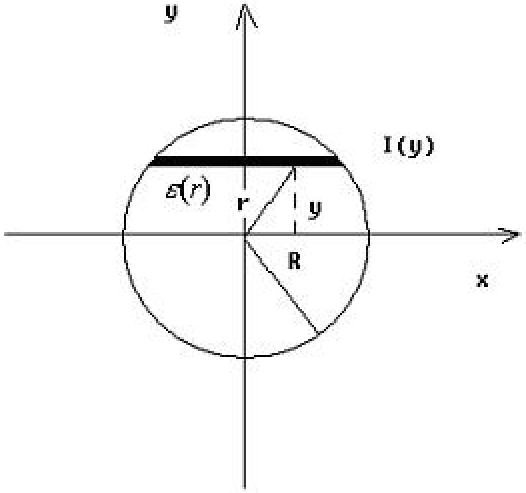

Figure A.1: The schematic of Abel inversion of chord-integrated intensity.

For a cylindrical geometry, Abel inversion is a good method to derive a radial local distribution. The schematic of Abel inversion is shown in Fig. A.1.

$$\begin{aligned} I(y) &= \int_{-x_0}^{x_0} \varepsilon(x)\,dx && \text{(A.1)} \\ I(y) &= 2\int_{y}^{R} \varepsilon(r)\frac{r}{\sqrt{r^2-y^2}}\,dr && \text{(A.2)} \\ \varepsilon(r) &= -\frac{1}{\pi}\int_{r}^{R} \frac{dI(y)}{dy}\frac{dy}{\sqrt{r^2-y^2}} && \text{(A.3)} \end{aligned}$$

According to equation (A.1), the $I(y)$ are the data obtained from spectroscopy, which is the line integral of plasma emissivity $\varepsilon(r)$. A series of discrete data are required to process the Abel inversion. This expression can be rewritten with radius coordinate as equation (A.2), the Abel's integral equation. The reconstruction of $\varepsilon(r)$ from the measured date $I(y)$ can be done analytically by means of the inverse of Abel's integral equation. The equation (A.3) is the final form to derive radial local emissivity with spectroscopy measurements [60].

There are a few methods to implement Abel inversion. All of them can be grouped into two types: fitting methods and numerical methods. Fitting methods, such as the least square method fitting, is possible to obtain an analytical expression of $\varepsilon(r)$. But it is very hard to fit all various distribution profiles. The numerical method can only get the discrete estimation of $\varepsilon(r)$, not an expression. However, the numerical method is very effective if the measured data are discrete and sparse.

Generally, three different methods, Nestor-Olsen method, Spline Interpolation method and Fourier Transform Method, are applied for Abel inversion. The advantages and disadvantages of them are discussed in Ref [60].

The Nestor-Olsen method is very popular to implement Abel inversion with discrete spectroscopic data [45] as below:

$$\varepsilon_k(r) = -\frac{2}{\pi\Delta y}\sum_{n=k}^{N-1} I_n(y)B_{k,n}$$

where $I(y)$ are series of discrete data obtained from experiments, $\varepsilon(r)$ is local radial emissivity profile, k and n are the integer position indices for the radial and lateral intensities, and Δy is the width between two adjacent experimental data. And

$$B_{k,n} = -A_{k,n} for n = k; B_{k,n} = -A_{k,n-1} - A_{k,n} for n \geq k+1$$

where

$$A_{k,n} = \frac{\sqrt{n^2-(n-1)^2} - \sqrt{(n-)^2-(k-1)^2}}{2n-1}$$

With the computational implementation above, the radial distribution of local emissivity are be derived. However, the Nestor-Olsen method is very difficult to get good estimation around the center of the cylindrical geometry, especially, when the number of discrete data points is large, due to the accumulation of noise from the measured data.

In these experiments, 2-D spectroscopic data of emission intensities can be obtained by the PISCES-A spectrometer. As a result, the Abel inversion is implemented by fitting the experimental data with analytical functions. The method employs a piece-wise cubic spline function, least-squares fitted to the data as Eq.(A.4).

$$I(y) = \sum_{k=1}^{N-1} I_k(y) \tag{A.4}$$

where

$$\begin{aligned} I_k(y) &= 0, & y < \xi_k && \text{(A.5)} \\ &= a_k y^3 + b_k y^2 + c_k y + d_k, & \xi_k \leq y \leq \xi_{k+1} && \text{(A.6)} \\ &= 0, & \xi_{k+1} < y && \text{(A.7)} \end{aligned}$$

where ξ_1, ξ_2, ξ_3, ..., ξ_N are the knots of the spline, the measured data points.

This method is very good at noisy data, which is very important since any inversion method tends to amplify the random errors inherent in the measured $I(y)$ data. The emissivity is then calculated by take of derivative of the fitted analytical functions as Eq.(A.3).

Appendix B:

The HeII Spectral line at 468.5nm in a Low Temperature Plasma with a Low Magnetic Field

In this research, the axial flow velocity is estimated by the Doppler shift of HeII emission at 468.5nm. The measured spectroscopic data are fitted by multi-Gaussian components with the least square method and then used to derive the line shift. In order to estimate the axial flow velocity, the light is observed through the mirror which makes an angle of ~ 60 degree with respect to the magnetic field; another view, made orthogonal to the magnetic field, provides an unshifted line emission spectrum as Fig.B.1. The axial flow is then obtained by the shift of the wavelength. In this section, we try to consider the effect of the magnetic field and plasma conditions to the line shift.

Apart from the line of sight contribution, the plasma conditions and magnetic field

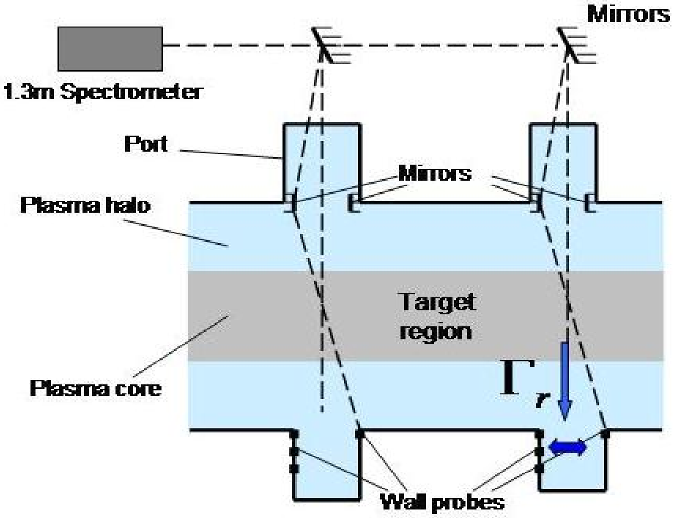

Figure B.1: The schematic drawing of installation of mirrors mounted on the wall of the side port.

affect the line shape of the radiation in a number of ways; and in order to model the line shape, these various effects need to be considered, including Zeeman, Doppler, and Stark effects. Due to the typical densities ($\sim 10^{17} - 10^{18} m^{-3}$) in plasmas in PISCES-A, the Stark broadening in negligible; hence a Gaussian line shape has been used to fit these experimental spectral data. Otherwise, for the plasmas in which Stark broadening shows a significant effect on the shape of spectra, a Lorentzian line shape has to be used to model the line profile. The line emission at 468.5nm that we measured in my experiments consists of 13 fine components in the fine structure multiplet. However, since the resolution of wavelength of the used spectroscopy is $\sim 0.01nm$, it is impossible to distinguish the different lines within the fine structure due to the instrument function. As a result, generally, the fine structure is totally unresolved in my experiments.

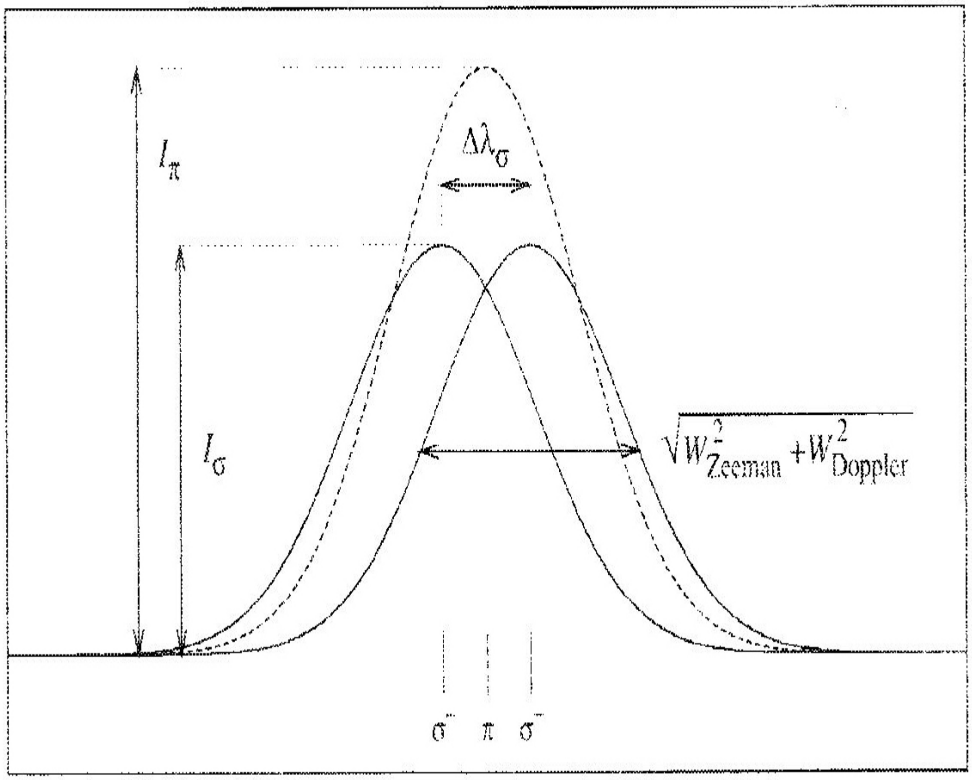

Figure B.2: The different Zeeman components due to the magnetic field polarization and Doppler broadening due to the ion temperature.

Now we consider the line shape of HeII at 468.5nm without the Doppler shift due to axial flow velocity. The magnetic field affect the line shape through the π component and two equal split σ components. When the view chord is perpendicular to the magnetic filed, only a central component π is presented in the line profile; two σ components are also shown when the view is at an angle in respect to the magnetic field as in Fig.B.2. As a result, there are total three components $(\sigma^+, \sigma^-$ *and* $\pi)$ for the view at 60 degree in my experiments. The intensity ratio between the two σ peaks can be calculated by

$$\frac{I_\pi}{I_\sigma} = \frac{2sin^2\theta}{1+cos^2\theta} \tag{B.1}$$

where I_π and I_σ are the magnitudes of the π and σ components, and θ is the angle between the path of the light and the magnetic field.

The ion temperature makes an effect to the line shape through the Doppler broadening as in Fig.B.2. The widths of π and $\sigma^\pm$ are weakly dependent on the magnetic filed and the polarization. They are assumed to have equal widths which is independent of the magnetic field. Consequently, the fact that the W_{Zeeman} is independent of the magnetic field suggests that the width is caused mainly due to the fine structure, which is then written in

$$W_{Zeeman} = \sqrt{W^2_{fitted} - W^2_{Doppler}}$$

where W_{fitted} the simulated result of the broadening of the line shape; $W_{Doppler}$ is the broadening due to the ion temperature; and W_{Zeeman} is the broadening due to the Gaussian fit of the fine structure. We may describe this effect as the Zeeman broadening, but it should be noted that it is independent of any magnetic field, due to the unsolved fine-structure.

Therefore, we can say the effect of the fine structure enters the simulation of the line shape through the W_{Zeeman}; the magnetic field affects the line shape through the Zeeman split of the two σ peaks; and the ion temperature makes an effect through the Doppler broadening. The effects dependent on the magnetic field and the temperature can be describe by only three numerical parameters. The simulations have already been done in Ref.[3]. The main points described below are from the published paper, Ref.[3]. The parametrization is implemented by considering the three components (including π and Zeeman splitting $\sigma^{\pm}$) due to the magnetic field and Doppler broadening due to ion temperatures. The different polarization components σ^{-}, σ^{+} and π are grouped together. The split $\Delta\lambda_{\sigma} = \sigma^{+} - \sigma^{-}$ and intensity ratio $\frac{I_{\pi}}{I_{\sigma}}$ can be calculated by fitting the line shapes and then getting the fitted positions and peak intensities.

The corresponding parameters to simulate the line shape can be described by the following two equations:

$$\Delta\lambda_{\sigma} = \alpha B \tag{B.2}$$

where $\Delta\lambda_{\sigma}$ is the split of two σ peaks due to the magnetic field; B is the magnetic field.

$$\frac{W_{Zeeman}}{W_{Doppler}} = \beta(k_B T)^{\gamma} \tag{B.3}$$

where T is the ion temperature.

The parametrization of Zeeman effect and Doppler effect for hydrogen-like spectra has been simulated in Ref.[3]. The fit curve and the parameters are obtained by nonlinear least square fits to the corresponding experimental line shapes and widths. And all the parameters are independent of the magnetic field and ion temperature. The corresponding parameters for HeII at 468.5nm are calculated to be:

$$\alpha = 0.0205205 nm/Tesla$$

$$\beta = 1.6118$$

$$\gamma = -0.4838$$

Moreover, this range of validity of this parametrization can be extended even into regions with very low temperatures and strong magnetic fields.

The Zeeman splitting can be approximated by a simple relation dependent only upon the strength of the magnetic field as Eq.(B.2). In my experiments, the magnetic field $B = 0.096 Tesla$, as a result, the splitting is 0.002nm. Although the split is comparable to the Doppler shift in my experiments, the split will have no effect on it since the π peak is exactly in the middle between the σ peaks. Similar results are obtained in Ref.[11] and Ref.[3]. Only one exception is when the fine-structure starts to become resolved, which means the temperature is very low and the magnetic field is large. It is also suggested by Eq.(B.2) and (B.3). The fine structure and the Zeeman split will change the line shape. As the temperature decreases, the Gaussian shape narrows and then more concentrates on the dominating components, which makes the wavelength shift a little during the fitting of the line shape as a whole.

Since the FWHM of the Doppler broadening for 1eV helium ion temperature in this wavelength is 0.018nm, the Doppler broadening is $\sim 0.04nm$ due to the ion temperature $T_i \sim 5eV$ ($\Delta\lambda_{FWHM} \sim T^{\frac{1}{2}}$) in the core region in my experiments. As a result, the condition of the exception is not shown and the line shift does not exist. For the plasma in the cold halo region, the ion temperature $T_i \sim 0.1eV$ and then the Doppler broadening is $\sim 0.006nm$. According to Eq.(B.2), the split of the σ peaks in the halo region is around 0.02nm. However, another important factor, the instrumental function, make the fine structure impossible. That is because we fit the emission spectra with an instrumental function convolved with a Gaussian for each of the Zeeman triplet components. The resolution of the PISCES-A is $\sim 0.01nm$. As a result, the low temperature is impossible to make the fine structure resolved. Therefore, with the low magnetic field $\sim 0.01Tesla$ in my experiments, the line shift is negligible. The simulation results in Ref. [3] show the magnetic field needs to be considered when it is a few Tesla, much larger than that in my experiments.

Overall, the Doppler shift measurement is affected when the magnetic field is large (a few Teslas), the ion temperature is low and the spectrometer has better resolution. For the plasma in PISCES-A, the effect due to the magnetic and ion temperatures is totally negligible.

Appendix C:

Error Analysis of Measurements

C.1 Error Analysis of Langmuir Probe Measurements

In my experiments, the electron density and temperature were measured by the scanning Langmuir probe. They were obtained by fitting the measured data with the corresponding I-V characteristic as Eq. (C.1) [20].

$$I = 10^{18} n_e e A_p T_e^{1/2} m_i^{-1/2} \left[\frac{1}{2} \left(\frac{2m_i}{\pi m_e} \right)^{1/2} \exp \frac{e(V - V_p)}{T_e} - \frac{A_s}{A_p} \exp\left(-\frac{1}{2}\right) \right] \tag{C.1}$$

where I and V are the probe current and sweeping voltage; A_p is the area of the probe tip; A_s is the area of the sheath surface around the probe tip; the n_e, T_e and V_p are the electron density, electron temperature and plasma potential, respectively; m_i and m_e are the masses of the ion and electron.

The deviation of the data from the model (Eq.(C.1)) can be used to find the errors of electron density and electron temperature.

The deviation of the measured current from the model current is given as

$$\sigma = \sqrt{\frac{\sum_{i=1}^{N}(I_i - I_i^*)^2}{N_{total} - N_{parameter}}} \tag{C.2}$$

where σ is the error of fitting the measured data with the model Eq.(C.1).

The relative error in the inferred density and electron temperature due to random or stochastic deviation in the measured data, $I_i(V)$, are given as

$$\varepsilon_{n_e} = \sqrt{\frac{\sum_{i=1}^{N}(I_i - I_i^*)^2}{\sum_{i=1}^{N}\left(\frac{\partial I_i^*}{\partial n_e} \cdot n_e^{fit}\right)^2}} \tag{C.3}$$

and

$$\varepsilon_{T_e} = \sqrt{\frac{\sum_{i=1}^{N}(I_i - I_i^*)^2}{\sum_{i=1}^{N}\left(\frac{\partial I_i^*}{\partial T_e} \cdot T_e^{fit}\right)^2}} \tag{C.4}$$

where I_i is the measured raw data point; I_i^* is the value of this model at the same probe voltage, which is considered as the real value of the current; N_{total} is the number of data points; $N_{parameter}$ is the number of parameters to be fitted; and n_e^{fit} and T_e^{fit} are the fitted density and electron temperature.

The errors of n_e and T_e are in the range of $10 \sim 20\%$. By averaging the results obtained from a series ($20 \sim 25$) of repeated measurements, the error can be reduced to $\sim 3-4\%$. The systematic error of probe measurements for electron density and electron temperature always exists. A systematic error in the range of 10%-20% does not invalidate the conclusion in this thesis. It is verified by the particle balance for the 0% H_2 case later.

In this appendix, we use the 5.9% H_2 case as an example to show the error analysis of the measurements and particle balance analysis.

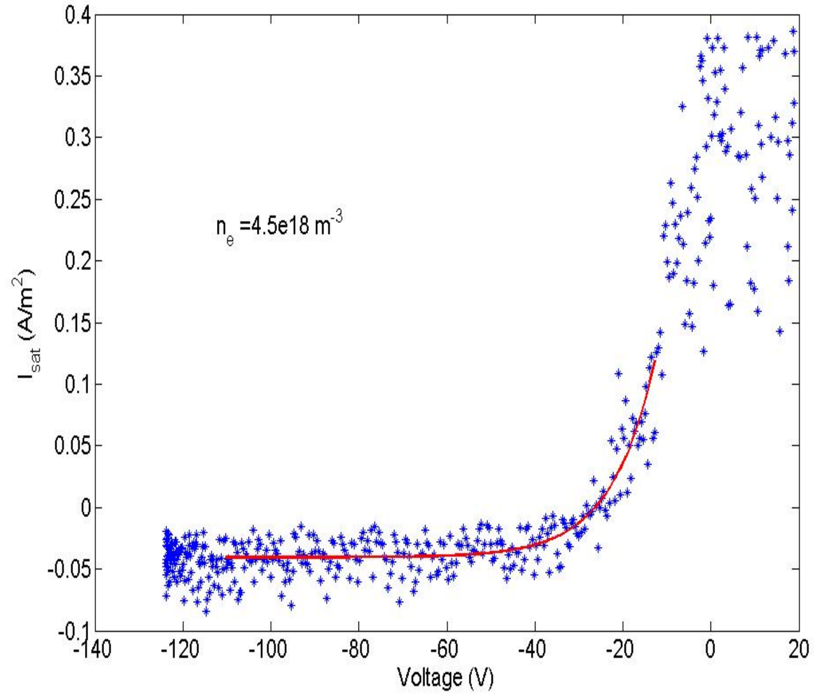

Figure C.1: Fitting the Langmuir probe data with Eq.(C.1)for the 5.9% H_2 case.

Fig.C.1 shows the fitting of the Langmuir probe data for the 5.9% H_2 case. The estimated electron density is $n_e = 4.5 \times 10^{18} m^{-3}$. The deviation of this model by Eq.(C.2) is 0.003. The the error of the electron density is then calculated to be 7% by Eq.(C.3). By averaging the results obtained from 20 repeated measuements, the error of the electron density is divided by $\sqrt{20}$.

C.2 Error Analysis of Axial Flow Velocities

The axial flow velocity was estimated by the Doppler shift of the HeII emission. In order to get a better resolution of the line shift, the measurement of the Doppler shift was operated in second order of He^+ emission $\lambda = 4685\text{Å}$ employing a 1200 lines/mm grating. The fine structure includes 13 lines given in Table 4.1. The Doppler shift can be estimated by fitting the Eq.(C.5) [24].

$$I(\lambda) = I_0 \sum_{l=1}^{13} g_l A_l exp\left\{ -\left(\frac{\lambda - \lambda_0 - \lambda_l}{\lambda_{1/e}} \right)^2 \right\} \tag{C.5}$$

where λ_l, A_l and g_l are the wavelength, Einstein coefficient and the statistical weight of the upper level. Line label l is from 1 to 13. The fitting parameters are the Doppler shift λ_0, the amplitude I_0 and the Gaussian line broadening $\lambda_{1/e}$.

The spectroscopic raw data are fitted with multi-Gaussian components as Eq.(C.6). The difference of b_i obtained by fitting the raw data of two views is the Doppler shift in pixel subject to the angle between the views.

$$I = \sum_{i=1}^{k} a_i \exp\left[-\left(\frac{x - b_i}{c_i} \right)^2 \right] \tag{C.6}$$

where I is the relative intensity of the emission; x is the pixel; a_i, b_i and c_i are the fitting parameters; i is the order of the Gaussian fitting; and k is the number of Gaussians used.

The relative error of the Doppler shift measurement is given in

$$\varepsilon_{\Delta\lambda} = \sqrt{\frac{\sum_{j=1}^{N}(I_j - I_j^*)^2}{\sum_{j=1}^{N}\left(\sum_{i=1}^{k} a_i \exp\left[-\left(\frac{x-b_i}{c_i}\right)^2\right]\cdot\frac{2(x-b_i)}{c_i^2}\right)^2}} \tag{C.7}$$

where I_j is the measured relative intensity; I_j^* is the value of this model at this point, which is considered as the real value; x is the pixel; a_i, b_i and c_i are the fitting parameters; i is the order of the Gaussian fitting; and j is the index of data points.

The error of the Doppler shift depends on how good we fit the spectroscopic data to the multi-Gaussian model. Overall, the error of the axial flow velocity is $\sim 5\%$.

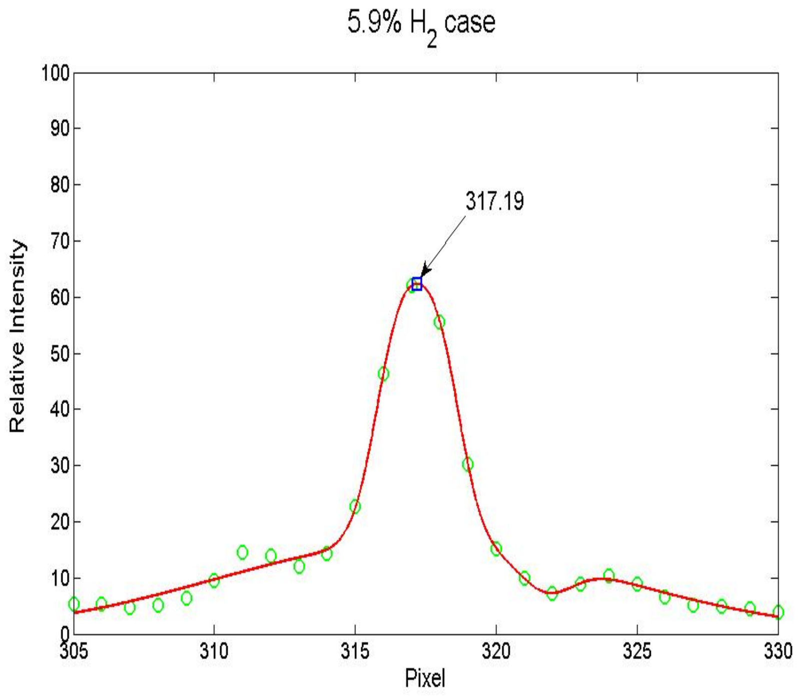

Figure C.2: Fitting the spectroscopic data with Eq.(C.6)for the 5.9% H_2 case.

Fig.C.2 shows the fitting of the spectroscopic data for the 5.9% H_2 case with

Eq.(C.6). The estimated pixel with maximum relative intensity is 317.19. The deviation of this model by a similar equation to Eq.(C.2) is 1.7. The the error of the axial flow velocity is then calculated to be 5% by Eq.(C.7). The flow velocity here is 1.57km/sec.

C.3 Error Analysis of Wall Probe Measurements

For the set of three wall probes, they are respectively 6.5mm, 21.5mm and 36.5mm deep into the side port from the chamber wall as in Fig.2.3 and Fig.2.2. The radial flux to the chamber wall is estimated by fitting the exponential equation (Eq.C.8) and then using Eq.(C.9).

$$I(y) = I_0 exp(-\frac{y}{\lambda_r}) \tag{C.8}$$

where $y = r - r_{wall}$ is the distance into the side port from the chamber wall, that is, $y = 0$ on the chamber wall locates at radius r_{wall}; and λ_r is the decay length.

$$\Gamma_r = \frac{2\lambda_r I_0}{W_p A_w} \tag{C.9}$$

where W_p is the width of the port and A_w is the area of the wall probe. Here Γ_r denotes the cross-field transport at the axial position $z = Z_p - \frac{W_p}{4}$, where z_p is the axial position of the centerline of the side port.

The error of the radial flux to the chamber wall also depends on the fitting of the exponential Equation C.8. Although the data from the third wall probe are not accurate since they are at the noise level, it has no effect to the total estimated radial flux at all since the ion saturation current decays rapidly with the depth into the side port. The error of the radial flux to the chamber wall is $\sim 3\%$.

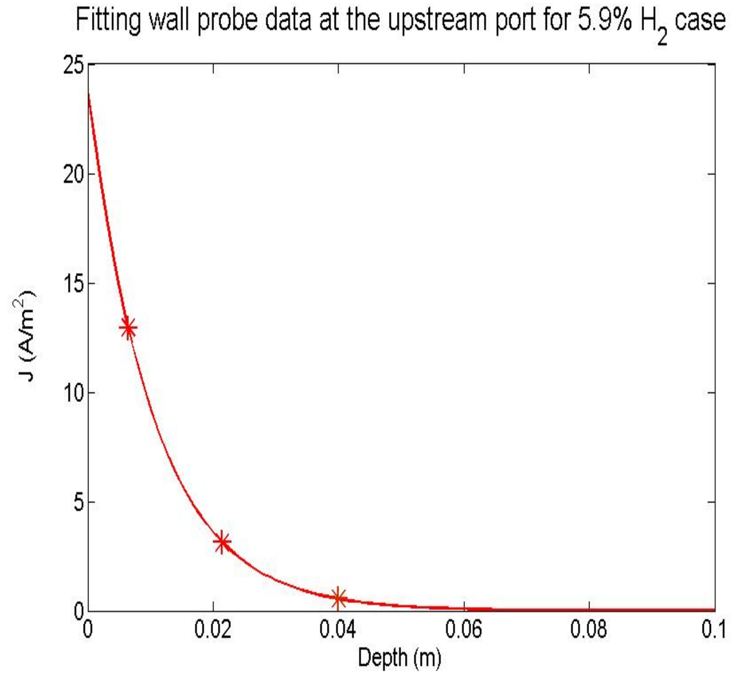

Figure C.3: Fitting the wall probe data at the upstream port with Eq.(C.8)for the 5.9% H_2 case.

Fig.C.3 shows the fitting of the wall probe data at the upstream port for the 5.9% H_2 case with Eq.(C.8). The deviation of this model by a similar equation to Eq.(C.2) is 0.05. The the error of the radial flux to the chamber wall is then calculated to be 4% due to the uncertainty of the data from third probe. The total radial flux for this case is 0.3A.

C.4 Error Analysis of Ionization and Recombination Estimations

The electron temperature in the cold halo is estimated by the calibrated high n emissions of HeI. The electron density in the halo is then obtained by the measured ion saturation current and the estimated electron temperature. Although the error the electron temperature in the cold halo changes from 10% for EIR dominate plasma to 70% for EIR quenched plasma, it does not have much effect to the estimation of S/XB of recombination since the S/XB of recombination is weakly dependent on the electron temperature and electron density.

Applying Abel inversion to the absolute chord-averaged intensity profiles, the radial profiles of the emissivity can be obtained. The error bars of emissivity in the core region are very big because of the accumulation effect during Abel inversion. In the core region, due to the relatively high electron temperature $(\sim 10eV)$, the EIR is negligible. In the halo region where EIR is dominant, the error of estimation of the EIR sink is $\sim 5\%$ due to the Able inversion. The details about Abel inversion are presented in Appendix B.

Similarly, the ionization source in the core region is also estimated by a chord-averaged HeI emission. Due to the characteristic of Abel inversion, the error of emissivity for ionization in the core region is a litter larger, around 10%. Therefore, the spectroscope measurements give a 5% error of S_{EIR} and a 10% error of S_{Ion}.

For the 5.9% H_2 case, the ionization source is 0.09A and the error is 10%; the total recombination is 0.024A and the error is 5%.

C.5 Error Analysis of Other Parameters

C.5.1 He^{2+} Ions

Doubly ionized helium He^{2+} is neglected in this analysis; this is justified by the measured intensity ratio HeI(6678)/HeII(4685)$\sim 0.8 \times 10^3 - 1.5 \times 10^3$. Together with the expected photon efficiencies $S/XB(6678) \sim 50 - 80$ and $S/XB(4685) \sim 5 - 8$ for the core plasma conditions of these experiments [66] and assuming comparable He^+ and He^{2+} loss rates, we arrive at a negligible He^{2+} fraction $\frac{n_{He^{2+}}}{n_{He^+}} < 2 \times 10^{-4}$.

C.5.2 Axial Flow Flux in the Halo Region

The axial flow in the halo region is neglected during the particle balance analysis. The axial flow speed drops by two orders of magnitude small for $r > 3.5cm$ while the electron density in the halo decreases to $< 10\%$ of the density in the core region. As a result, the axial flow in the halo region is three orders of magnitude smaller than that in the core region and can be neglected in the halo region particle balance.

C.5.3 Molecular-Assisted Dissociation (MAD)

This analysis neglects molecular-assisted dissociation (MAD), which includes two channels: $HeH^+ + e \rightarrow He + H^+ + e$ and $HeH^+ + e \rightarrow H + He^+ + e$. The rate coefficients of MAD in a He/H plasma are not available. Using the measured results and the rate coefficient of MAD obtained from a pure hydrogen plasma [8], the total estimated MAD in the core region is $\sim 0.006A - 0.08A$ with H_2 injection. The effect of MAD modifies the value to MAR, but the basic conclusions drawn in this thesis are still valid. In Fig.6.2, the particle balance was done without MAD since the rate coefficients of MAD can not be obtained from published papers.

C.6 Error Analysis of the MAR

According to the errors of measurements we obtained above, the error of MAR can be estimated by adding them up together. It changes in the range of $\sim 0.06A - 0.09A$ with H_2 gas partial pressure from 0% to 12%. Correspondingly, the error of the MAR rate coefficient is derived from the error of the obtained MAR sink by Eq.(6.6). The error analysis shows that the conclusions we claimed in Chapter 6 and 7 are valid.

The error analysis for the 5.9% H_2 case:

Table C.1: Error Analysis for the 5.9% Case

Measurements	Estimated Valvue	Deviation from Model	Relative Error	Absolute Error
electron density	$4.5 \times 10^{18} m^{-3}$	0.003	7%(single)	error of $\Gamma_{\|}$: 0.056A
flow velocity	1.57km/sec	1.7	5%	
radial flux to the wall	0.3A	0.05	4%	0.012A
ionization source	0.09A	N/A	10%	0.009A
EIR sink	0.024A	N/A	5%	0.001A
MAR sink	0.20A	N/A	39%	0.078A

Bibliography

[1] G. Y. Antar, S. I. Krasheninnikov, Phys. Rev. Lett., 87, 065001, (2001)

[2] Atomic Line List, http://www.pa.uky.edu/∼peter/atomic/

[3] A. Blom and C. Jupen, Plasma Phys. Control. Fusion, 44, 1229-1241, (2002)

[4] Lisa M. Blush Ph.D. Thesis, University of California, San Diego, 2001

[5] P. K. Browning, Journal of Nuclear Materials, 337-339, 232-236, (2005)

[6] M. J. de Graaf et al., Phys. Rev. E, 48, 2098, (1993)

[7] N. Ezumi, D. Nishijima, J. Nucl. Mater., Vol. 266-269, 337-342, (1999)

[8] U. Fantz, D. Reiter, B. Heger, D. Coster, Journal of Nuclear Materials, 290-293, 367-373, (2001)

[9] T. Fujimoto, J. Quant. Spectrosc. Radiat. Transf. Vol. 21, 439-455, (1979)

[10] T. Fujimoto, Plasma Spectroscopy, Oxford University Press, (2004)

[11] J. Ghosh, H. R. Griem, and R. C. Elton et. al., Physics of Plasmas, Vol. 11, Num. 3, 1033-1042, (2007)

[12] M. Goto, K. Sawada, T. Fujimoto, Physics of Plasmas, Vol. 9, Num. 10, 4316-4324, (2002)

[13] H. R. Griem, Plasma Spectroscopy (McGraw-Hill, New York, 1964)

[14] O. Gruber, A, Kallenbach, et al., Phys. Rev. Lett., 74, 4217 (1995)

[15] E. M. Hollmann, A. Yu. Pigarov 28th EPS Conference on Contr. Fusion and Plasma Phys., Funchal, 2001 ECA Vol. 25A (2001) 285-288

[16] E. M. Hollmann, D. G. Whyte Phys. Plasmas Vol.8, Number 7, (2001) 3314-3320

[17] E. M. Hollmann, A. Yu. Pigarov, R. Seraydarian, D. G. Whyte, S. I. Krasheninnikov, Phys. Plasmas Vol.9, Number 4, (2002) 1226-1232

[18] E. M. Hollmann, A. Yu. Pigrov, Phys. Plasmas. Vol. 9, Number 10, 4330-4339, (2002)

[19] M. Hudis and L. M. Lidsky, J. Appl. Phys. 41, 5011 (1970)

[20] I. H. Hutchinson, Principles of Plasma Diagnostics, Cambridge University Press, 1st Edition, 1987

[21] I. H. Hutchinson, Principles of Plasma Diagnostics, Cambridge University Press, 2nd Edition, 2002

[22] R. C. Isler, G. R. Mckee, Phys. Plasmas, 4, 2989, (1997)

[23] R. K. Janev, D. Reiter, and U. Samm, Collision Processes in Low-Temperature Hydrogen Plasmas, Forschungszentrum Juelich, Juel-4105, 2003

[24] S. Kado, J. Plasma Fusion Res., Vol.79, No.9, 841-843, (2003)

[25] S. Kado, Contrib. Plasma Physics 44, No 7-8, 656-661 (2004)

[26] H. Kawazome, K. Kondo, K. Ida, K. Takiyama, M. Goto, S. Morita, N. Tamura, N. Ohyabu, S. Sudo, J. Nucl. Mater., 313-316, 716-719, (2003)

[27] S. I. Krasheninnikov, A. Yu. Pigarov, D. J. Sigmar, Physics Letters A 214, 285-291, (1996)

[28] S. I. Krasheninnikov, A. Yu. Pigarov, J. Nucl. Mater., 241-243, 283, (1997)

[29] S. I. Krasheninnikov, Phys. Lett. A. 283, 368, (2001)

[30] H. Kubo, S. Higashijima, et al., Proceedings of the 1998 ICPP 25th EPS Conference on Plasma Physics and Controlled Fusion, p427, (1998)

[31] S. Kubo, et al., 1998 Proc. 25th EPS Conf. on Controlled Fusion and Plasma Physics (Prague) Vol. I, p56

[32] J. P. Lanquart, J. Phys. D: Appl. Phys. 19 (1986) 925-931

[33] J. D. Lawson, Proceedings of the Physical Society B, Vol. 70, p. 6, (1957)

[34] B. Lipschultz, J. Goetz, B. LaBombard, G. M. McCracken, J. L. Terry, M. Graf, R. S. Granetz, D. Jablonski, C. Kurz, A. Niemczewski, J. Snipes, J. Nucl. Mater., 50, 220-222, (1995)

[35] B. Lipschultz, J. L. Terry, C. Boswell, J. A. Goetz, A. E. Hubbard, S. I. Krasheninnikov, B. LaBombard, D. A. Pappas, C. S. Pitcher, F. Wising,a) and S. Wukitch, Phys. Plasmas, 6(5), 1907-1916, (1999)

[36] B. Lipschultz, J. L. Terry, C. Boswell, et al., J. Nucl. Mater., 266-269, 370, (1999)

[37] W. Lochte-Holtgreven, Plasma Diagnostics, North-Holland Publishing Company, 1968

[38] Wolfgang Lotz, Zeitschrift fur Physik, 216, 241-247, (1968)

[39] D. Lumma, J. L. Terry, B. Lipschultz, Phys. Plasmas, 4, 2555, (1997)

[40] C. F. Maggi, L. D. Horton, J. Nucl. Mater., 266-269, 867, (1999)

[41] G. M. McCRACKEN, M.F. Stamp, R.D. Monk, A.G. Meigs, J. Lingertat, R. Prentice, A. Starling, R.J. Smith and A. Tabasso, Nuclear Fusion, Vol. 38, No. 4, 619-629, (1998)

[42] G. M. McCracken, R. D. Monk, A. Meigs, L. Horton, L. C. Ingesson, J. Lingertat, G. F. Matthews, M. G. O'Mullane, R. Prentice, M. F. Stamp, P. C. Stangeby, J. Nucl. Mater., 266-269, 37 (1999)

[43] K. Miyamoto, Contrib. Plasma Phys., 46, No. 7-9, 643-648 (2006)

[44] K. Miyamoto, Journal of the Physical Society of Japan, Vol. 76, No. 3, 034501 (2007)

[45] O. H. Nestor and H. N. Olsen, SIAM Rev. 2, 200, (1960)

[46] D. Nishijima, N. Ezumi, Contrib. Plasma Phys., Vol. 38, (1998) 55

[47] D. Nishijima, N. Ezumi, H. Kojima, N. Ohno, S. Takamur, S. I. Krasheninnikov, A. Yu. Pigarov, J. Nucl. Mater., Vol. 266-269. (1999) 1161

[48] D. Nishijima, A. Yu. Pigarov Modeling of helium plasma transport in linear divertor simulator NAGDIS-II with UEDGE

[49] D. Nishijima, R. P. Doerner, M. J. Baldwin, E. M. Hollmann, R. P. Seraydarian, Y. Udda, Physics of Plasmas, 14, 103509, (2007)

[50] N. Ohno, N. Ezumi, S. Takamura, S. I. Krasheninnikov, A. Yu. Pigarov, Phys. Rew. Lett., Vol. 41, No. 8, 818, (1998)

[51] N. Ohno, D. Nishijima, S. Takamura, Y. Uesugi, M. Motoyama, N. Hattori, H. Arakawa, N. Ezumi, S. Krasheninnikov, A. Pigarov, U. Wenzel, Nuclear Fusion, Vol. 41, No. 8, 1055-1065, (2001)

[52] N. Ohno, Contrib. Plasma Phys., 44, 222, (2004)

[53] N. Ohno, M. Tanaka, Phys. Plasmas, 6(6), 2486-2494, (1999)

[54] J. Park, Ph.D. thesis, Princeton University, 1998

[55] T. W. Petrie, D. Buchenauer, D.N. Hill, C. Klepper, S. Allen, R. Campbell, A. Futch, R.J. Groebner, A. Leonard, S. Lippmann, M. Ali Mahdavi, M. Rensink, P. West, J. Nucl. Mater. 196-198, 848 (1992)

[56] A. Yu. Pigarov, S. I. Krasheninnikov, Phys. Lett. A , 222, 251-257, (1996)

[57] A. Yu. Pigarov, Physica Scripta., T96, 16-31, (2002)

[58] A. Yu. Pigarov, S. I. Krasheninnikov J. Nucl. Mater. 313-316, 1076, (2003)

[59] D. L. Rudakov, Rev. of Sci. Intr. Vol. 70, Number 1, 476 (1999)

[60] A. Sainz, A. Diaz, Applied Spectroscopy, Vol.60, Number 3, 229 (2006)

[61] L. Schmitz, J. Nul. Mater. 337-339, 1096-1100, (2005)

[62] L. Schmitz, B. Merriman, L. Blush, R. Lehmer, R. W. Conn, R. Doerner, A. Grossman, and F. Najmabadi, Phys. Plasmas 2, 3081, (1995)

[63] J. Semaniak, Physical Review A, Vol. 54, No. 6, R4617-R4620, (1996)

[64] P. C. Stangeby, The Plasma Boundary of Magnetic Fusion Devices, IOP Publishing, p505, (2000)

[65] P. C. Stangeby, The Plasma Boundary of Magnetic Fusion Devices, IOP Publishing, p497, (2000)

[66] H.P. Summers, Atomic Data and Analysis Structure: User's Manual, JET Joint Undertaking Report JET-IR94, (1994)

[67] S. Takamura, N. Ohno, D. Nishijima, Y. Uesugi, Plasma Source Sci. Technol., 11, A42-A48, (2002)

[68] S. Takamura, N. Ohno Static and Dynamic Behaviors of Plasma Detachment in Divertor Simulator NAGDIS-II

[69] Tenney F H and Lewin G (1974) Princeton Plasma Physics Laboratory Report MATT 1050 P75

[70] J. L. Terry, B. Lipschultz, A. Yu. Pigarov, C. Boswell, S. I. Krasheninnikov, B. LaBombard, D. A. Pappas, CP443, Atomic Processes in Plasmas: Eleventh APS Topical Conference (1998) 43

[71] J. L. Terry, B. Lipschultz, A. Yu. Pigarov, S. I. Krasheninnikov, B. LaBombard, D. Lumma, H. Ohkawa, D. Pappas, M. Umansky, Phys. Plasmas, Vol. 5, No. 5, 1759, (1998)

[72] A. Tonegawa, 28th EPS Conference on Contr. Fusion and Plasma Phys., ECA, Vol. 25A, 2145-2148, (2001)

[73] U. Wenzel, K. Behringer, J. Nucl. Mater., 266-269, 1252, (1999)

[74] U. Wenzel, K. Behringer, A. Carlson et al 1998 Proc. 25th EPS Conf. on Controlled Fusion and Plasma Physics (Praha) ECA vol. 20C 504

[75] Ya. B. Zel'dovich and Yu. P. Raizer. Edited by Wallace D. Hayes and Ronald F. Probstein, Physics of Shock Waves and High-Temperature Hydrodynamic Phenomena (Academic Press, New York, 1966), Vol.1, P406-408